Size-dependent ultrafast ionization dynamics of nanoscale samples in intense femtosecond x-ray free-electron laser pulses

vorgelegt von

Diplom-Physiker
Sebastian Schorb

aus Karlsruhe

Von der Fakultät II - Mathematik und Naturwissenschaften
der Technischen Universität Berlin
zur Erlangung des akademischen Grades

Doktor der Naturwissenschaften
- Dr. rer. nat. -

genehmigte Dissertation

Promotionsausschuss:

Vorsitzender:	Prof. Dr. Mario Dähne
Gutachter:	Prof. Dr. Thomas Möller
Gutachter:	Prof. Dr. Ulf Saalmann

Tag der wissenschaftlichen Aussprache: 30. Oktober 2012

Berlin 2012

D 83

Abstract

All matter exposed to intense femtosecond x-ray pulses from the Linac Coherent Light Source (LCLS) free-electron laser is strongly ionized on femtosecond time scales. On these time scales, the ionization is competing with the lifetimes of the created inner-shell vacancies. In the present work, it is shown that for nanoscale objects the environment, i.e., nanoparticle size, is an important parameter for the time-dependent ionization dynamics in intense x-ray pulses because it has an influence on the inner-shell vacancy liftimes. As a sample system, argon atoms and clusters with sizes between $\langle N \rangle = 55$ and $\langle N \rangle = 1600$ were chosen. The clusters were irradiated with 480 eV x-ray pulses reaching power-densities of up to a few $10^{17}\,\mathrm{W/cm^2}$. At this photon energy dominantly the argon L-shell is ionized and the remaining vacancies are most likely filled via Auger decay. To investigate the electron dynamics, the x-ray pulse length was tuned between 30 fs and 85 fs, using the novel LCLS slotted spoiler technique. The ionization products were measured with an ion time-of-flight spectrometer with a special slit aperture. This aperture efficiently suppresses atomic background, which yields cluster spectra of unprecedented quality. Spectra for different pulse lengths and a range of pulse energies were collected for atoms and all cluster sizes. In atoms, as in clusters, longer x-ray pulses are absorbed more efficiently than shorter x-ray pulses with the same number of photons. To shed light on size-dependent effects in clusters, an independent measure for the time-dependent component of the absorption for every cluster size was found by means of x-ray induced transparency increase (XITI). The XITI increases from atoms to clusters and shows a clear cluster size dependence. A rate equation model for the ionization of atomic systems has been developed to support the interpretation of the experimentally determined XITI as a function of the cluster size. As a result, the Auger lifetimes of large argon clusters are found to be longer than for small clusters and isolated atoms. This is due to delocalization of the valence electrons in the x-ray induced nanoplasma, resulting in a smaller overlap between valence electrons and core holes. As a consequence, large nanometer sized samples absorb intense femtosecond x-ray pulses less efficiently than small ones.

Kurzfassung

Jegliche Materie, die den intensiven Femtosekunden-Röntgenpulsen des Linac Coherent Light Source (LCLS) Freie-Elektronen Lasers ausgesetzt ist, wird sehr stark ionisiert. Auf den Femtosekundenzeitskalen der Pulse, konkurriert die Ionisierungsrate mit den Lebensdauern der Innerschalenlöcher. In dieser Arbeit wird gezeigt, dass für Teilchen auf der Nanometerskala der Einfluss der Umgebung, d.h. die Teilchengröße, ein wichtiger Parameter für die zeitabhängige Ionisierung in intensiven Röntgenpulsen ist, weil sie Auswirkungen auf die Lebensdauern von Innerschalenlöchern hat. Als Probensystem wurden Argon-Atome und Argon-Cluster mit einer Größe zwischen $\langle \mathrm{N} \rangle = 55$ und $\langle \mathrm{N} \rangle = 1600$ gewählt. Die Photonenenergie wurde mit 480 eV so eingestellt, dass vorranig die Argon-L-Schale ionisiert wird, wobei die entstandenen Innerschalenlöcher hauptsäechlich durch Auger-Zerfall wieder aufgefüllt werden. Um die Ionisationsdynamik zu untersuchen, wurde die Länge der Röntgenpulse zwischen 30 fs und 85 fs mit Hilfe der neuartigen LCLS *slotted spoiler*-Technik eingestellt. Im Experiment wurden Leistungsdichten von einigen $10^{17}\,\mathrm{W/cm^2}$ erreicht. Die Ionisationsprodukte wurden mit Hilfe eines Flugzeitmassenspektrometers mit einer speziellen Schlitzblende gemessen. Diese Schlitzblende unterdrückt den atomaren Hintergrund und ermöglicht es Clusterspektren von hoher Qualität aufzunehmen. Es wurden Argon-Atome und Cluster bei verschiedenen Pulslängen und Pulsenergien untersucht. Die Daten zeigen, dass in Atomen und Clustern lange Röntgenpulse auf der Femtosekundenzeitskala effizienter absorbiert werden als kurze Pulse mit der gleichen Anzahl von Photonen. Für die Untersuchung größenabhängiger Effekte wurde für jede Clustergröße ein Maß für die zeitabhängige Absorption gefunden, dass von sekundären Effekten unabhängig ist, die sogenannte röntgeninduzierte Transparenzzunahme (engl. x-ray induced transparency increase - XITI). Es zeigt sich, dass die XITI von Atomen zu Clustern zunimmt und ein charakteristisches größenabhängiges Verhalten hat. Ein Ratengleichungsmodel für die Ionisierung von atomaren Systemen wurde entwickelt, um die Interpretation der experimentell bestimmten XITI in Abhängigkeit der Clustergröße zu unterstützen. So konnte gezeigt werden, dass die Auger-Lebensdauern in großen Clustern länger sind als in kleinen Clustern und isolierten Atomen. Dies wird durch die Delokalisierung der Valenzelektronen im röntgeninduzierten Nanoplasma verursacht, durch die der Überlapp zwischen Valenzelektronen und Innerschalenlöchern veringert ist. Dadurch absorbieren größere Partikel auf der Nanoskala intensive Femtosekunden-Röntgenpulse weniger effizient als kleinere Partikel.

Contents

Chapter 1

Introduction

Intense x-ray flashes from free-electron laser sources such as the Linac Coherent Light Source (LCLS) [1] open the door for a wide range of novel applications. Femtosecond infra-red laser systems can reach ultrahigh intensities on sub femtosecond time scales and synchrotron sources produce light at very short wavelengths. Free-electron lasers, however, are the first light sources that can produce pulses that access both, short timescales and short wavelengths. X-ray pulses with a length down to few femtoseconds and intensities up to $10^{18} W/cm^2$ have become available. For the first time a wide range of atomic core-levels can be reached with ultrashort and ultraintense x-ray pulses. This allows for imaging ion motion [2] and probing bond-breaking and changes in chemical shifts [3] on a femtosecond time scale. With the intensity of the pulses of the LCLS small objects [4] and proteins in nanocrystals [5, 6] can be imaged with single shots and even single-shot imaging of non-periodic nanometer-sized objects is within reach. At the same time new states of matter can be prepared and probed ranging from double and multiple core-holes in atoms [7] and molecules [8, 9] to hot plasmas in clusters [10] and solid samples [11]. The absorption steps leading to these states and the processes following the absorption are barely investigated. Understanding these phenomena is of great interest for time-resolved imaging of molecules, imaging of non-periodic objects and understanding the dynamics in hot dense plasmas.

Specifically, future single-shot imaging experiments will be limited by the x-ray pulse length. Fig. 1.1 shows a schematic of a typical single shot imaging setup for non-periodic objects. The pulse length needs to be shorter than the timescale on which the sample experiences significant damage. Two types of damage can be distinguished, electronic and structural damage. Electronic damage refers to the removal or excitement of bound electrons that subsequently do not scatter or do not contain information about the structure of the sample anymore. Structural damage occurs as a result of the electronic damage. When the sample is ionized and turned into a nanoplasma through photoabsorption, it will explode. The structural damage in large molecules is predicted to happen on a few ten femtosecond timescale. For nanocrystals signifi-

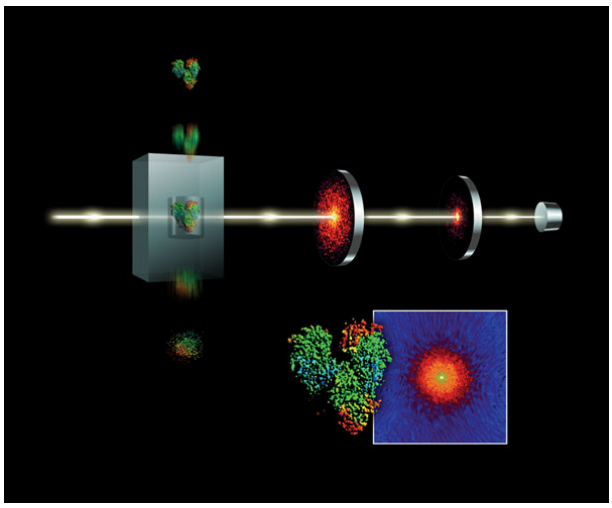

Figure 1.1: Schematic of a setup for single shot scattering imaging of non-periodic objects at an x-ray free-electron laser [12]. Molecules are injected and hit by the intense x-ray pulses. Two photon detectors record the scattering image of the sample. The molecule explodes after being hit by the x-ray beam. If the x-ray pulse is short enough, sufficient light is scattered before the sample experiences severe damage.

cant displacement of the sample has even been estimated above a pulse length of about 50-80 fs [13, 14]. Fig. 1.2 shows the results of simulations performed by Neutze et al. on the explosion of Lysozyme excited by an intense x-ray pulse [15].

Electronic damage, however, happens on a shorter time scale in very intense x-ray pulses. Fig. 1.3 shows the result of calculations for the number of scattered photons as a function of the photon fluence in a scattering experiment [16]. At high fluences, already for an x-ray pulse length of 1 fs, the number of scattered photons is not proportional to the incoming fluence anymore. Further, there is a significant difference in the scattering intensity between x-ray pulses of a length of 1 fs and 10 fs. This calculation shows that electronic damage already happens on a sub-femtosecond time scale. After initial ionization, the absorption cross section of the sample drops until an Auger decay happens. Therefore, an upper limit for the x-ray pulse length that could be used for imaging experiments without causing significant electronic damage is set by the Auger lifetimes of the sample. An increased Auger lifetime would implicate that longer x-ray pulses could be used than predicted by current damage models [16].

First experiments at LCLS have focussed on the investigation of ionization dynamics of atoms [7, 17, 18] and small molecules [9, 8] in intense x-ray pulses. Atoms exposed to intense x-ray pulses are sequentially ionized from the inside out starting with the inner-shell electrons, which exhibit the highest absorption cross section in the x-ray regime. Until the inner-shell vacancy is filled the sample becomes transiently more x-ray transparent, which is also referred to as core-level bleaching. The overall sample absorption depends sensitively on the x-ray pulse length and inner-shell vacancy lifetimes [7]. On a larger scale hot plasmas induced in solid state surfaces

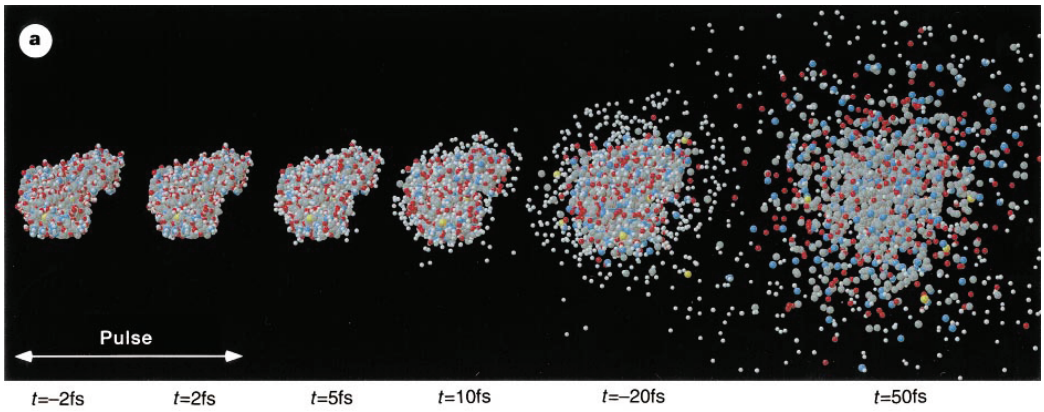

Figure 1.2: Simulation of the ion dynamics of Lysozyme after ionization with an intense x-ray pulse [15].

[11] and larger clusters were studied [10]. However, for extended nanometer-scaled systems there are theoretical predictions that there exists a size-dependence of the ionization dynamics in intense x-ray pulses, as the charges created by the x-ray pulse lead to delocalization of the valence electrons and subsequently to a reduction of the Auger rates [19].
In the present work the influence of the environment, i.e., particle size is studied in detail. As a sample system argon clusters are chosen. Rare gas clusters are ideal model systems for nanometer scaled systems in the gas phase. Their size can be easily tuned and there is no energy dissipation to surrounding media. By setting the proper photon energy, the argon L-shell could be selectively excited. The size of the nanometer sample, i.e., the influence of the environment was tuned by changing the cluster size from single atoms to about 1600 atoms or 2.5 nm in diameter. To investigate the dynamics of the absorption process the x-ray pulse length was scanned using the LCLS slotted spoiler foil [20]. The results show that there is a strong change in the Auger lifetime in the nanoplasma going from an atomic to an extended sample. Further the Auger lifetime depends on the cluster size. Larger clusters exhibit a longer Auger lifetime once they are strongly excited and ionized. An increased Auger lifetime result in reduced absorption for larger samples compared to smaller ones and atoms in intense femtosecond x-ray pulses. The results have implications for coherent imaging of nanometer-sized samples. With an increased Auger lifetime, longer x-ray pulses than predicted by current damage models [16] could be used for such experiments.

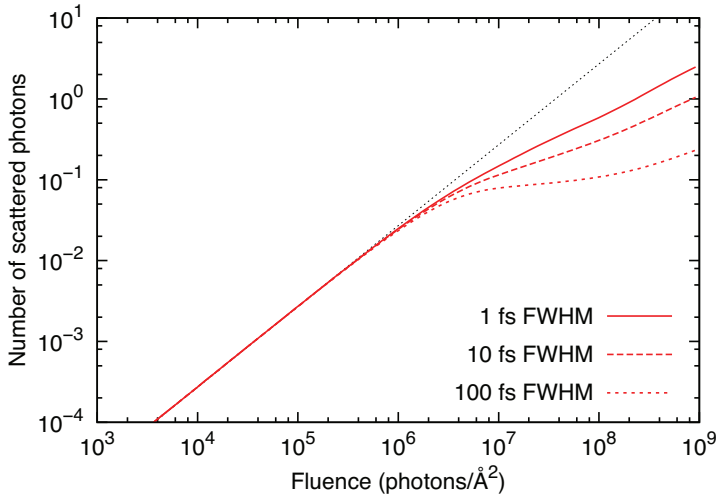

Figure 1.3: Simulation of the scattering intensity as a function of x-ray fluence and x-ray pulse length [16]. For shorter x-ray pulses the number of scattered photons is higher because the pulse is over before a significant number of Auger decays happen.

Chapter 2

Fundamental concepts

2.1 Principle of x-ray free-electron lasers and the LCLS

For the last decades synchrotron storage rings have been the most powerful x-ray sources. With the advent of short-wavelength free-electron lasers (FELs) in the past decade, light sources with a brilliance several orders of magnitude higher have become available. Fig. 2.1 shows the brilliance of several state of the art synchrotron light sources, the Free-Electron Laser Hamburg (FLASH) and the Linac Coherent Light Source (LCLS) free-electron laser. The brilliance B of a light source is defined as:

$$B = \frac{n}{A \cdot \theta \cdot t \cdot \Delta E} \tag{2.1}$$

where n is the number of photons emitted from a cross section A to a solid angle θ in a time interval t and with a spectral width of ΔE. The following section will focus on the physical and technical principles of an x-ray FEL.
All light sources mentioned in Fig. 2.1 use the same basic principle of producing light with electron beams that are transversally accelerated by a magnetic field and emit bremsstrahlung. If an electron bunch travels through a simple dipole magnet, the power of the emitted radiation is proportional to the number of electrons in the bunch. A further development in second generation synchrotron light sources resulted in placing many pairs of dipole magnets with alternating polarity into the electron beam. Fast electrons wiggle through the set of magnets on a sinusoidal trajectory and emit light on every turn. The emitted power, P_w, in such a devise, called *wiggler*, increases proportionally to the number of magnets n. The emitted spectrum is continuous with the centroid position depending on the electron energy.

$$Wiggler: \; P_w \propto n \tag{2.2}$$

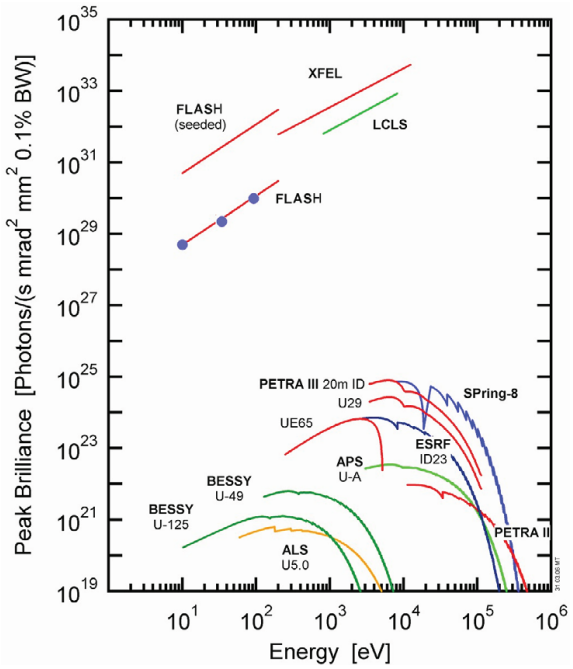

Figure 2.1: Peak brilliance of different synchrotron and SASE light sources [21].

In the 1950 years the undulator was developed as an improvement of the wiggler design [22]. Fig. 2.2 shows a schematic of an undulator. It consists, just like a wiggler, of a number of pairs of alternating dipole magnets with a distance λ_u from one dipole magnet to the next magnet of the same orientation. λ_u is called the undulator period. The distance λ_u and the magnetic field are chosen such, that the radiation emitted in every turn of the electrons in a magnet interferes constructively with the radiation emitted in the next magnet. As a result, discrete spectral peaks are emitted because only one wavelength and its higher harmonics interfere constructively. The fundamental wavelength emitted into an observation angle Φ from an electron beam with the energy γ_0 in an undulator with the period λ_u is:

$$\lambda_r = \frac{\lambda_u}{2\gamma_0^2}\left(1 + \frac{K_0}{2} + \gamma_0^2\Phi^2\right) \tag{2.3}$$

with K_0, the undulator parameter, given by:

$$K_0 = \frac{eB\lambda_u}{2\pi mc} = 0.934 B_0[Tesla]\lambda_u[cm] \tag{2.4}$$

B_0 being the magnetic field between the magnets. Tuning the wavelength of the emitted light can be achieved by varying the distance between the two poles of the magnets (gap) and therewith the

magnetic field B_0. The power of the emitted radiation P_u at the wavelength λ_r in an undulator scales with the number of magnets n in the undulator squared.

$$Undulator: \; P_u \propto n^2 \tag{2.5}$$

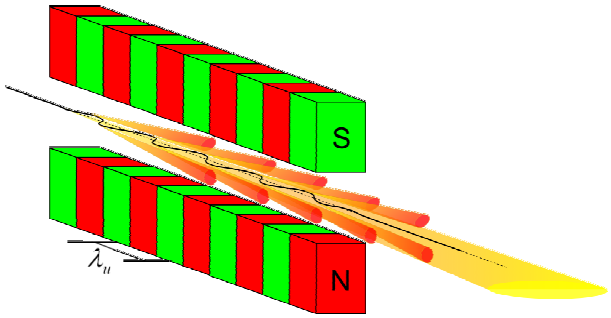

Figure 2.2: Scheme of an undulator with the period λ_u. The magnets are arranged with alternating polarity. An electron beam traverses the undulator on a sinusoidal trajectory due to the magnetic field and emits light in beam direction.

In free-electron lasers light is also produced using an undulator [23]. However, the deviation of the electron bunch in every magnet is small and the electron bunch itself is so small that the electromagnetic wave copropagating with the electron beam exchanges significant energy with the electrons. The relative phase of the electron bunch and the light field is determined by the electron energy γ_0. In the vacuum light is always faster than the electrons. Hence, the radiation overtakes the electrons in one undulator period along the beam axis by the resonant wavelength λ_l given by [23]:

$$\lambda_l = \lambda_r(\Phi = 0) = \frac{\lambda_u}{2\gamma_0^2}\left(1 + \frac{K_0}{2}\right) \tag{2.6}$$

This is also referred to as *slipage* and λ_l or $\lambda_l/2$ is referred to as *slip*. Fig. 2.3 shows the trajectory of electrons with a kinetic energy γ_0 and the light field with the wavelength λ_l in an undulator with the period λ_u. Depending on the relative phase of the electrons to the light field some electrons loose energy to the radiation and some electrons gain energy. As a result, some electrons get accelerated and some get slowed down by the light field causing a periodic density modulation of the electron bunch called *microbunching* (c.f. Fig. 2.4). These microbunches resemble dense slices of electrons separated by λ_l. The electrons in the microbunches emit radiation almost in phase and the radiation power P_{FEL} becomes proportional to the number of electrons N_e squared as opposed to an unbunched electron beam where the radiation power is proportional to N_e.

$$FEL\,Undulator: \; P_{FEL} \propto N_e^2 \tag{2.7}$$

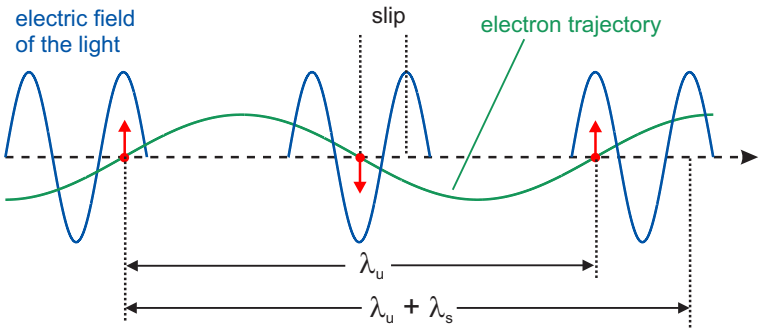

Figure 2.3: Slipage of the electron beam with respect to the light wave in an FEL undulator. In resonant condition the light wave (blue line) with the wavelength λ_l overtakes the electron beam with the energy γ_0 (green line) by λ_l in one undulator period λ_u. Electrons that are out of phase with the light field get either accelerated or slowed down resulting in a periodic modulation of the electron bunch (c.f. Fig 2.4. The red arrows indicate the velocity component of the electron beam perpendicular to the undulator axis.

Fig. 2.4 shows the structure of the electron bunch and the emitted power as a function of the distance traveled through the undulator z. In the beginning the emitted power $P(z)$ in a free-electron laser grows exponentially along the undulator with distance z:

$$P(z) = A\, P_{in}\, exp\left(\frac{2z}{L_g}\right) \tag{2.8}$$

where A is the input coupling factor that is equal to $1/9$ in 1-dimensional FEL theory [24]. P_{in} is the effective input power and L_g is the gain length, which are machine specific parameters. The exponential gain stops once the beam has lost enough energy to upset the resonant condition given in Eq. 2.6. At this point (on the right of Fig. 2.4) the radiation intensity and microbunching have reached their maximum and go into saturation. To ensure sufficient overlap between electron bunch and light field, and because the amplified wavelength λ_l depends on the emission angle (c.f. Eq. 2.3 and Eq. 2.6), the electron bunch needs to be transversely small compared to the wavelength. Furthermore, the *emittance* of the electron bunch has to be small. The emittance of an electron bunch can be understood as the volume it covers in the six dimensional phase space including the three spatial directions and their temporal derivatives.
According to Eq. 2.6, the resonant wavelength in the undulator λ_l is proportional to the inverse square of the electron energy γ_0^2. This means the resonant wavelength, i.e. the wavelength of the emitted light, can be tuned by adjusting the electron beam energy. In order to reach saturation the electron bunch has to travel long enough through the undulator. In infrared FELs the electrons go repeatedly through a short undulator and emit only a small fraction of the total radiation per cycle. This concept is called low gain FEL. A resonator is necessary to conserve the light. For x-rays it is more difficult to build normal incident mirrors for resonators or cavities that conserve the light. In addition, the repetition rate of x-ray FELs is comparably low. The light would have to be conserved in a resonator for as long as microseconds up to milliseconds

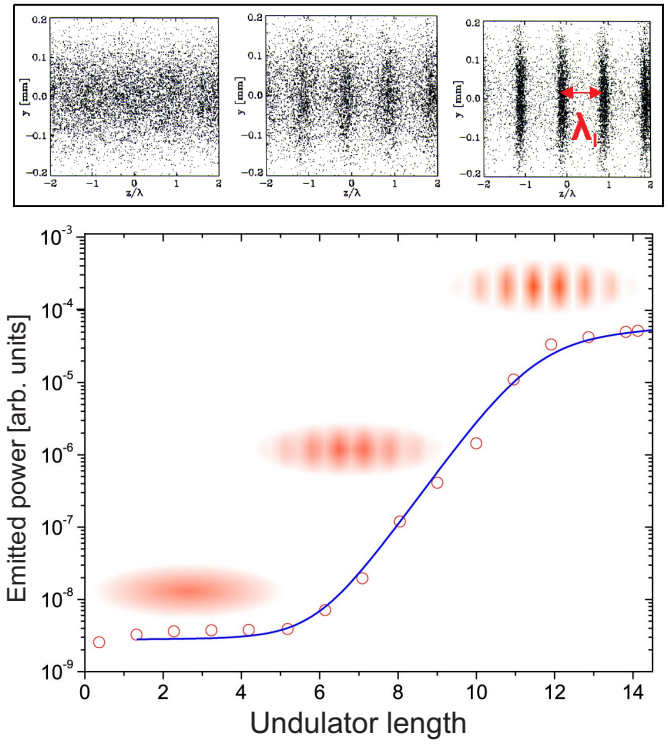

Figure 2.4: Energy of the emitted x-ray pulse vs. distance the electron beam traveled through the undulator [25]. At first, the power of the emitted light grows exponentially until it reaches saturation. Above the blue curve the structure of the electron bunch at the beginning, during the gain period and in saturation is shown. Due to interaction with the emitted light field the electron bunch gets structured to microbunches with the period of one light wavelength which enhances coherent emission.

until the next pump pulse is available. Therefore, x-ray FELs are built as high gain sources that produce all the radiation in just one pass through the undulator. The gain length, L_g, of x-ray FELs is typically on the order of meters, which makes very long undulators necessary. For the LCLS the gain length is, depending on the photon energy, between 1.5 m and 3.5 m and the undulator has a total length of 112 m. Fig. 2.5 shows a picture of the LCLS undulator. It is built into a tunnel under ground, inside a hill in order to ensure thermal stability.

In current high gain x-ray FELs the lasing process is started through spontaneous emission of the electron bunch at the beginning of the undulator. The light from the spontaneous emission is then amplified. This principle is called self amplified spontaneous emission (SASE). The initial spontaneous emission is of statistical nature and the exact wavelength is random within certain bandwidth defined by the electron energy and the magnetic field of the undulator. Even though only wavelength close to the resonant wavelength λ_l (c.f. Eq. 2.6) can be amplified, the bandwidth of SASE FELs is about 0.2 % - 1 % of the photon energy. Different parts of the electron bunch may even lase at different wavelengths. Because of the statistical nature of the initial spontaneous

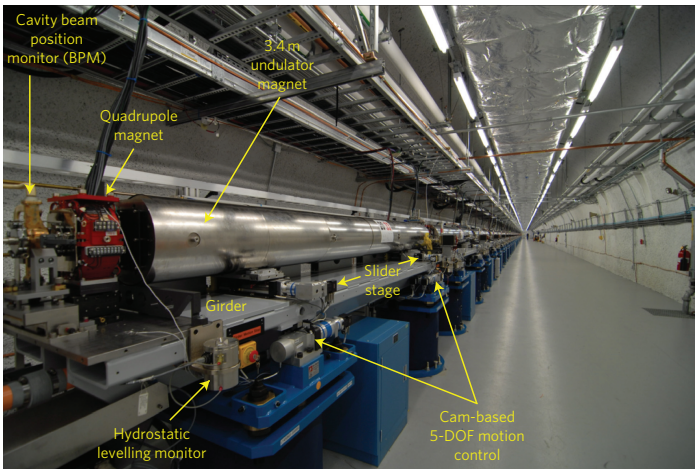

Figure 2.5: Picture of the LCLS undulator in its tunnel. The undulator consists of 33 sections with a total length of 132 m including quadrupole focusing magnets. The active undulator is 112 m long. The tunnel is located underground to avoid thermal fluctuations. The undulator segments have to be aligned very precisely with respect to each other. Between the undulator sections quadrupole magnets recompress the electron bunch transversally and beam position monitors measure its position.

emission it is also said that the lasing process in a SASE-FEL starts from *shot noise*. The SASE process induces a lot of fluctuations in the properties of the x-ray pulses. Shot-to-shot variations of 10 % - 20 % in the x-ray pulse energy are not unusual for x-ray FEL sources.
In future FEL sources, the lasing process could be stimulated with a monochromatic x-ray beam in order to decrease the bandwidth and reduce statistical fluctuations. In this process, called *seeding*, mostly the stimulating wavelength will be amplified and not the statistical shot noise [26]. This results in a much narrower bandwidth, down to 0.001% of the wavelength, and therefore in a much higher brilliance (c.f. Eq. 2.1). However it is difficult to produce short, narrow bandwidth x-ray pulses to seed an FEL. Promising concepts for seeding sources are higher harmonic generation with femtosecond NIR lasers or spontaneous emission from the first part of an undulator which is spectrally filtered with a monochromator.

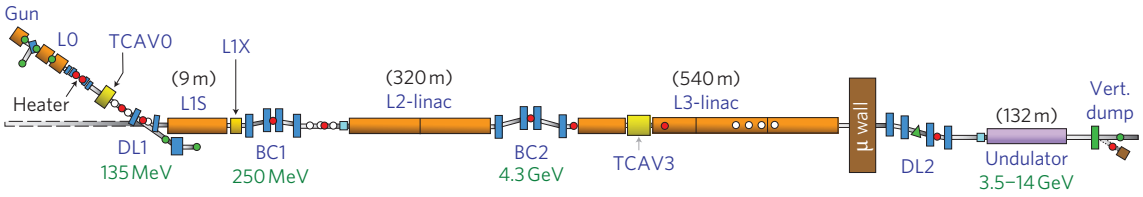

Figure 2.6: Schematic of the LCLS free-electron laser. The electron bunch is generated with a gun laser hitting a copper anode. It is accelerated in accelerator sections (L1, L2, L3) and temporally compressed with magnetic chicanes in between (BC1, BC2). The undulator is located at the end of the linear accelerator. After the undulator the electron beam is separated from the light pulse by a magnet and dumped. The front-end enclosure (FEE) with beam diagnostics, steering mirrors and attenuators as well as the experimental endstations are located downstream of the undulator.

At the time of the writing of this work there are worldwide five FEL sources in operation in the XUV or x-ray regime throughout the world. In chronological order they are:

- FLASH (**F**ree-electron **las**er **H**amburg) at DESY in Hamburg, Germany was the first FEL that produced intense light pulses in the XUV and soft x-ray regime [27]. It became available for user operation in 2005.
- SCSS (**S**pring-8 **C**ompact **S**ASE **S**ource) at the Spring-8 synchrotron facility in Japan came online in 2006 and is an XUV source [28].
- LCLS (**L**inac **C**oherent **L**ight **S**ource) was the first FEL covering x-ray photon energies from 480 eV to 12 keV and started user operation in 2009 [1]. A seeded x-ray beam at 8 keV was achieved in 2011 by using light from the first part of the undulator that is monochromatised with a diamond crystal [29].
- The FERMI FEL at the Elettra synchrotron laboratory in Trieste, Italy came online in 2011 [30]. It produces light in the XUV range and was the first short-wavelength FEL light source that uses seeding to produce intense pulses with a narrow bandwidth.
- SACLA (**S**pring-8 **a**ngstrom **c**ompact free-electron **la**ser) is the second FEL light source in the hard x-ray regime and is also located at the Spring-8 laboratory in Japan [31].

The LCLS is the light source that was used in the current work and it will be explained in more detail below. In Fig. 2.6 a schematic of the LCLS free-electron laser is depicted [1]. The electrons are produced by targeting a copper cathode with a picosecond near infra-red (NIR) laser. They are accelerated by three linear accelerator (linac) sections (L1, L2 and L3) and compressed longitudinally by two magnetic chicane bunch compressors (BC1 and BC2) after the

Property	Hard x-ray	Soft x-ray	Unit
Charge per bunch	0.02/0.04/0.25	0.02/0.04/0.25	nC
Repetition rate	120	120	Hz
FEL gain length	3.5	1.5	m
X-ray wavelength	1-1.5	6-26	Å
X-ray photon energy	0	0	eV
Photons per pulse	1.0 - 2.3	10-20	10^{12}
Pulse energy	1.5-4.0	1-4.0	mJ
Pulse length	5-100	5-500	fs
Bandwidth	0.1	0.2	%
Peak brightness	20	0.3	10^{32}

Table 2.1: Electron beam and x-ray beam parameters of the LCLS in the hard and soft x-ray regime.

first and the second linac section. A transversal cavity (TCAV3) is located in the third linac section to measure the electron bunch length. After the third linac section the electrons enter the undulator where the x-rays are produced. The x-ray light continues to the experimental endstations, while the electron beam is deflected by a magnet and dumped into a graphite block. In Tab. 2.1 the electron beam and x-ray pulse parameters of the LCLS are listed.

2.2 X-ray pulse length and slotted spoiler foil

The pulse length of the x-ray beam in a free-electron laser is determined by the length of the electron bunch in the undulator. There are two magnetic chicane bunch compressors (BC1 and BC2) that compress the bunch and maintain its longitudinal emittance. They are located after the first (L1) and the second (L2) linac sections (c.f. Fig. 2.6). Such a magnetic chicane bunch compressor is depicted in Fig. 2.7 a). It consists of four dipole magnets (green triangles). The electrons in the bunch have a velocity distribution that results in bunch spreading over time along the linac path. When the electrons enter the first magnet in the bunch compressor, they are deflected perpendicular to their velocity vector by the Lorentz force. Faster electrons travel transversally further compared to the slower electrons, leading to a longer trajectory in the bunch compressor. The slower electrons on their shorter trajectory can catch up with the faster ones. When the electrons are deflected back to their initial trajectory the bunch is shorter in time, i.e. compressed.

By tuning the magnetic field and the position of the magnets in the bunch compressor the electron bunch length, and therefore the x-ray pulse length, can be varied. Changing the compression, however, changes the properties of the electron bunch and may affect the lasing process in the undulator. More importantly, for a certain bunch charge, i.e. number of electrons in the

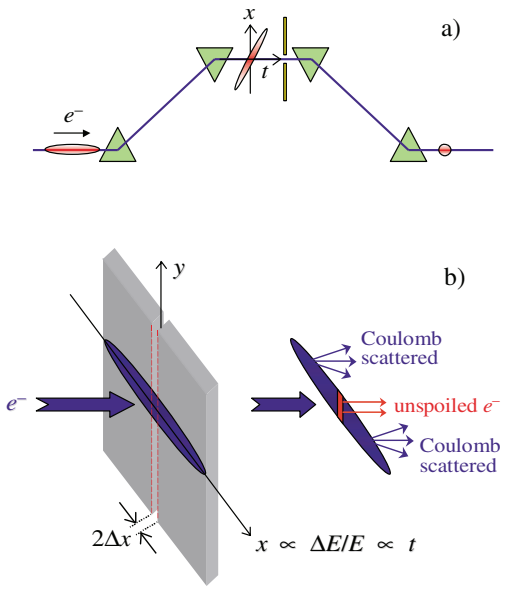

Figure 2.7: a) Schematic of a magnetic bunch compressor with the electron trajectory (blue line). The temporally expanded electron bunch (red) is deflected by magnets (green). The magnetic field vector is pointing out of the drawing plane. Faster electrons at the front of the bunch travel further out then slower ones which translates the temporal expansion of the bunch into a spacial expansion. The spoiler foil (yellow) spoils the emittance of the bunch that does not go through the small slot. Afterwards the bunch is deflected back on its original trajectory translating the spacial expansion back into a temporal expansion. Only the short part of the bunch that is not spoiled is lasing in the undulator. b) Detailed scheme of the spatially expanded electron bunch and the slotted foil. Most of the bunch gets Coulomb scattered when crossing the foil. Only a small portion (red) of the electron bunch still has a high enough emittance to lase [20].

bunch, only a limited range of bunch lengths are possible. Varying the bunch charge requires major tuning of the accelerator which may sacrifice the reproducibility of measurements in a experiment. A novel method to reduce and tune the pulse length without affecting the bunch charge and compression is the so called *slotted spoiler* technique [20]. With the slotted spoiler a part of the electron bunch is spoiled so that it cannot contribute to the lasing process anymore, making the x-ray pulse shorter. The principle of slotted spoiler technique is explained in the following.

When the electron bunch is deviated from its initial trajectory in the bunch compressor, the longitudinal distribution of the bunch in front of the bunch compressor is converted into a transversal distribution between the 2nd and 3rd magnet. At this point a thin Aluminium foil with a thickness of about $15\,\mu m$ is inserted into the beam inside the second bunch compressor (BC2) of the LCLS (c.f. Fig. 2.6). This foil has a vertical slot smaller than the transversal extension of the electron bunch. In Fig. 2.7 a this foil is shown as a black vertical line. When the

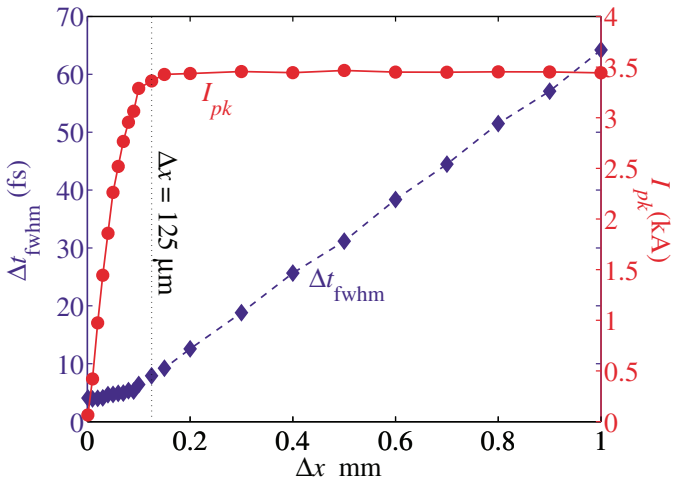

Figure 2.8: Simulation of the x-ray pulse length depending on the slot width of the slotted spoiler [20]. The graph shows the FWHM of the x-ray pulse (blue) and peak current of the electron bunch (red) vs. half width of the slotted foil. The resulting x-ray pulse length has a linear behavior with the slot width.

electron bunch crosses the slotted foil (c.f. Fig. 2.7 b) the electrons encountering the Aluminium foil are Coulomb scattered while the electrons that pass through the opening of the slot are left undisturbed. Coulomb scattering disturbs the trajectory of the electrons slightly and therefore spoils the emittance of this part of the electron bunch. The spoiled part of the electron bunch will cease lasing when it travels through the undulator. After the slotted spoiler foil, the electron bunch is deflected back to its initial trajectory. It will continue to the undulator and only the small central part of unspoiled electrons will lase, resulting in a much shorter x-ray pulse. The size of the unspoiled part of the electron bunch and therefore the length of the x-ray pulse can be tuned by changing the width of the slot.

In Fig. 2.8 the blue curve shows the simulated x-ray pulse length, as a function of the spoiler width [20]. The x-ray pulse length depends linearly on the slot width over most of the range allowing for fairly simple tuning of the pulse length. Besides tuning the pulse length, the slotted spoiler method allows much shorter x-ray pulses than the shortest possible electron bunch, down to fractions of femtoseconds [32].

Fig. 2.9 shows a picture and a schematic of the slotted foil installed in the LCLS. The lowermost single slot was used to tune the pulse length for the experiments in this work. It is V-shaped so that the width can be changed by moving it perpendicular to the electron beam. Above the single slot, two double slots can be seen that allow producing two temporally separated x-ray pulses with a femtosecond delay for x-ray pump – x-ray probe experiments [33].

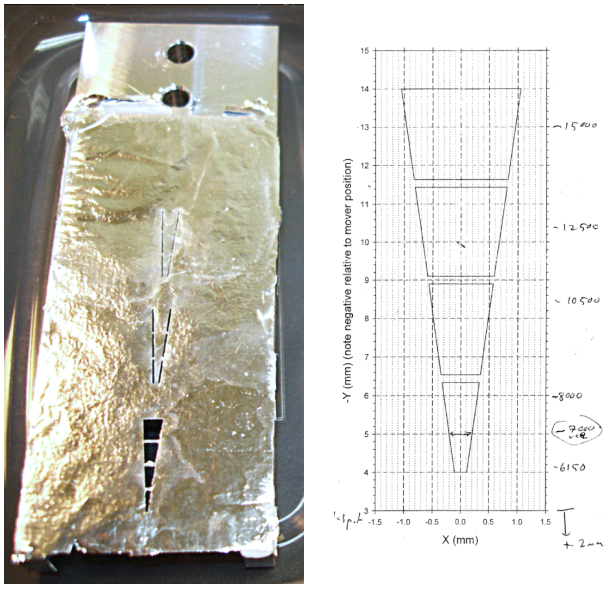

Figure 2.9: Left: picture of the LCLS slotted spoiler foil. The lowermost slot is the single slot. It is V-shaped to adjust the pulse length of a single pulse. The slots above it are double slots to produce two x-ray pulses separated in time. Right: drawing of the single slot

2.3 Rare gas clusters

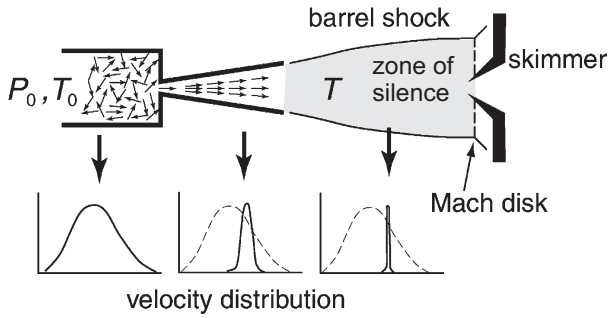

Figure 2.10: Schematic of a supersonic expansion of a gas with the temperature T_0 and the backing pressure P_0. The region of free flow (zone of silence) is limited by the barrel shock to the sides and the Mach disk downstream [34]. The background pressure has to be low enough so that the Mach disk is located downstream of the interaction region or at least downstream of the first skimmer. At the bottom of the figure, the velocity distribution is depicted for different parts of the flow. The gas cools down traveling downstream from the nozzle.

The sample system that was studied in the experiments shown in the present work are rare gas clusters, and more specifically, argon clusters. Rare gas clusters can be liquid or solid an usually consist of a few up to millions of atoms [35, 36]. They are a widely used model system to study light-matter interactions in intense laser pulses from the infrared to the x-ray regime [37, 38, 39, 40, 41, 42, 43, 44]. As rare gases have closed electron shells they form only weak Van-der-Waals bonds with binding energies between 0.8 meV for Helium and 130 meV for Xenon. Therefore, the clusters can only exist at cryogenic temperatures. When they are produces through supersonic expansion the atoms forming the cluster usually arrange in an energetically favorable sphere-like shape. Most of the rare gases, including argon, form solid clusters, only helium clusters and small neon clusters can be liquid. Solid clusters usually exhibit an icosahedral structure when they are small while clusters above a size of a few thousand atoms exhibit an fcc structure with possible stacking faults [45, 46]. The condensation of atoms and molecules - i.e. cluster formation - in a supersonic jet was first studied in 1956 for thermonuclear fuel applications [47] and later extensively studied [48, 49]. In the following section an overview about the production of rare gas clusters is given.

Rare gas clusters are generally produced by supersonic expansion of the sample gas through a nozzle into the vacuum. Their size can easily be tuned by adjusting the expansion parameters [48, 50, 51]. Fig. 2.10 shows a schematic of a nozzle and the gas expansion [34, 52]. The cluster formation process involves a gas with a backing pressure p_0 and the temperature T_0 expanding through a small nozzle with a diameter d into the vacuum with a background pressure p_b. If the ratio p_0/p_b is greater than the critical value G which is smaller than 2.1 for all gases, the expansion velocity v can exceed the local speed of sound c. Then the Mach number M, defined

as the ratio v/c, is greater than 1. Accordingly, the gas travels faster than information can be transferred in the medium. The gas in this *zone of silence* does not "know" about boundary conditions and must not adjust. It has almost no energy exchange with the surrounding vacuum and the expansion process can be considered adiabatic or isentropic. With the local speed of sound $c = \sqrt{\gamma kT/m}$ and $\gamma = c_p/c_v$, the ratio of specific heat at constant pressure c_p and constant volume c_v which is independent of the temperature for an atomic gas, M can be described as:

$$M = A\left(\frac{x_M}{d}\right)^{\gamma-1} \tag{2.9}$$

with $A = 3.20$ for atomic gases and x_M being the distance from the nozzle. M increases downstream along the beam direction. At the boundaries of the zone of silence, M drops below 1 and the gas suddenly has to meet the boundary conditions resulting in very thin nonisentropic regions of large density, pressure, temperature and velocity gradients. These zones are called *barrel shock* to the sides, and *Mach disk* downstream of the zone of silence.
In an experiment, the Mach disk needs to be downstream of the interaction region to achieve an undisturbed flow. The distance from the nozzle to the Mach disk x_{MD} in terms of nozzle diameters d is:

$$\frac{x_{MD}}{d} = 0.67\left(\frac{p_0}{p_b}\right)^{\frac{1}{2}} \tag{2.10}$$

For a certain backing pressure p_b, the background pressure p_0 needs to be low enough to move it far enough downstream. Usually a skimmer is placed close to the nozzle (c.f. Fig. 2.10) separating the vacuum in the nozzle chamber from the interaction region or further differential pumping. Because the background pressure in the vacuum section behind the skimmer is lower, the Mach disk shifts further away from the nozzle. Skimmers are small apertures that are conical or trumpet shaped to avoid turbulence and maximize the transmission. They cut out the center part of the gas jet where the cluster density is highest.
In the zone of silence where the flow is isentropic, Bernoulli's equation relates the enthalpy in the stagnation region (H_0) with that of the flow (H) and with the kinetic energy of the directed mass of the flow [49, 52]:

$$H_0 = H + \frac{1}{2}mv^2 = c_p T + \frac{1}{2}mv^2 = c_p T_0 \tag{2.11}$$

where c_p is (5/2)k for a monoatomic gas and T is the temperature of the expanding gas. With the Boltzmann constant $k = c_p - c_v$ and M being the Mach number, Eq. 2.11 can be expressed as follows:

$$T = T_0\left(1 + \frac{1}{2}(\gamma-1)M^2\right)^{-1} \tag{2.12}$$

Eq. 2.12 shows that the gas is cooled during the expansion. When the gas is cold enough the

cluster formation process starts with a three-body collisions where a dimer is formed and the released binding energy is carried away by the third atom as kinetic energy. The dimers act as condensation nuclei for further cluster growth. Depending on the ratio of atoms to clusters, the clusters grow further, either by addition of monomers or cluster-cluster aggregations [34, 53]. Concurrent to the temperature also the gas density decreases as the gas expands. From a hydrodynamic expansion at the nozzle, where the gas density is close to the density in the backing volume, the expansion changes to a molecular flow further downstream. The cluster formation takes place in the hydrodynamic expansion region and discontinues in the molecular flow region.

In the phase diagram shown in Fig. 2.11 the cluster formation can be seen as a gas to liquid/solid transition. Point A represents the gas before the expansion. During the expansion it follows the adiabatic line down to point B where it crosses the vapor pressure curve. From there the gas expands further along an adiabatic line into the nonequilibrium so called *supersaturated* state at point C. Then the formation and growth of clusters starts bringing the gas back to the equilibrium vapor pressure curve $p_v(t)$.

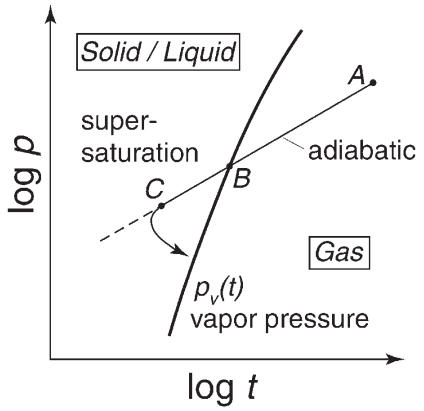

Figure 2.11: Phase diagram with the condensation path of a gas in a supersonic expansion [34]. From the initial point A the gas expands and cools down to point B where it crosses the vapor pressure curve. It expands and and cools further to nonequilibrium *supersaturated* state at point C. The onset of condensation an growth of clusters brings it back to the vapor pressure curve $p_v(t)$.

A small particle or cluster of radius r has a vapor pressure P_r larger than vapor pressure P_0 of a plane surface:

$$ln\,\frac{P_r}{P_o} = \frac{2\,\sigma\,m}{k\,T\,\rho}\,\frac{1}{r} \tag{2.13}$$

where σ is the surface tension of the small particle and ρ is its density. As the radius r increases, the vapor pressure decreases. A cluster having a radius greater than the critical radius r^* grows while a smaller one evaporates. Therefore there are two peaks in the mass spectrum of the cluster

	Helium	Neon	Argon	Krypton	Xenon
K	3.85	185	1646	2980	5554

Table 2.2: Material specific cluster parameter K for the rare gases [55].

jet: an exponential decay distribution of small clusters and a wide distribution of larger clusters. The average cluster size, $\langle N \rangle$, for a certain gas and nozzle, with specific expansion parameters p_b and T_0, can be determined using the empiric Hagena scaling laws [48, 54, 50]. The so called *Hagena parameter* Γ^* is defined as:

$$\Gamma^* = K\, p_b\, d_{eq}^{q}\, T_0^{0.25q-1.5} \tag{2.14}$$

K and q are gas specific parameters, d_{eq} is the equivalent nozzle diameter. For pinhole nozzles:

$$d_{eq} = d \tag{2.15}$$

and for conical nozzles with a half opening angle ϕ:

$$d_{eq} = d\,\frac{tan\phi_0}{tan\phi} = 0.719\frac{d}{tan(\phi)} \tag{2.16}$$

with ϕ_0 being the half opening angle of the free expansion. While q was experimentally determined to be 0.85 for all the rare gases, K depends on gas specific properties (c.f. table 2.2). For rare gases Eq 2.14 reduces to:

$$\Gamma^* = \frac{K\, p_b[mbar]\, d_{eq}^{0.85}[\mu m]}{T^{2.2875}[K]} \tag{2.17}$$

Gas jet setups with the same Hagena parameter Γ^* will produce the same average cluster size $\langle N \rangle$. This average size can be determined from the Hagena parameter Γ^* as follows.
For $\Gamma^* < 350$ no condensation is observed.
For $350 \leq \Gamma^* < 1800$ the average size $\langle N \rangle$ is found to be:

$$\langle N \rangle = 38.4\,(\Gamma^*/1000)^{1.64} \tag{2.18}$$

and for $\Gamma^* \geq 1800$ $\langle N \rangle$ is:

$$\langle N \rangle = 33\,(\Gamma^*/1000)^{2.35} \tag{2.19}$$

Every supersonic cluster jet will always produce a size distribution. The centroid of this distribution is given by the average size $\langle N \rangle$ calculated from the Hagena scaling law. In good

approximation the width of this distribution is about half the average size $\langle N \rangle$.
For many purposes the size distribution is of secondary importance because the main interest lies in determining a size dependent effect. Even though a size distribution is investigated the whole distribution shifts when the expansion parameters are changed. To perform experiments with clusters of a single size there are two possible methods. The first method is to filter the clusters by mass using special techniques [56]. The second method is to reduce the density of the cluster jet and perform experiments on single clusters. In these types of experiments some information about the size has to be collected with every single shot. This has become possible with the advent of free-electron laser sources [10, 57].

2.4 X-ray photoionization and relaxation of inner-shell holes

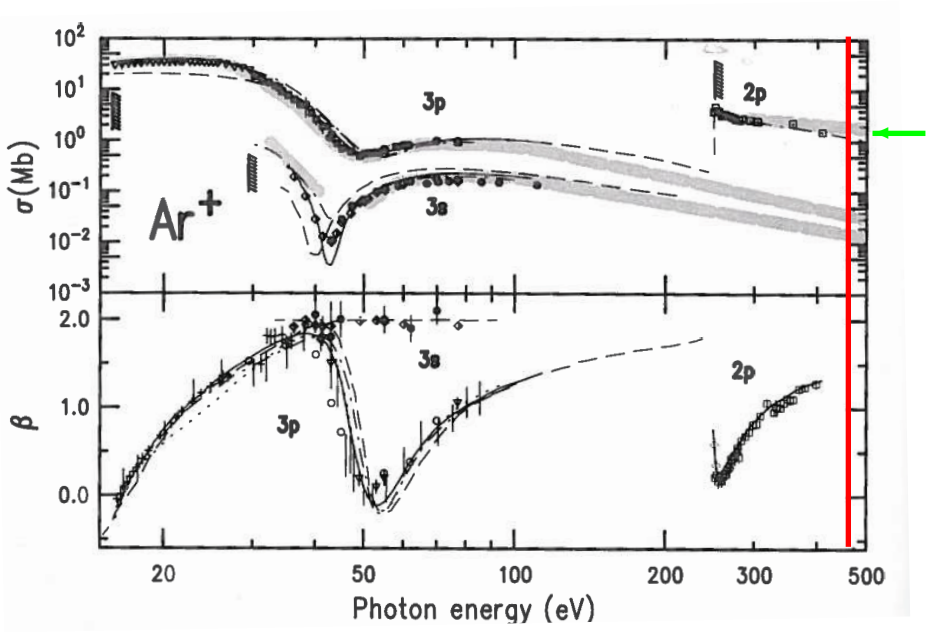

Figure 2.12: Measured linear photoionization cross section of atomic argon [58]. The photon energy of 480 eV that was used for the experiments in this work is marked with a red line. The respective photoabsorption cross section of the argon 2p shell is marked with a green line.

Photoionization describes the absorption of photons by an atom with the result that one or more electrons are excited into the continuum, i.e. removed from the atom. In the x-ray/XUV wavelength range the absorption of one photon is enough to ionize an atom. The ionization cross section for a certain electronic shell depends strongly on the x-ray photon energy. Usually the electronic levels with the highest binding energy below the photon energy exhibits the highest absorption cross section per electron. Furthermore, the total absorption cross section for an electronic level is roughly proportional to the number of electrons in this level. As a result of the photoionization process, the atomic Coulomb potential is reconfigured and other electrons can end up above the ionization potential in bound states (shake-up) or in the continuum (shake-off). Fig. 2.12 shows the experimentally determined ionization cross sections for argon, and Tab. 2.3 shows differential ionization cross sections of argon at 480 eV as calculated with the Los Alamos Atomic Physics Code [59]. The photon energy of 480 eV used in this study is above both the argon 2s and 2p levels.

If an electron is removed from an inner-shell the remaining hole leaves the atom in an excited state. Inner-shell holes are usually filled with higher-lying electrons on a femtosecond timescale.

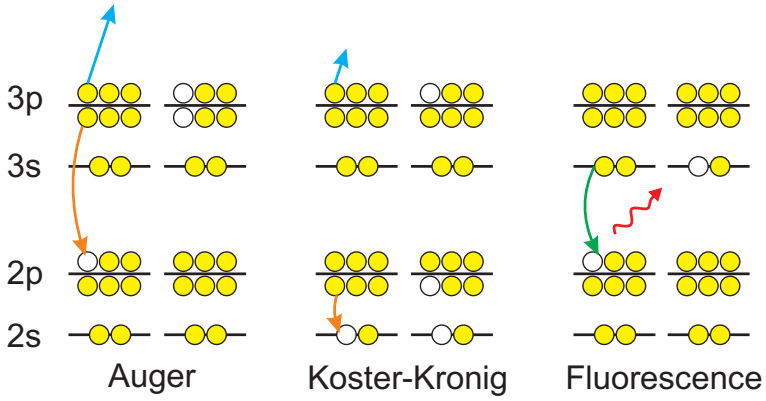

Figure 2.13: Possible decay channels of an inner-shell hole. Auger decay (left): The inner-shell hole is filled by an electron from a higher shell and and electron from this or an even higher shell is emitted. Koster-Kronig decay (middle): The inner-shell hole is filled with an electron from the same shell and an electron from a higher shell is emitted. Fluorescence (right): The inner-shell hole is filled by any higher electron and the released energy is emitted as a fluorescence photon is emitted.

shell	cross section [Mbarn]	Ionization potential [eV]
2s	0.206	328.0
2p	1.05	249.0
3s	0.027	34.3
3p	0.065	15.6

Table 2.3: Differential photoabsorption cross sections and Ionization potentials of argon at 480 eV

Fig. 2.13 illustrates the three most likely inner-shell hole decay channels. In an *Auger* decay [60, 61] the hole is filled with an electron from a higher lying shell. The released energy is transferred to another electron from that shell or a higher shell that is ejected. This results in two holes in higher lying shells. Similarly, the inner-shell holes can also be filled by a higher-lying electron of the same shell and an electron from a higher shell is ejected. This decay channel is called *Koster-Kronig* decay and results in one hole in the inner-shell where the initial hole was produced and another hole in an higher lying shell. The third important decay channel is the *fluorescence* decay where the inner-shell hole is filled by higher lying electron and the released energy is emitted as a photon. The yield of each of the three channels for a certain hole in a certain atom depends on its electronic configuration and where the hole is created. In general the probability for a fluorescence decay increases compared to an Auger decay and a Koster-Kronig decay with the energy difference between the hole and the next energetic higher occupied electronic level. In Fig. 2.14 the relative yield for an L-shell hole is plotted vs. the core charge Z of the elements. The probability for fluorescence (red lines) is very low for light elements and increases monotonically with Z for all three levels. For the L2-shell and L3-shell the Auger yield

(blue lines) is almost 1 for low Z and decreases with Z. The L3-shell cannot decay via Koster Kronig (green lines) and the probability for a Koster-Kronig decay in an L2 shell is below 20 % for all elements. For the L1-shell, Koster-Kronig decay and Auger decay are competing. Their relative probability depends on the electronic configuration of the atom. argon with a core charge of Z=18 is marked with black vertical line in Fig. 2.14. Fluorescence is almost irrelevant for all levels of the argon L-shell. Holes in the L2-shell and L3-shell most likely decay via Auger decay resulting in two valence holes. If a hole in the L1-shell is created, it will decay with a probability of about 95 % via Koster-Kronig decay, resulting in one hole in the valence shell and one in the L2-shell or L3-shell. It is important to note that a Koster-Kronig decay of a L1-shell hole results in another L-shell hole and the ejection of a valence electron. Therefore it doesn't significantly change the absorption cross section for photon energies above the L1 edge.

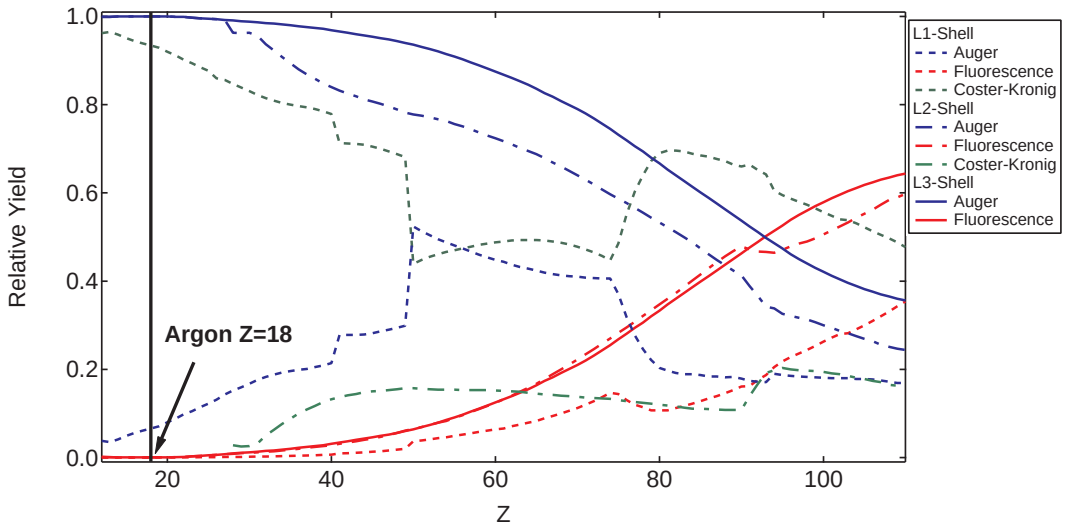

Figure 2.14: Auger, Fluorescence and Koster-Kronig yields for the L-shell of different elements. For argon (Z=18) Fluorescence is negligible for all levels. For L2 and L3 Auger decay is clearly dominating. For L1 a Koster-Kronig decay ist most likely which then results in and L2 or L3 hole [62].

2.5 Field effects in x-ray ionization

Conventional x-ray and XUV sources, e.g. synchrotron storage rings, x-ray tubes or higher harmonic generation, produce light beams that are not intense enough to induce non-linear absorption in a sample. With the advent of free-electron lasers producing x-ray pulses with power densities up to 10^{18} W/cm^2 this has become possible. However there are few experimental results on non-linear absorption in the x-ray regime available. The following section gives an overview about the current state of research about ionization mechanisms of atomic systems in

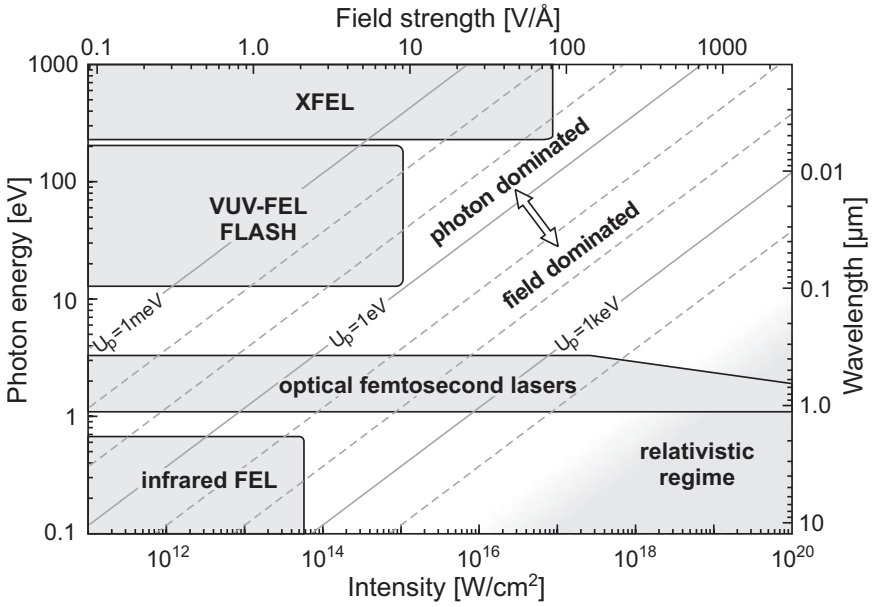

Figure 2.15: Ponderomotive potential U_p as a function of Intensity and Photon energy [41]. The diagonal lines represent areas with the same ponderomotive potential. Different types of light sources are marked as grey shaded areas.

intense x-ray pulses.

Ionization with intense x-ray pulses is fundamentally different from ionization with intense optical pulses. With intense optical femtosecond pulses it is possible to transfer enough energy to an electron with the electric field of the laser to drive it out of the atomic Coulomb potential. If the laser intensity is high enough the atomic Coulomb potential is deformed and formerly bound electrons can tunnel out of it (tunnel-ionization) or can end up above the Coulomb barrier and leave the atom (over-the-barrier ionization). For x-rays however, the field frequency is much higher, and therefore, the time the electrons are accelerated in one direction is much smaller until they are turned around by the field again. Similarly, the influence of the light field on the atomic Coulomb potential is much smaller with x-ray intensities currently available. As a result the absorption of an intense x-ray pulse can be described perturbative model with quasi-static Coulomb potential. From another point of view, the light of intense x-ray pulse can be described by its photon character rather than its field character.

To get a more quantitative understanding, two quantities that are commonly used to describe the strength of field effects in the absorption of laser pulses are compared for an intense x-ray and optical laser pulse in the following. Namely the *ponderomotive potential* U_p and the Keldysh parameter γ. The *ponderomotive potential* U_p also referred to as *quiver energy* gives a quantitative measure of the electron motion induced by the electric field. It is defined as:

$$U_p = \frac{E^2}{4\,\omega^2} \tag{2.20}$$

where E is the field strength and ω is the field frequency. As an example, for soft x-ray pulses of the LCLS with a power density of 10^{17} W/cm^2 and a photon energy of 1 keV these quantities are roughly: E,≈ 2 and $\omega \approx 37$, both in atomic units. For an near infra-red (NIR) laser with a power density of 10^{15} W/cm^2 and a photon energy of 1 eV they are: E ≈ 0.17 and $\omega \approx 0.037$. This results in a ponderomotive potential for both light sources:

$$LCLS : U_p = \frac{2^2}{4 \cdot (37)^2} = 0.0007\,au \approx 20\,meV \tag{2.21}$$

$$NIR - laser : U_p = \frac{0.17^2}{4 \cdot (0.037)^2} = 5\,au \approx 140\,eV \tag{2.22}$$

The ponderomotive potential for pulses of the LCLS is about four orders of magnitude lower than for pulses of a typical NIR femtosecond laser. As a result the energy that can be transferred to an electron by the light field is four orders of magnitude lower for the LCLS in comparison to a typical NIR laser. In Fig. 2.15 the ponderomotive potential U_p is plotted as diagonal lines as a function of light intensity and wavelength. Different types of light sources are marked as grey shaded areas. While optical lasers easily reach into the field dominated area current short-wavelength sources are clearly on the photon dominated side.
To describe the influence of a laser field on the Coulomb potential of an atom the Keldysh parameter γ [63] is commonly used. For $\gamma < 1$ the field of the atom is significantly influenced by the laser field and the interaction has to be described in a non-perturbative picture while for $\gamma > 1$ the influence of the laser field is minor and the interaction can be described in a perturbative picture with a quasi-static atomic Coulomb potential. The Keldysh parameter is defined as:

$$\gamma = \frac{optical\,frequency}{tunneling\,frequency} = \sqrt{\frac{E_b}{2\,U_p}} \tag{2.23}$$

where E_b is the binding energy of the electron. For the LCLS, where inner-shell binding energies are typically a few hundred eV and above, this results in:

$$\gamma = \sqrt{\frac{400\,eV}{2 \cdot 20\,meV}} \approx 100 \tag{2.24}$$

For NIR lasers, with valence binding energies of 5-15 eV the Keldysh parameter is:

$$\gamma = \sqrt{\frac{10\,eV}{2 \cdot 140\,eV}} \approx 0.2 \tag{2.25}$$

Regarding these numbers the interaction of intense x-ray pulses from current FEL light sources can be understood in a perturbative picture. It can be described by single photons absorption

and the field character of the light plays a minor role. According to Eq. 2.23 x-ray power densities of about 10^{21} W/cm^2 would be needed to reach a regime where tunnel ionization of inner-shell electrons occurs. This is about 3 to 4 orders of magnitude more than LCLS can currently deliver. In Fig. 2.15 the photon energy is plotted vs. laser intensity [41]. The ponderomotive potential is marked as diagonal lines. The regime where the absorption can be understood in a photon absorption picture is on the upper left side while the field dominated region is on the lower right side.

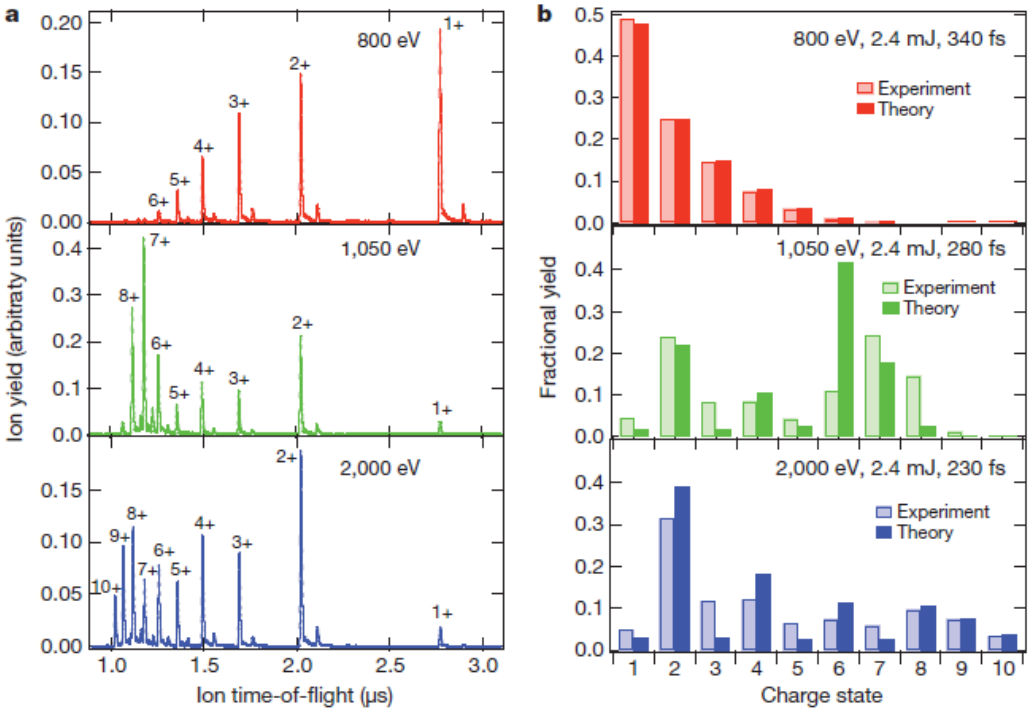

Figure 2.16: Ionization of neon with intense x-ray pulses at different photon energies of 800 eV (red,top), 1050 eV (green,middle) and 2000 eV (blue,bottom), a pulse length of 230 fs to 340 fs and a pulse energy of 2.4 mJ [7]. Experimental ion tof spectra (left) are compared to results of a rate equation model (right). The diameter of the focus was estimated to 2 μm^2.

2.6 Nonlinear x-ray absorption

The first experimental study of core-level ionization with intense x-ray pulses at the LCLS was performed by Young et al. [7] on neon atoms. Concurrent with other studies at LCLS [18, 9], the observed effects can be sufficiently explained by sequential absorption of x-ray photons. No indications of simultaneous multi-photon absorption were observed. In addiation to the experimental data theoretical calculations were performed. A rate equation model was developed including

calculated ionization cross sections, Auger rates and fluorescence rates of neon. Fig. 2.16 shows the measured ion time-of-flight (tof) spectra and ion yields compared to the theoretical data. Except for some deviations that can be explained by missing double Auger and shake-off probabilities in the model, the simulations agree very well with the experiment. In more detail, Fig. 2.16 shows tof spectra of atomic neon irradiated with intense x-ray pulses at different photon energies between 800 eV and 2000 eV and a pulse energy of 2.4 mJ. Fig. 2.17 illustrates the most likely ionization pathways that lead to the highest observed charge state, observed in the spectra shown in Fig. 2.16, for the different photon energies.

The red curve in Fig. 2.16 is recorded at a photon energy of 800 eV, below the neon 1s ionization potential of 870 eV. Neon 1s core-electrons cannot be ionized and only valance ionization with a relatively low cross section occurs. The valence electrons are removed by sequential photoionization and charge states up to Ne^{6+} are observed. Due to the low valence ionization cross section the ionization process does not saturate and the yield of the ions is monotonically decreasing as a function of increasing charge states.

The green curve in Fig. 2.16 shows data taken with a photon energy of 1050 eV above the neon 1s edge, where the neon 1s electrons exhibit the highest absorption cross section. Compared to the spectrum at 800 eV the ion yield changes dramatically. Charge states up to Ne^{8+} are observed with a maximum yield at Ne^{7+}. The highest observed charge state is Ne^{8+} because the photon energy of 1050 eV is above the $Ne^{7+} \rightarrow Ne^{8+}$ ground state ionization potential (240 eV [59]) but below the $Ne^{8+} \rightarrow Ne^{9+}$ ground state ionization potential (1196 eV [59]). In other words the photon energy is not high enough to remove one of the two 1s electrons if all the valence electrons are already stripped of.

For a neon 1s core-hole the Auger decay is the most likely decay path resulting in at least two charges per atom. Therefore the Ne^{1+} signal is very small resulting only from weak valence ionization and fluorescence decay following 1s ionization. There are two main reasons for the much higher average charge state compared to 800 eV photon energy. First, the neon 1s absorption cross section at 1050 eV is much higher than the valence absorption cross section at 800 eV, leading to more absorbed photons per atom. Second, the most likely ionization pathway at 1050 eV is cycles of core-ionization followed by an Auger decay that refills the hole. This results in two charges per atom per absorbed photon. The ionization pathway leading to Ne^{8+} in Fig. 2.17 shows that the photoionization–Auger decay cycles stop at Ne^{6+}. At this point the neon 1s ground state ionization potential with 1196 eV is higher than the photon energy. Higher charge states are produced by subsequent valence ionization until only the two core-electrons are left.

The tof spectrum represented by a blue line in Fig. 2.16 is recorded at a photon energy of 2000 eV, above the ground state ionization potential of $Ne^{9+} \rightarrow Ne^{10+}$ at 1362 eV [59]. All electrons can be stripped of the neon atoms through cycles of core ionization and subsequent Auger decay. Charge states up to Ne^{10+} are observed.

It is noted that the ion spectra shown in Fig. 2.16 are integrated over the whole volume of the x-ray focus. Higher charge states from atoms that have absorbed many photons and that undergo

the ionization pathways shown in Fig. 2.17 are mostly produced in the central, most intense region of the focal volume. Accordingly, lower charge states from atoms that have absorbed only few photons are mostly produced in the outer region of the focal volume, where the x-ray intensities are lower.

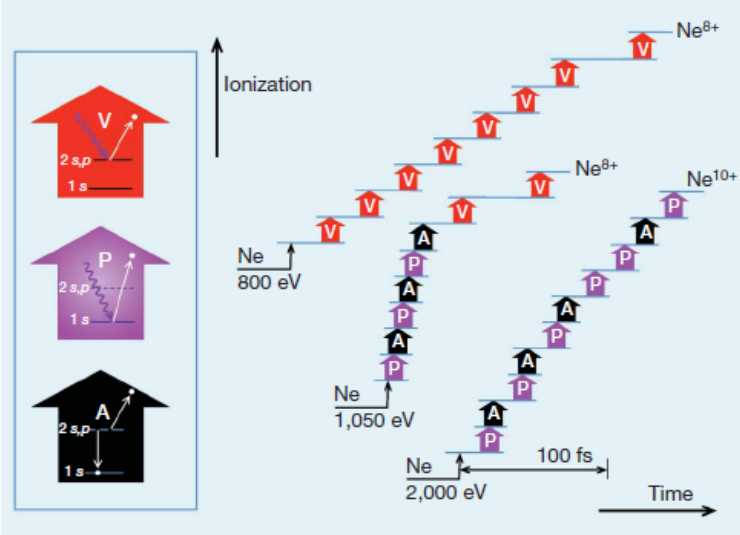

Figure 2.17: Ionization pathways for the highest charge states observed in the spectra shown Fig. 2.16 according to the photon energy. The possible Ionization steps are valence photoionization "V", core photoionization "P" and ionization via Auger decay "A" [7].

2.7 Induced x-ray transparency

An important aspect of the ionization with intense x-ray pulses are the dynamics of the participating phenomena. While the photoabsorption happens on time scales much shorter than the x-ray pulses, the Auger lifetimes are comparable to the x-ray pulse lengths. If one of the inner-shell electrons is removed by the leading part of the x-ray pulse the absorption cross section is lowered due to the missing electron. The atom is transiently more transparent to the rest of the pulse until the hole is filled via Auger decay. In other words, the x-ray pulse induces transparency in the sample, what is also referred to as *bleaching* [7, 8]. In a temporal average it is more likely for a longer pulse to see filled inner-shells than for a shorter pulse with the same number of photons. That is, the atom is more transparent to a shorter pulse than to a longer pulse if both pulses consist of the same number of photons. Vice versa, the Auger lifetimes have an influence on the absorption. An atomic system that has longer Auger lifetimes, on average, absorbs less photons from a pulse with certain length than the same system with shorter lifetimes. As a result

the Auger rates of an atomic system and the x-ray pulse length are critical parameters for the absorption of intense x-ray pulses. In contrast to pulses of optical light, for x-rays, longer pulses can be absorbed more efficiently than shorter pulses. In Fig. 2.18 the result of the pulse length dependent ionization of neon is shown. This data set has been recorded in the high field physics (HFP) chamber of the AMO endstation as a preliminary study for this work and to evaluate the performance of the slotted spoiler foil.
In this experiment atomic neon was irradiated with intense x-ray pulses at a photon energy of 1200 eV and a pulse length between 15 fs and 75 fs while the pulse energy was held constant at 0.3 mJ for all pulse lengths. In the top panel of Fig. 2.18 the tof spectra for neon are shown for three different pulse lengths. In the lower left panel of Fig. 2.18 the relative abundance of the neon charge states for the 30 fs and 80 fs pulse length compared to the 15 fs pulse length are displayed. The charge states higher than Ne^{4+} are less abundant for shorter x-ray pulses. As a result, the average charge state (in the lower right panel of Fig. 2.18) decreases with shorter pulse length. This can be understood as an increase in transparency as explained above. Ne^{4+} and lower charge states are mostly unaffected as they are produced in the outer part of the focus where only 1-2 photons per atom are absorbed and therefore the induced transparency is only a weak effect.

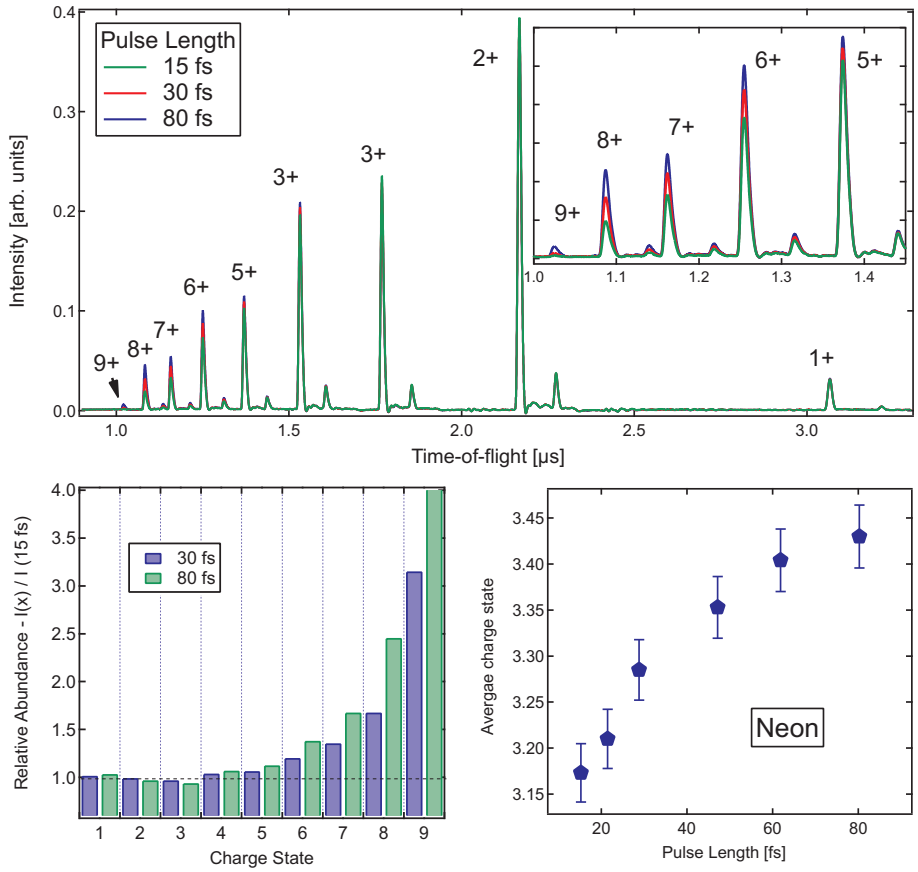

Figure 2.18: Top: Ion spectra of neon for different pulse length at pulse energy of 0.3 mJ. Bottom, left: Relative abundance of neon charge states normalized to the ion yield at a pulse length of 15 fs. The high charge states increase significantly with increasing pulse length. Ne^{4+} and lower charge states are almost unaffected as they stem from regions of the focus where the intensity is low. Bottom, right: Average charge state of neon as a function of the pulse length.

Chapter 3

Clusters in intense short wavelength pulses

The ionization of clusters in intense short-wavelength pulses and the processes following the ionization are an active field of research. Cluster are commonly used as model systems to study basic light–matter interaction. Many experimental studies have been performed at the FLASH and SCSS free-electron-lasers in the EUV to soft x-ray regime and research at the LCLS x-ray laser just started in the recent years. Common methods to study clusters in intense short wavelength pulses are electron and ion spectroscopy [43, 64, 65, 66, 67], fluorescence spectroscopy [68] and elastic scattering [10, 53, 69, 70]. Also many theoretical studies have been performed on this subject [40, 41, 71, 72, 73, 74]. However many processes during and after the ionization are not yet well understood and are still under active investigation. This chapter gives an overview of the current state of research in the field of clusters in intense short-wavelength pulses.

3.1 Absorption processes

The first studies of clusters in intense light pulses were performed in the infra-red regime. At those wavelengths the ionization dynamics of clusters, as nanometer sized objects, in intense laser fields is very different from atoms [37, 38, 42, 75, 76]. The electrons are efficiently driven out of the cluster by the electric field of the laser. After an initial ionization in the cluster, the plasma can be efficiently heated with the light field. As a result, a large number of electrons can be removed from the cluster and high ion charge states can be produced. This causes a violent Coulomb explosion with kinetic energies up to MeV, enough to trigger even nuclear fusion [38]. In the XUV and x-ray regime, no collective absorption effects in clusters were observed [43, 44, 66]. The light field frequency is too high to couple efficiently into collective excitations. As a result,

the absorption can be understood in a photon picture where one photon after the other or many photons simultaneously are absorbed from single atoms in the cluster. The field character of the light does not play a significant role.

3.2 Electron trapping in Coulomb potential

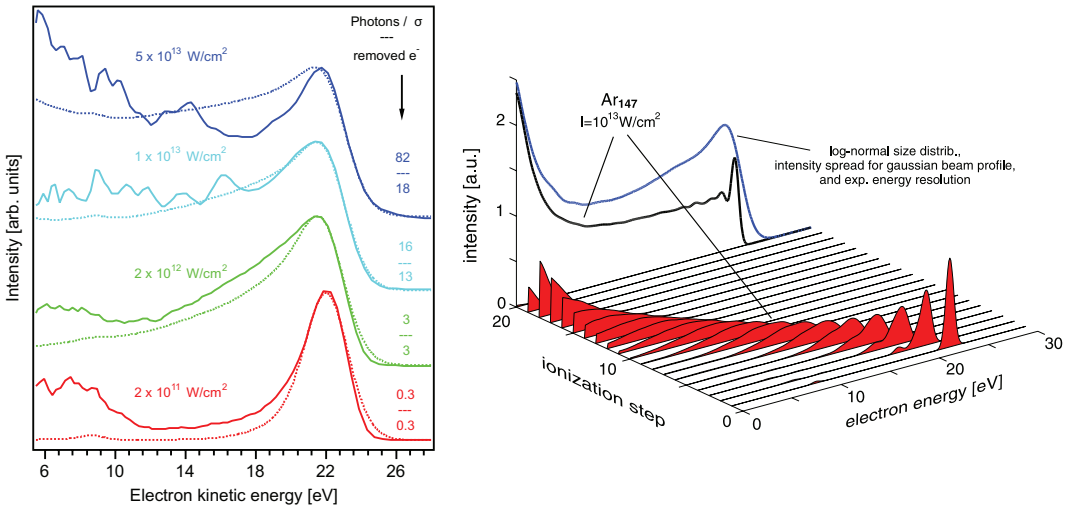

Figure 3.1: Electron trapping during the ionization of a cluster by an intense x-ray pulse [43]. Left: The solid lines show experimental photoelectron spectra of argon clusters at a photon energy of 37.8 eV for different intensities. The dotted lines are the corresponding simulations (c.f. right graph). Right: Red plots show a Monte Carlo simulation of the sequential ionization in the multistep model. As the Coulomb potential of the cluster increases with every ionization event the emitted electrons get slowed down and are finally trapped. The black curve shows the total photoelectron spectrum of all emitted electrons. The blue curve results from a model including cluster size distribution, light intensity profile and spectrometer resolution.

When a cluster is irradiated with a short-wavelength pulse, initially electrons are removed from the single atoms in the cluster. However, when multiple photons are absorbed by atoms of the cluster and more and more electrons leave the cluster, the influence of the neighboring atoms becomes important. The removal of electrons leaves positively charged ions back, and a Coulomb potential for the cluster as a whole starts building up. Electrons that leave the cluster are slowed down by this Coulomb potential and their final kinetic energy decreases with every ionization event. After a certain number of ionization events the Coulomb energy of the cluster is higher than the initial kinetic energy of the photoelectrons. From that point the electrons cannot leave the cluster anymore, they are trapped in the clusters Coulomb potential [43, 66]. The process, when electrons are excited and removed from their atomic core but remain trapped in the cluster, is referred to as *inner ionization*.

Electron trapping in the clusters Coulomb potential has been experimentally observed and validated by theoretical calculations. The experimental approach was to measure photoelectrons from clusters as a result of the ionization with intense XUV pulses. During the ionization process the kinetic energy distribution of the electrons changes under the influence of the increasingly positively charged cluster core. Fig. 3.1 (left, solid lines) shows experimental photoelectron spectra of argon clusters in an intense XUV pulse with a photon energy of 37.8 eV [43]. The top spectrum (blue solid line) is recorded at a power density of 5 x 10^{13} W/cm^2 where roughly 0.3 photons per atom in the cluster are absorbed. At a kinetic energy of about 20 eV there is a peak from photoelectrons that are emitted in the beginning of the pulse when the clusters are still neutral. The tail to lower kinetic energies can be explained with electrons that are emitted later in the pulse. They are slowed down by the already positively charged cluster core. The electron kinetic energy decreases with increasing charge of the cluster core during the ionization process. A Monte Carlo simulation in Fig. 3.1 (right) gives a more detailed insight in the stepwise ionization process. In this graph the kinetic energy distribution for all ionization steps is plotted (red). While the first electron keeps its full kinetic energy all the following electrons are slowed down by the cluster Coulomb potential. After about 20 ionization steps the excess kinetic energy drops below zero and all electrons that are excited afterwards cannot leave the cluster anymore. From this point on only inner ionization occurs. The resulting total electron spectrum including cluster size distribution and XUV beam profile is plotted as a blue line. In Fig. 3.1 (left) the simulation (dotted blue line) is compared to the experimental result (solid blue line) with good agreement.

For the conditions in the experiment shown in Fig. 3.1 the kinetic energy of the electrons leaving the cluster can be easily approximated. In argon clusters at a photon energy of 37.8 eV most of the ionization occurs in the 3p-level. At intensities of 5 x 10^{13} W/cm^2, on average, less than one electron per atom leaves the cluster. In a simple electrostatic model the kinetic energy $E_{k,j}$ of the j-th electron leaving the cluster is:

$$E_{k,j} = h\nu - I_p - \frac{e^2}{4\pi\epsilon_0} \sum_{i \neq j}^{all\ i} \frac{q_i}{r_{ij}} \tag{3.1}$$

where i runs over all other ions in the cluster with charge q_i and distance r_{ij}. I_p is the ionization potential of the atoms and $h\nu$ the photon energy. The total number of electrons M that can leave the cluster can be determined by calculating at which ionization step M+1 the kinetic Energy $E_{k,M+1}$ drops below zero.

For higher photon energies, photoionization from many shells and Auger electrons have to be taken into account. Further, if the x-ray pulse intensity is very high and significantly more than one electron per atom is removed, the ionization energies and Auger energies become dependent on the ionic state of the atom the particular electron belongs to. Eq. 3.1 changes to:

$$E_{k,j} = E_{\varphi}^{S} - \frac{e^2}{4\pi\epsilon_0} \sum_{i \neq j}^{all\ i} \frac{q_i}{r_{ij}} \tag{3.2}$$

Meaning the j-th electron is emitted from an atom in the electronic configuration S. If the j-th electron is excited by direct photoionization:

$$E_{\varphi}^{S} = h\nu - E_{b}^{S} \tag{3.3}$$

where E_b is the binding energy of the excited electron. If it is excited by an Auger decay:

$$E_{\varphi}^{S} = E_{a}^{S} \tag{3.4}$$

where E_a^S is the initial kinetic energy of the Auger electron. It depends on the course of the ionization process from which atom in what configuration S the j-th electron is emitted. To calculate the number of electrons that can escape from the cluster a theoretical model describing the course of the ionization process statistically has to be utilized to determine the initial kinetic energy of every electron.
In general it can be stated that the total number of electrons that can escape the cluster depends on the cluster size, the photon energy and the element the cluster consists of. In larger clusters less electrons per atom in the cluster can escape for a certain photon energy because of the long range Coulomb potential. The dependence on the photon energy and cluster composition is not as simple. It depends on which electronic shell is preferably ionized and how inner-shell holes decay. In intense XUV or soft x-ray pulses usually only a small fraction of the excited electrons can leave the cluster.
All the electrons that cannot leave the cluster remain trapped in the cluster Coulomb potential. They are not bound to a specific atom anymore but to the whole cluster core. These electrons are delocalized over the cluster and they can freely move inside the cluster but cannot leave it. In the literature they are called *quasi-free* electrons.

3.3 Formation of a nanoplasma

The quasi-free electrons in the cluster have a significant amount of kinetic energy that depends on the initial kinetic energy E_φ from the ionization process. Together with the ions in the cluster core they form a nanometer-sized confined plasma also referred to as *nanoplasma*. The plasma electrons can cause further inner ionization through collisions with bound electrons. They can as well exchange energy with each other on a femtosecond time-scale through collisions also referred to as *energy exchange collisions* [64, 77]. This leads to a thermalization of the electrons and their kinetic energy can be described by a thermal energy distribution which defines the electron temperature of the plasma. The temperature depends on the initial kinetic energy E_φ of the excited electrons. In a combined experimental and theoretical study the thermal energy distribution of the electrons was measured through electron emission [64]. In the nanoplasma, some electrons in

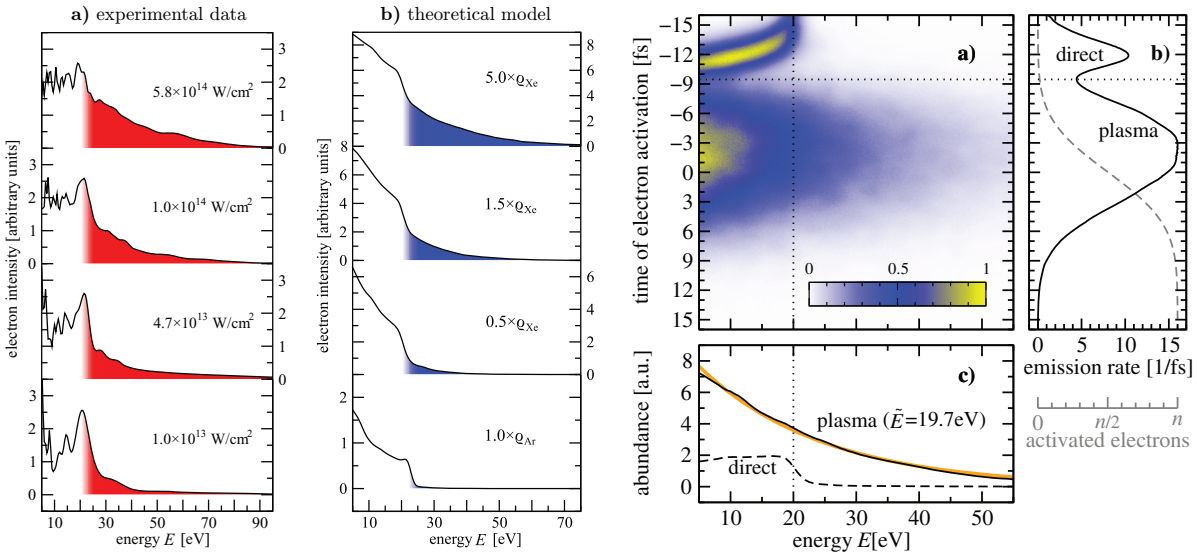

Figure 3.2: Emission of thermal electrons from an excited cluster nanoplasma [64]. The left panel shows experimental photoelectron spectra from xenon clusters at different intensities and the middle panel the respective simulated spectra. Graph a) in the right panel shows the result of simulations on the time-resolved electron emission from the clusters. At the beginning (T < -9 fs) direct photoelectrons are emitted until the emission gets frustrated. The trapped electrons thermalize and form a nanoplasma. Through energy exchange collisions additional energy can be transferred to some of the electrons so they have enough kinetic energy to leave the cluster (T > -9 fs).

the plasma can gain enough energy through energy exchange collisions to overcome the cluster Coulomb potential. These electrons that are emitted after the direct photoionization is frustrated can be measured through photoelectron spectroscopy.

In the experiment xenon clusters were excited with an intense soft x-ray pulse at a photon energy of 90 eV and peak intensities of 4 x 10^{14} W/cm^2. Fig. 3.2 shows the measured photoelectron spectra (left panel) for different intensities compared to simulated spectra (middle panel). Electrons emitted from the plasma can be seen as a tail (red and blue shaded) at kinetic energies above the main photo-emission line at 19.7 eV. The simulations agree well with the measurements. For a more detailed understanding time-dependent simulations have been performed. The right panel in Fig. 3.2 shows the resulting time resolved photoelectron spectrum. Early in the pulse (-15 fs to -9 fs) direct photoelectrons are emitted until they are trapped by the cluster Coulomb potential. Afterwards only inner ionization happens resulting in trapped, quasi-free electrons. They thermalize through energy exchange collisions and electrons that have enough kinetic energy are emitted resulting in a tail at kinetic energy above 19.7 eV. The projection of the 2-dimensional graph in the right panel of Fig. 3.2 on the energy axis results in the total kinetic energy spectrum shown in the middle panel of Fig. 3.2.

3.4 Interatomic barrier suppression in the ionized cluster

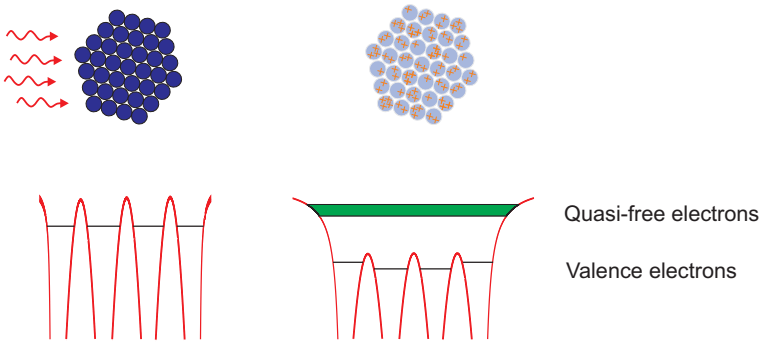

Figure 3.3: Simplified Coulomb potential of a cluster in the neutral state (left) and the nanoplasma state (right). The valence levels are indicated as black horizontal lines. In the neutral cluster the single atoms are separated by Coulomb barriers. When the cluster is ionized and turned into a nanoplasma by inner ionization the intra-atomic barriers are lowered. The quasi-free electrons in the nanoplasma are indicated as a green band.

The ionization process and the formation of a nanoplasma has a strong impact on the Coulomb potential inside the cluster. Fig. 3.3 shows a schematic of the cluster Coulomb potential before (left) and after (right) the ionization. The Coulomb potential of a neutral rare gas cluster is basically a superposition of the atomic potentials of the atoms in the clusters (c.f. Fig. 3.3, left). The bound electrons of each atom are well separated by the Coulomb barriers between them. After ionization, the Coulomb potentials of the single atoms in the cluster become deeper because the remaining electrons are less screened from the core. When the electron emission from the cluster is frustrated the excited electrons get trapped as quasi-free electrons. As a result, the interionic Coulomb barriers are pulled down by the surrounding charges (c.f. Fig. 3.3, right) [78]. The change in the Coulomb barriers has multiple implications. First, the energy that is necessary to excite an electron that is bound to an atom into the intra-cluster continuum, can be lower than the ionization potential in the neutral cluster. Second, the remaining valence electrons that are still bound to the single ion potentials are influenced. They shift up in energy compared to an atomic case without barrier suppression and their tunnel probability to neighboring ions increases.

3.5 Relaxation of the nanoplasma

After the absorption of a short wavelength pulse the highly excited nanoplasma will start to expand due to the thermal energy of the plasma and Coulomb repulsion of the ions. Depending on the temperature and the density of the plasma this expansion can be something between,

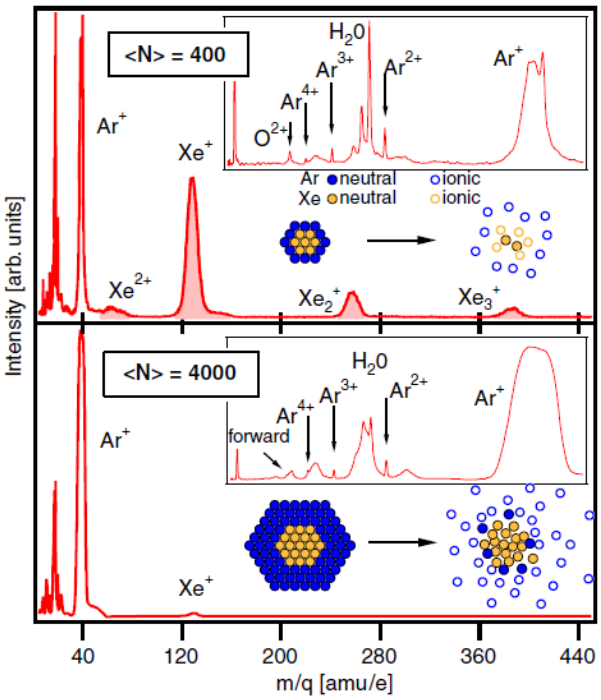

Figure 3.4: Charge transfer and recombination of clusters in intense soft x-ray pulses [79]. In a xenon core - argon shell system at 93 eV mostly the xenon is ionized. The charge results in a strong electric field pointing towards the center of the cluster pulling the trapped electrons there. In smaller clusters with a thinner argon shell (top panel) only a small part of the central xenon ions recombine and both argon and xenon remain ionized and are detected. In a larger cluster with a thicker argon shell (bottom panel), most of the xenon ions in the center recombine, the xenon core neutralizes again and virtually no xenon ions are detected.

or a mixture of, a thermally driven hydrodynamic expansion and a violent Coulomb explosion [8, 80, 81]. As the plasma expands it will cool down, enabling possible electron-ion recombination. Which of the expansion processes is dominant and if recombination occurs strongly depends on the size of the cluster, the degree of ionization, i.e., intensity of the light pulse, and the temperature of the nanoplasma, i.e., the wavelength of the light. A higher degree of ionization increases recombination. On the other hand the recombination rate decreases with increasing temperature of the nanoplasma. In the following, experimental results are presented for different combinations of these parameters.

For small clusters in the XUV and soft x-ray regime, it was observed that the quasi-free electrons in the cluster are pulled towards the ionic core and partially recombine with the ions [79, 81]. Experiments on pristine xenon clusters in intense 93 eV pulses from FLASH have investigated the kinetic energy release and abundance of the different ionic charge states from the clusters explosion [81]. The results indicate that the quasi-free electrons are pulled towards the center of the cluster by a strong electric field resulting from the cluster Coulomb potential. Atoms in

the outer shells of the cluster remain highly ionized and explode off driven by a strong Coulomb repulsion while the quasi-neutral core of the cluster expands hydrodynamically driven by thermal forces.

In another investigation xenon-argon core-shell systems were irradiated with intense 93 eV pulses from FLASH. The resulting tof spectra are shown in Fig. 3.4. At this photon energy the photoabsorption cross section of xenon is about a factor 25 higher than for argon. That is, in a mixed xenon-argon cluster mostly the xenon absorbs while the argon is almost transparent [82]. By changing the expansion parameters of the gas jet the ratio of xenon to argon atoms could be changed. In a first measurement, clusters with a size of $\langle N \rangle = 400$ atoms were irradiated. In this case the xenon core and the argon shell consist of a similar amount of atoms. The resulting ion tof spectrum is shown in the upper panel of Fig. 3.4. When these small clusters are irradiated a relatively high number of electrons per atom can escape the cluster Coulomb potential. The resulting charge is distributed over the whole cluster. The quasi-free electrons are pulled towards the center of the cluster resulting in a small quasi-neutral cluster core. Here, they can recombine with xenon ions in the cluster core. As the total number of charges per atom is high, there is still ionized xenon as well as ionized argon that appears in the measured tof spectrum.

In a second measurement the cluster size was changed to $\langle N \rangle = 4000$ atoms. Now the argon shell contains much more atoms than the small xenon core. The lower panel of Fig. 3.4 shows the resulting ion tof spectrum. Due to the larger cluster size, less electrons per atom can escape compared to the smaller clusters and the number of charges per atoms is lower. Quasi-free electrons, that are pulled into the center of the cluster, recombine with most of the xenon ions and neutralize them. The neutral xenon is not detected and it does not appear in the resulting ion tof spectrum, while the ionized argon from the shell ist still apparent. For higher photon energies there is some controversy. In a recent study small xenon clusters have been investigated at a photon energy of 850 eV at the LCLS [44]. The abundance and kinetic energy of the ionic fragments from the clusters has been determined. Supported by a rate equation models and plasma modeling the results have been interpreted as a hydrodynamic expansion of the nanoplasma with significant electron-ion recombination. However, for larger clusters at a photon energy of 800 eV very little to no recombination has been observed [10]. Fig. 3.5 (top panel) single shot ion tof spectra of large single xenon clusters with a diameter of 30 nm are displayed. Scattering images have been recorded in coincidence to determine the size of the cluster and intensity that it is exposed to, i.e., the position of the cluster in the focus profile. From clusters at the highest x-ray intensity only high charge states are observed (a) while for lower intensities (b and c) only intermediate or low charge states can be observed. These results have been interpreted as a absence of recombination in the hot nanoplasma that is produced in the clusters through absorbtion of many x-ray photons per atom. During the expansion the temperature of the plasma is high enough to suppress the recombination. The electrons and ions stay sperate until the ions reach the detector.

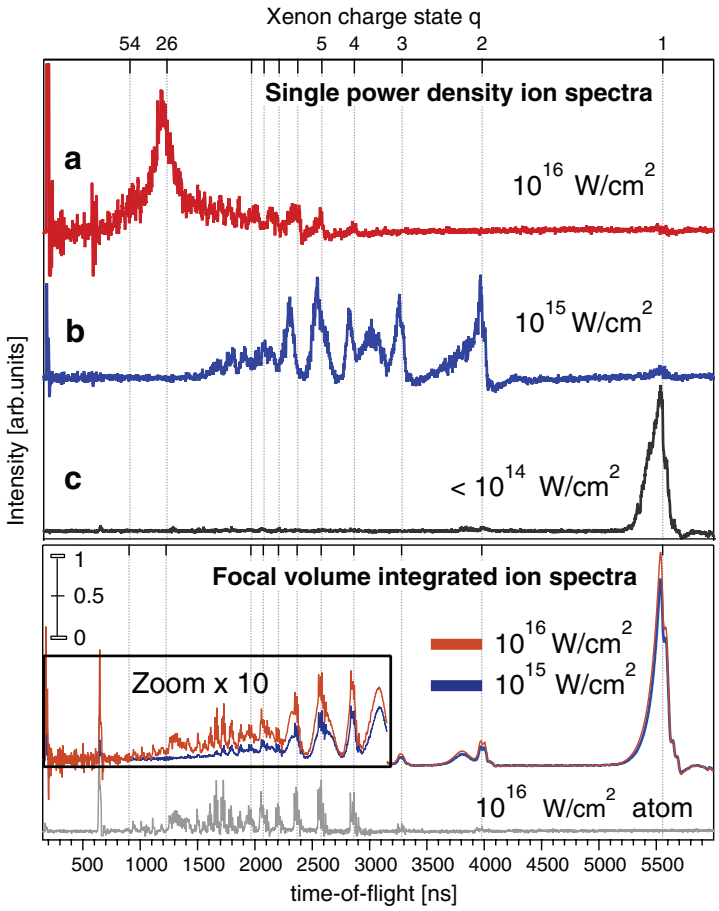

Figure 3.5: Top panel: single shot tof spectra of single clusters for different positions of the cluster in the focus profile [10]. The intensity at the cluster position and the cluster size has been determined from a coincidentally recorded scattering image. Lower panel: Single cluster tof spectra averaged over many shots for different x-ray pulse intensities.

Chapter 4

Experimental setup at the LCLS-AMO endstation

The experiments for this work were conducted in the HFP vacuum chamber of the endstation for Atomic Molecular and Optical (AMO) sciences of the Linac Coherent Light Source (LCLS) free-electron laser (FEL) at the SLAC National Accelerator Laboratory in Menlo Park, California, USA [1, 83]. Intense x-ray pulses produced with the help of a 1 km long section of the linear accelerator can be delivered to six experimental hutches in two experimental halls.
The near experimental hall (NEH) located downstream of the undulator contains the AMO, the soft x-ray material science (SXR) and the hard x-ray pump-probe (XPP) endstations. Further downstream of the NEH a cavern called far experimental hall (FEH) contains the x-ray coherent scattering (XCS), the coherent x-ray imaging (CXI) and the materials under extreme conditions (MEC) endstations. In the following chapter the x-ray beamline to the AMO endstation and the experimental setup will be described.

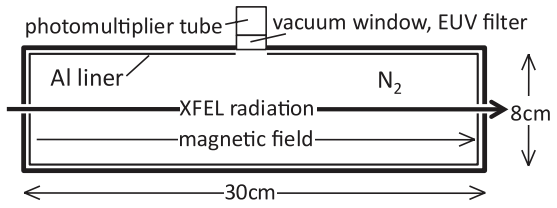

Figure 4.1: Schematic of the gas energy monitor at LCLS. The unfocused x-rays beam travels through a 30 cm long vacuum tube filled with nitrogen gas at a pressure in the mbar range. The nitrogen gets excited and ionized by the x-rays, and photoelectrons are emitted. Some of the excited electronic states in the nitrogen decay by emitting fluorescence photons that are detected by photomultipliers. A magnetic field is applied parallel to the x-ray beam to force photoelectrons on spiral trajectories and excite the gas more efficiently.

4.1 Front end enclosure - FEE

Between the undulator and the NEH the x-ray beam crosses the Front End Enclosure (FEE) [84]. The FEE contains a set of x-ray optics, diagnostics, and beam attenuators. There are two attenuator stages to reduce the x-ray intensity according to experimental needs, a gas absorber and several solid absorbers. The gas absorber is a two meter long vacuum pipe that can be filled with up to 20 mbar of nitrogen gas. A set of solid foils of different material can be quickly moved in and out of the beam in addition to the gas attenuator.

Because the SASE process is of statistical nature the intensity of the x-ray pulses fluctuates strongly with every shot (c.f. section 2.1). Therefore, two x-ray pulse energy monitors are installed in the FEE that measure the pulse energy of every single shot [85]. One is located in front of the attenuators to measure the full beam and one after the attenuators to measure the attenuated beam. Fig. 4.1 shows a scheme of LCLS pulse energy monitor. It is composed of a 30 cm long vacuum tube that has two small holes for the x-ray beam on both sides. The vacuum tube is filled with nitrogen gas at a pressure in the mbar range. When the unfocused x-ray beam crosses the energy monitor it excites and ionizes the nitrogen. Fast photoelectrons emitted from the nitrogen excite and ionize further nitrogen molecules through collisions. Excited states in the molecules will decay emitting fluorescence photons in the UV range that are detected by two redundant photomultipliers. To prolong the electron trajectories a magnetic field parallel to the x-ray beam is applied that causes the photoelectrons to gyrate around the x-ray beam axis and increase the probability of collisions. This magnetic field is produced by a solenoid around the vacuum tube. Because the x-ray beam is unfocused and the gas density is low the x-rays induce only linear processes in the nitrogen. Thus, the fluorescence signal registered by the photomultipliers is proportional to the pulse energy of the x-ray pulse that goes through the energy monitor. However, the signal strongly depends on photon energy, x-ray beam size and alignment. Hence, the energy monitors have to be calibrated to an absolute measure of the pulse energy and recalibrated every time major x-ray parameters are changed. For calibration, a so called *energy loss scan* of the electron beam going through the undulator is performed as explained in the following.

The total kinetic energy of the electron bunch is measured before and after the undulator. This difference in energy is called energy loss. By inducing a slight spatial oscillation, called *orbit oscillation*, in the electron bunch the lasing process can be partially or fully disturbed. Even though the lasing process is disturbed the electrons still lose energy in the undulator due to spontaneous emission of light. On average, the difference in energy loss between a lasing and a non-lasing electron beam equals the average pulse energy of the coherent x-ray pulse. For that reason, the energy loss can be used to calibrate the energy monitor. To obtain a calibration curve the orbit oscillation is slowly ramped up to get a range of x-ray intensities. Every point of this energy loss scan is averaged over many shots to even out the statistical fluctuations of the x-ray pulses.

For the experiments in this work, it was a major experimental challenge to keep the average x-ray pulse energy, i.e., the number of photons per pulse, constant for different pulse lengths. This was achieved by setting the gas attenuator to a pressure such that the downstream energy monitor was showing the same average reading for the different pulse lengths. This resulted in a very stable average pulse energy in the experiment for different pulse length, independent of linearity and dynamic range of the energy monitor. Downstream of the x-ray diagnostics and attenuators in the FEE a set of optics is installed to deflect the beam to the different endstations in the NEH and to the FEH. The mirrors are single crystal silicon substrates coated with boron carbide that reflect the x-rays in gracing incidence. To reach the AMO endstation the x-ray beam is reflected off three mirrors.

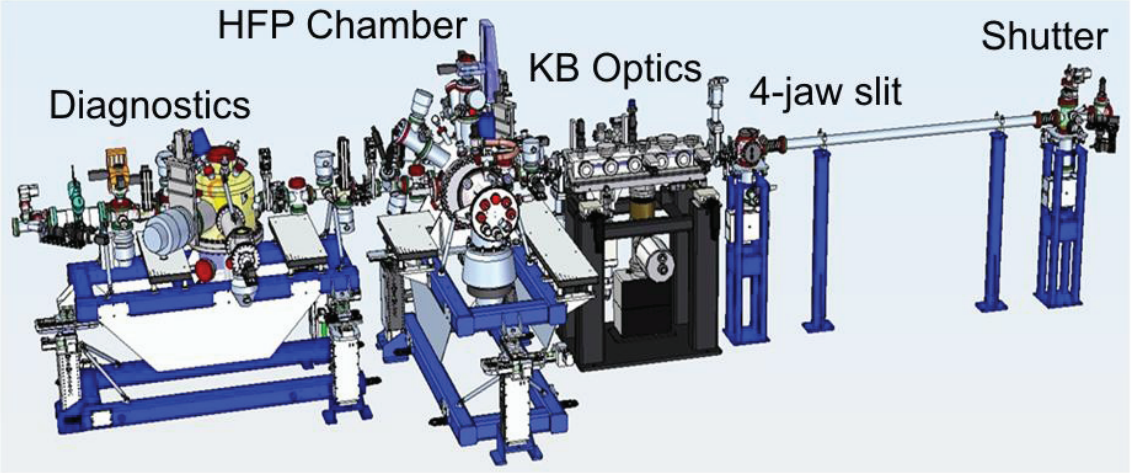

Figure 4.2: Schematic of the AMO endstation at the LCLS. From right to left (upstream to downstream of the FEL): Fast shutter assembly to pick single pulses. 4-jaw slit to cut beam down in front of the optics in order to reduce stray light. Set of variable focal length KB optics to focus the x-ray beam into the experimental chamber. High Field Physics (HFP) chamber with cluster jet, ion and electron spectrometers. Diagnostics chamber for beam diagnostics and as alternative experimental chamber.

Photon energy	$480\,eV - 2000\,eV$
Focus diameter	$\approx 1.2\,\mu m$
Pulse energy	$< 4\,mJ$
Power density	$< 10^{18}\,W/cm^2$
Pulse length	$5 - 500\,fs$

Table 4.1: Available x-ray beam parameters at the AMO endstation

4.2 The endstation for atomic, molecular and optical (AMO) sciences at LCLS

The endstation for Atomic Molecular and Optical (AMO) [83] sciences is the first endstation downstream of the undulator. It was the first endstation that received light from the LCLS in August 2009. In Tab. 4.2 the x-ray beam parameters that are available in the AMO endstation are listed. Fig. 4.2 shows a schematic of the AMO beamline and endstation, where the x-ray beam is coming from the right side. On the upstream end a fast shutter is installed to pick single pulses for experiments that need only a single x-ray shot at a time. A 4-jaw slit can be used to aperture down the unfocused beam and control what part of the focusing optics is illuminated. The x-ray beam is focused with a pair of variable focal length Kirkpatrick-Baez (KB) optics into the experimental vacuum chambers. Fig. 4.2 shows the standard configuration of the AMO beamline with the High Field Physics (HFP) vacuum chamber in the optimal x-ray focus and the Diagnostic (DIA) vacuum chamber downstream of the HFP. Depending on the experimental needs both chambers have been reconfigured and the diagnostic has been temporally replaced by the CAMP (CFEL ASG Multi Purpose) vacuum chamber in the past [86]. In the following, the elements of the AMO endstation that are most important for this work are described in more detail.

4.3 Kirkpatrick-Baez x-ray optics

When the soft x-ray beam reaches the AMO endstation it has a size of about 1.5 mm to 2.5 mm fwhm depending on the photon energy. In order to reach high intensities the x-ray beam has to be focused. The light delivered to the AMO endstation has wavelengths that are too short for multilayer optics but not short enough for crystal diffraction or x-ray lenses. Therefore, the most versatile way of focusing the x-ray beam is using gracing incidence mirrors.
In the AMO endstation a pair of Kirkpatrick-Baez (KB) [87] optics is utilized to focus the x-ray beam. Fig. 4.3 shows a schematic of KB optics. The x-ray beam is reflected in gracing incidence and focused in each dimension by one elliptic mirror. The curvatures of the two mirrors have to

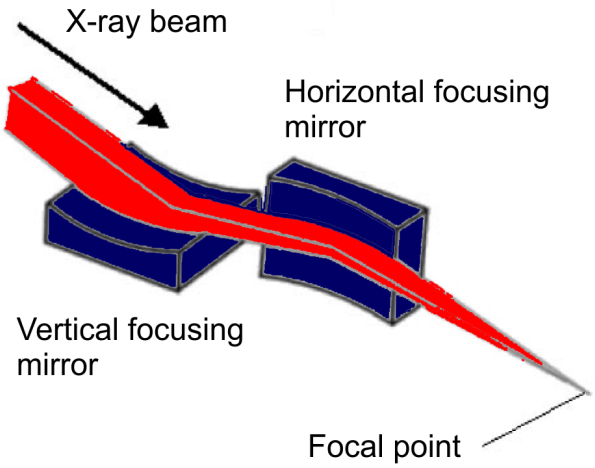

Figure 4.3: Schematic of Kirkpatrick-Baez (KB) optics. The x-ray beam is reflected in gracing incidence off two curved mirrors. The upstream mirror is focussing in vertical direction and the downstream mirror in horizontal direction. In the AMO endstation both mirrors can be dynamically bent to change the focal length. Best focussing is achieved in a distance of 1.1 m from the center of the downstream mirror where the interaction region of the HFP chamber is located.

be different as they have a different distance to the focus, i.e., the upstream mirror has a longer focal length than the downstream mirror. Both mirrors are consist of 40 cm long single crystal silicon substrates that are coated with boron carbide (B_4C). The substrate can be dynamically bent to move the focal spot along the beam axis or defocus the x-ray beam when needed. The diffraction limit for the diameter of the x-ray focus is about 1 μm at a distance of 1.1 m from the center of the downstream mirror. Realistically, focal spot size measurements indicate that the focus diameter is about 1.2 - 1.8 μm fwhm [88].

4.4 High-field physics (HFP) vacuum chamber

All experiments shown in this work where conducted in the HFP vacuum chamber of the AMO endstation. The interaction region of this chamber is located 1.1 m downstream of the second KB focusing mirror in the spot of the smallest possible focus. At this point power densities of up to 10^{18} W/cm^2 can be reached. In its original configuration this chamber was built for atomic and molecular ion spectroscopy and precision electron spectroscopy. The chamber is doubly mu-metal shielded and a low density pulsed gas with a single skimmer stage is mounted in direction perpendicular to the x-ray beam.
For the present work the setup has been reconfigured to accommodate the needs of a cluster experiment. In Fig. 4.4 a schematic of the modified HFP vacuum chamber is shown. The x-ray beam (green arrow) is crossing the chamber perpendicular to the cluster jet (yellow arrows)

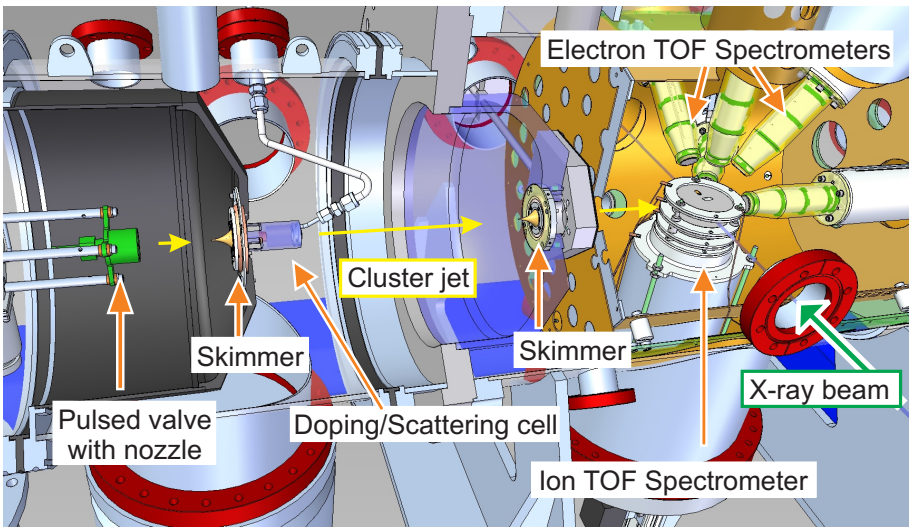

Figure 4.4: Experimental setup inside the HFP vacuum chamber. Clusters are produced by supersonic expansion through a pulsed solenoid valve with a conical nozzle of 100 μm throat diameter and 15 ° half angle. The main chamber with the tof-spectrometer is separated from the nozzle by two differentially pumped skimmer stages. A gas cell next to the first skimmer could be used to scatter out atomic background and produce heterogeneous clusters.

as indicated. In the interaction region the x-ray focus is overlapped with the gas target and surrounded by the entrance apertures of electron and ion spectrometers. Five high resolution electron tof spectrometers similar to the design published by Hemmers *et al.* [89] are pointing to the interaction region from the upper hemisphere in different angles to investigate dipole and non-dipole effects.

The ion spectrometer that is important for the current investigation is inserted from the bottom of the chamber. Fig. 4.7 shows a detailed top view of the interaction region where the x-ray beam intersects the cluster jet above the entrance aperture of the ion spectrometer. The slit aperture for this spectrometer has been designed and tested in order to screen atomic background from the detector. A more detailed description of the ion tof spectrometer is given in section 4.6.

On the left side on Fig. 4.4 the newly designed cluster jet setup is shown. Clusters are produced by supersonic expansion through a pulsed solenoid valve with a conical nozzle. They pass two differentially pumped skimmers before they get to the interaction region as indicated with yellow arrows. The cluster jet setup is described in more detail in following section. The HFP vacuum chamber is pumped by a 1000 l/s turbomolecular pump to reach a low base pressure and to be able to handle the gas load from the gas jet.

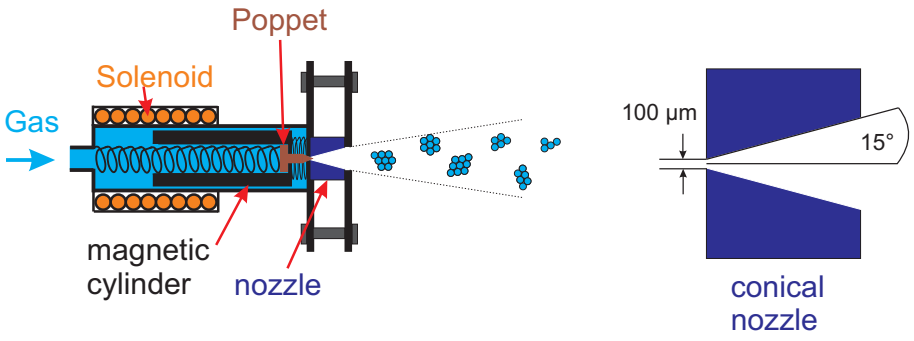

Figure 4.5: Schematic of the pulsed Parker Series 99 solenoid valve with a conical nozzle. The nozzle cylinder is clamped to the front plate of the valve and sealed with an indium gasket foil. In the closed state the magnetic cylinder holding the poppet is pushed towards the nozzle to seal the opening. When a current is flowing through the solenoid the magnetic cylinder together with the poppet is pulled back and gas can flow through the nozzle.

4.5 Cluster jet

For the experiments in the present work a defined cluster jet with sufficient density and low atomic background was necessary. Therefore, a special gas jet setup was designed. The overall setup is shown in Fig. 4.4 with the pulsed valve, two differentially pumped skimmers and a doping and scattering cell. In section 2.3 of this work, the principle of the cluster production through supersonic expansion is explained. The clusters are produced by a supersonic expansion of argon gas through a nozzle. A pulsed valve (Hanfin-Parker Series 99 General Valve) running at the beam frequency of 120 Hz was used to reduce the gas load in the nozzle chamber and the background pressure in the main chamber. Fig. 4.5 shows a schematic this valve with the nozzle. When current flows through the solenoid the magnetic cylinder holding the sealing poppet is pulled back and gas can flow through the nozzle. After the opening cycle the current is turned off and the magnetic cylinder is pushed back into the closed position by a spring. For the cluster experiments a conical nozzle with a throat diameter of 100 μm and a opening half angle of 15° was used. This particular nozzle was used for many cluster studies before [43, 79, 81] and is therefore very well characterized. The whole valve is mounted on a three-axis motorized in-vacuum stage to be able to align the nozzle with respect to the skimmers and the interaction region.
Downstream of the nozzle, the clusters travel through two trumpet shaped skimmers to the interaction region (c.f. Fig. 4.4) The skimmer next to the nozzle has a hole diameter of 1 mm the skimmer next to the interaction region a hole diameter of 0.5 mm. Both skimmers reduce the background pressure stepwise and transmit only the central part of the cluster jet. This results in a cluster beam diameter of 0.6-0.7 mm in the interaction region. The skimmers can be separately aligned to form a straight line that intersects with the interaction region. To be able to service the gas jet it is separated with a gate valve from the vacuum of the main

experimental chamber. Turbomolecular pumps were installed in the two vacuum volumes to ensure high pumping speed. The chamber containing the nozzle was pumped with a pumping speed of 2600 l/s and the chamber between the two skimmers with 1000 l/s.

4.6 Time-of-flight spectrometer

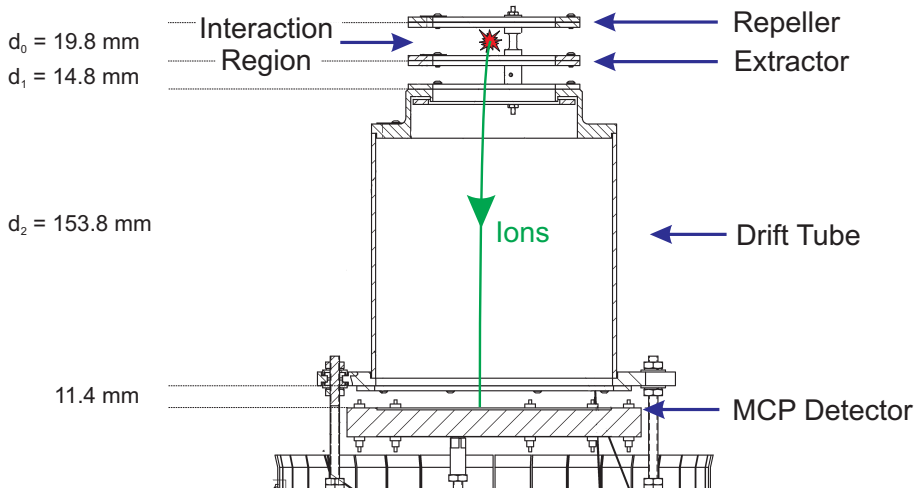

Figure 4.6: Drawing of the ion time-of-flight (tof) spectrometer. The interaction region is located between the repeller and the extractor plate. The drift tube is terminated by highly transmissive meshes on both ends. Both plate electrodes and the drift tube can be set to independent potentials. At the lower end of the drift tube the MCP detector is located.

The data for the present work were recorded with an ion time-of-flight (tof) spectrometer. Fig. 4.6 shows a drawing of the spectrometer. It consists of two electrode plates, a flight tube and a multi channel plate (MCP) detector. Repeller and the extractor plates are solid Molybdenum plates, with the extractor having a rectangular 1 mm x 2 mm slit aperture in the center (c.f. Fig. 4.7). The drift tube is a solid metal tube that is terminated with a copper mesh on both sides to avoid the electric field reaching into the drift region. All electrodes and the drift tube can be set to independent potentials. The ions are detected by a 120 mm diameter chevron-stack double MCP that is located at the end of the drift tube with an anode behind it. Tab. 4.2 shows the operating potentials of the spectrometer relative to ground.
Ions produced by the x-rays in the interaction region are accelerated downwards by the electric field between the electrodes. After the ions reach the upper mesh of the drift tube they drift with a constant velocity. Behind the lower mesh of the drift tube, the ions are accelerated over a short distance to the detector. Eq. 4.2 shows the relation between the tof and the mass-to-charge ratio (m/q) for the ion spectrometer with the distance d_0 and U_0 the voltage between repeller and extractor, d_1 and U_1 between extractor and drift tube and d_2 the length of the drift tube

Repeller	ground
Extractor	-500 V
Drift Tube	-1445 V
MCP front	-2000 V
MCP back	ground
Anode	+100 V

Table 4.2: Operating voltages for the ion tof spectrometer

[90].

$$k_0 = 2\,(U_0/2 + U_1)/U_0 \tag{4.1}$$

$$TOF = 1.02\sqrt{\frac{m}{2q}}\left(2\sqrt{k_0}d_0/2 + \frac{2\sqrt{k_0}}{\sqrt{k_0}+1}d_1 + d_2\right) \tag{4.2}$$

For constant lengths d_0,d_1,d_2 and voltages U_0,U_1 the time-of-flight TOF of an ion is proportional to its mass-to-charge ratio:

$$TOF \propto \sqrt{\frac{m}{q}} \tag{4.3}$$

Ions with an initial kinetic energy will have a shorter tof if they have a velocity component towards the detector and a longer tof if they have a component away from the detector.
Fig. 4.7 shows top view of the extractor plate with the slit aperture. The interaction region is located above the slit aperture where the cluster jet and x-ray beam cross. This slit has the long axis perpendicular to the x-ray beam and reduces the acceptance of the spectrometer along the x-ray beam to a small region where the x-ray focus is located. The width of the slit is 1 mm which is similar to the Rayleigh length of the x-ray focus where the fluence is nearly constant. In addition, the slit reduces the signal from atomic background along the x-ray beam and the acceptance for ions with initial kinetic energy. Fig. 4.8 a) shows trajectories of ions with kinetic energy in the spectrometer that start in different directions. Only ions flying in a small angle towards or away from the detector cross the slit. Ions with a significant velocity component perpendicular to the spectrometer axis will hit the solid part of the extractor plate and do not reach the detector. The transmission of ions with an isotropic velocity distribution depends strongly on their initial kinetic energy. While ions with no or very low kinetic energy compared to the acceleration field are fully transmitted only a small fraction of ions with higher kinetic energy make it to the detector. Ionic fragments from clusters irradiated with intense x-ray pulses usually have a significant kinetic energy and therefore their transmission is low compared to the uncondensed atomic background from the expansion.

To increase ion signal from the clusters compared to ion signal from atomic background a

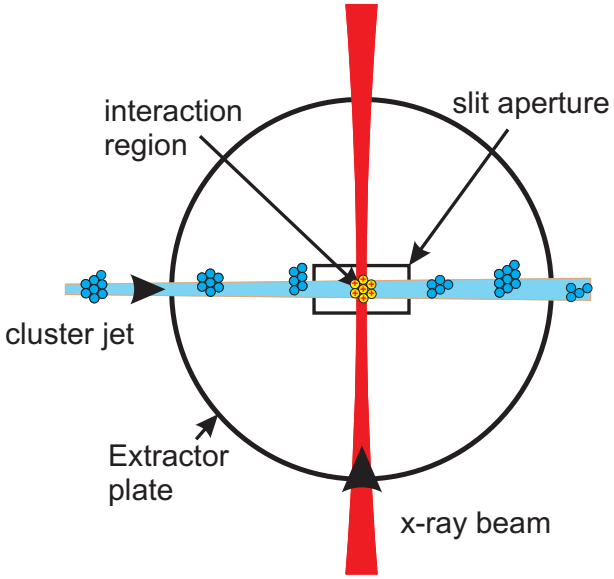

Figure 4.7: Schematic of the x-ray beam intersecting the cluster jet above the extractor plate with the slit aperture in a top view. The x-ray focus is located above the slit where it intersects the cluster jet coming from the left.

smaller slit design compared to earlier configurations has been implemented together with the capability of moving the HFP chamber far enough along the cluster jet to reach the edge of the slit. Fig. 4.8 shows the principle of the slit design. In Fig. 4.8 a) a setup with a large slit is shown with the resulting ion spectrum. Dominantly ions without kinetic energy and some ions with kinetic energy flying in a small angle towards and away from the detector cross the slit. Ions without kinetic energy form the sharp peak in the center and the broader peaks to the left and right of it can be assigned to ions with kinetic energy flying towards and away from the detector. Fig. 4.8 b) shows a setup with a slit of exactly half the size compared to Fig. 4.8 a). The velocity distribution of ions from a cluster explosion is isotropic and the according spectrum exhibits the same features with half the intensity because half the ions compared to Fig. 4.8 a) hit the metal plate and are not detected. In Fig. 4.8 c) the slit is slightly smaller so that ions without kinetic energy just hit the edge of the plate. Because the interaction volume is very small in the direction perpendicular to the beam this is a very small movement compared to the slit size and the signal from ions with kinetic energy (from clusters) remains almost unchanged while the signal from ions without kinetic energy (from atomic background) is greatly suppressed. In order to move the slit with respect to the interaction region the whole vacuum chamber with the spectrometer and the gas jet was moved perpendicularly to the x-ray beam in direction of the cluster jet.

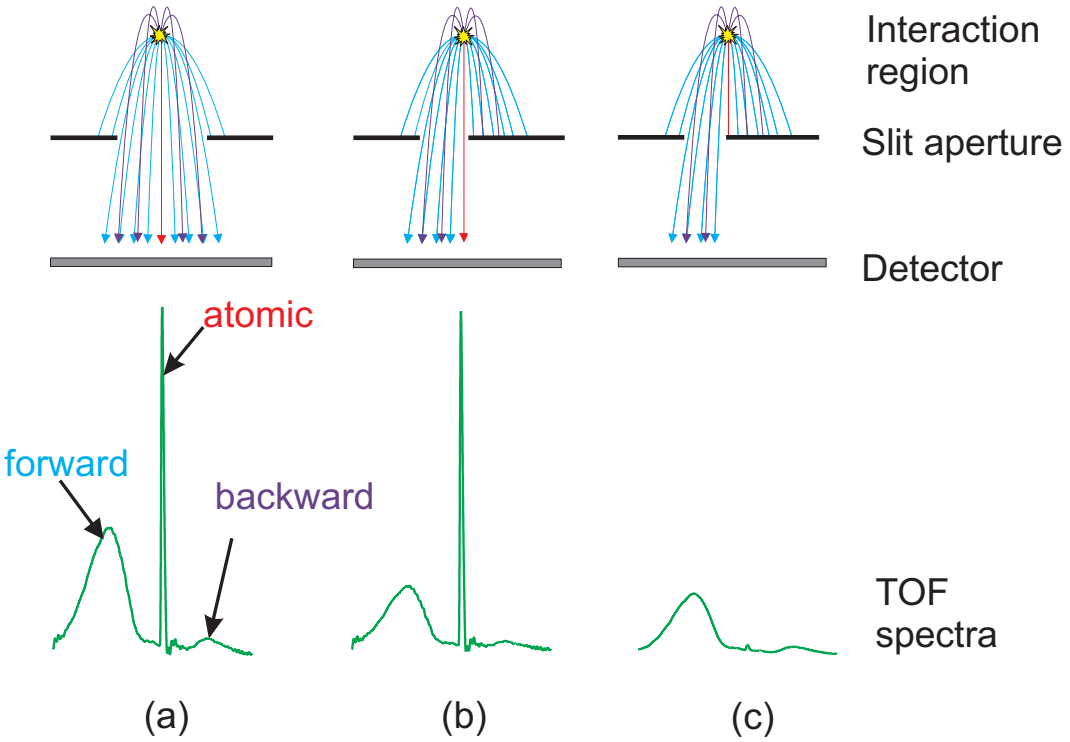

Figure 4.8: Schematic of the atomic background reduction using a specially designed slit aperture of the tof spectrometer. Top: Interaction region (yellow) with ions starting towards (blue) and away (purple) from the detector. Bottom: Ar^{2+} portion of the resulting tof spectrum with the sharp peak from background atoms in the center. Two broad peaks toe the left and right stem from ions with kinetic energy starting towards and away from the detector from a cluster explosion.
(a) Interaction region is located above the center of the slit. Only ions starting in an narrow angle towards or away from the detector or atomic background make it through the slit and are detected. The atomic background is comparably strong because all of it is transmitted.
(b) Slit aperture is slightly about half the size of (a). The intensity of the cluster signal is cut to about half the signal of (a) because only the ions starting to the left are transmitted while ions starting to the right hit the metal of the slit plate. However, qualitatively the cluster signal is similar because the ions are emitted isotropically from the cluster explosion. The atomic signal has the same intensity as in (a) because still all of it is transmitted.
(c) Slit aperture is slightly smaller than in (b) in a way that the atomic signal is just cut off. The cluster signal is almost unchanged because the total width of the slit is about the same. The signal from the atomic background, however, is greatly reduced.
It is noted that for the explanation of the background reduction principle the slit width is changed in this figure. In the actual experiment the slit has a fixed width. To switch between the background reduction mode and a mode where atoms can be measured the whole vacuum chamber including the slit was moved with respect to the x-ray beam. The cluster spectra were measured in a position similar to (c) while for atomic spectra the slit was centered on the x-ray beam (similar to a).

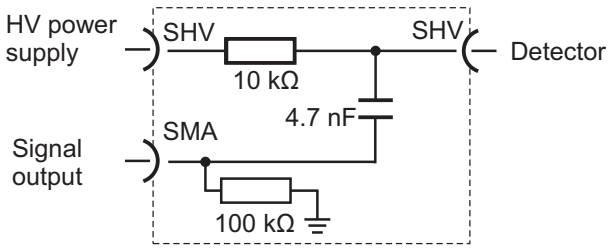

Figure 4.9: Outcoupling electronics for the MCP detector of the ion time-of-flight spectrometer. The signal is decoupled from the detector that is at a potential given by the HV power supply. While the capacitor separates the signal output from the DC voltage from the supply the high-frequency pulses from the detector can travel through it to the output. The capacity together with the impedance of the detector is matched to transmit the ns tu μs pulses from the detector. The $10\,k\Omega$ resistor separates avoids reflections from the HV supply and the $100\,k\Omega$ resistor pulls the output to ground if nothing is connected to it.

The ions are detected with a chevron stack multi channel plate (MCP) detector. The tof ion signal is decoupled from the anode which is a $+100\,\mathrm{V}$ potential. A custom made RC-circuit was used to decouple the high-frequency signal from the potential of the anode. Fig. 4.9 shows a schematic of the RC circuit. The high voltage of the detector is separated with a capacitor from the signal cable. High frequency signals from the detector can travel through the capacitor to the signal output and further to the digital transient recorder. The capacitor is optimized to the length of the pulses from the ion tof spectrometer of a few nanoseconds to a few microseconds. To avoid signal reflections from the high voltage power supply it is separated by a $10\,k\Omega$ resistor from the detector. The signal output is pulled to ground with a $100\,k\Omega$ resistor to keep it from charging up when nothing is connected to it. The tof traces are recorded on a shot-by-shot bases with Aqiris digital transient recorders and fed into the LCLS data acquisition system. All important experimental as well as beam and machine parameters are saved with every single shot together with a tof trace. This allows sorting the data according to the properties of the respective x-ray pulse (e.g. pulse energy) in the off-line analysis.

4.7 SIMION simulation of the ion tof spectrometer

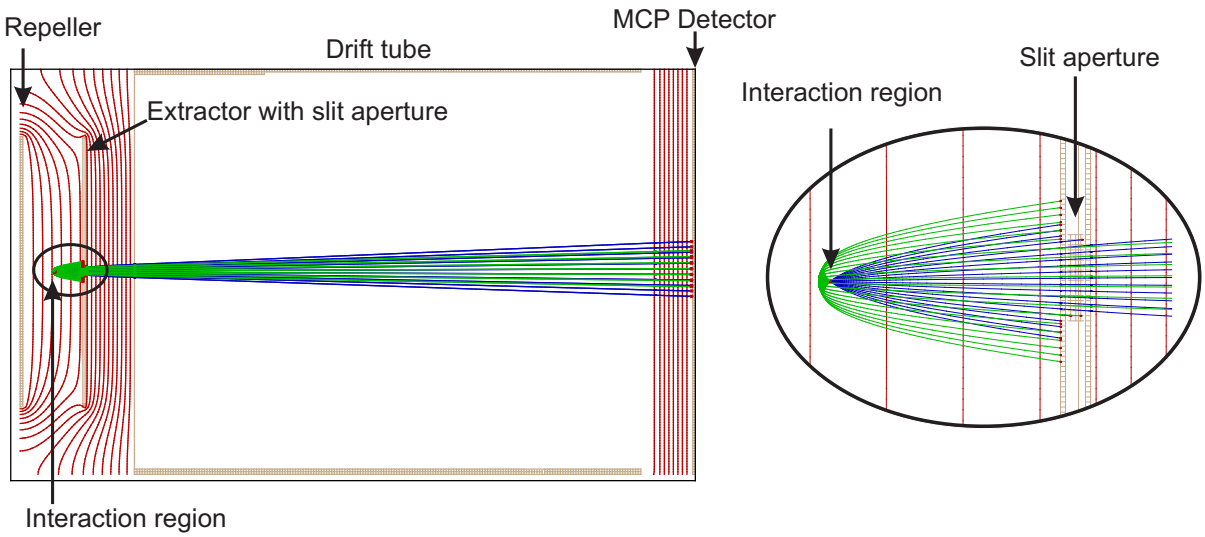

Figure 4.10: Left: Schematic of the tof spectrometer in the SIMION simulation. The interaction region is located between the repeller and extractor plate. Equipotential curves are drawn as red lines. The green and blue lines are ion trajectories of Ar^{2+} ions starting in the interaction region. All ions have a kinetic energy of 120 eV and their initial velocity vector is pointing in an angle of $\pm 25°$ towards (blue) or away (green) from detector. Right: Magnification of the interaction region and the slit aperture. Ions starting with an angle of larger than 10 ° to the detector axis and towards the detector don't make it through the slit and hit the extractor plate. For better display the interaction region is located at the center of the slit in this simulation.

To estimate the expected ion flight times in the spectrometer and the spectrometer transmission for this experiment and to be able to estimate the kinetic energy of the measured ions, a simulation of the ion trajectories in the electric fields of the tof spectrometer was performed using SIMION. SIMION is a simulation software package that calculates electrostatic fields from a given set of electrodes and ion trajectories in this field using numerical integration techniques [91]. The geometry of the tof spectrometer was imported to SIMION from the original CAD model. In Fig. 4.10 a cut through the spectrometer is shown with the electric field lines (red) and ion trajectories (blue and green). In the beginning the exact position of the interaction region in the direction along the spectrometer symmetry axis (horizontal direction in Fig. 4.10) is unknown for the experiment. It was determined by varying the position in the simulation until the tof of argon ions without kinetic energy fit the experimental tof shown in Fig. 6.3. In Fig. 4.11 the simulated tofs of argon ions with charges from 1+ to 16+ are compared to the measured tofs and the red line in Fig. 4.11 represents an inverse square root function fitted to the tof values. The inset of Fig. 4.11 shows the relative error of the tof for every charge state. It can be seen that the simulated values agree with the experimental results to an accuracy of below 1%. The ion trajectories shown in Fig. 4.10 belong to Ar^{2+} ions with a kinetic energy of

120 eV. Their initial velocity vector points in an angle of $\pm 25°$ to the spectrometer axis towards (blue) or away (green) from the detector. In the magnification of the interaction region on the right side of Fig. 4.10 it can be observed that fewer of the backwards flying ions cross the slit to the detector. This is due to the wider transversal spread once they reach the extractor plate because of the longer flight time. According to the simulations the transmission for backwards going ions should be about 50% lower than for forward going ions. However, in the experiment much fewer of the backward going ions are transmitted, only about 10% (c.f. Fig. 4.8). The lower transmission can be explained by slight misalignment of the spectrometer and inhomogeneities in the electric field between extractor and repeller and has been observed in other experiments with similar spectrometer geometries [81, 92].

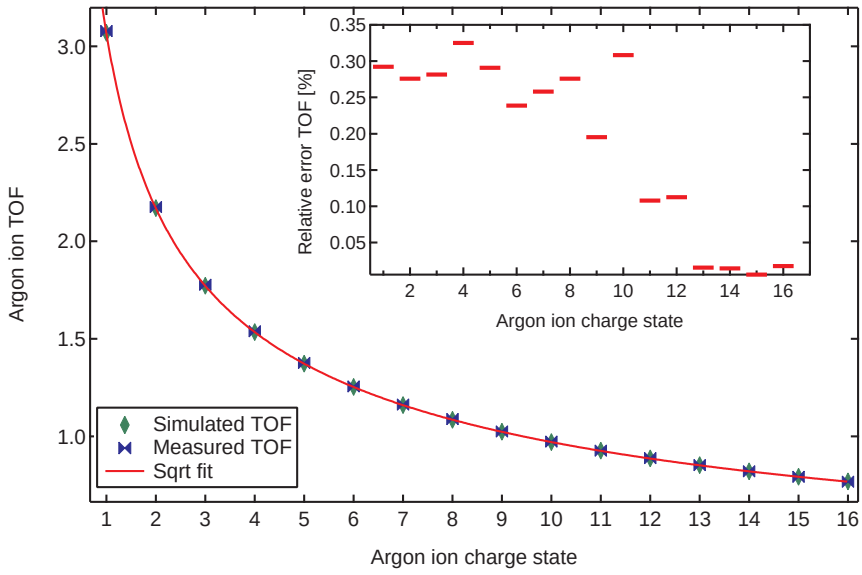

Figure 4.11: Comparison of simulated tof (green markers) to the experimentally measured tof (blue markers, see Fig. 6.3.) of the charge states of atomic argon. The values agree within less than 1% deviation and fit favorably to an inverse square root function.

Chapter 5

Simulation of the ionization dynamics

At the time this experiment was conducted, LCLS was the first and only light source producing intense x-ray pulses with photon energies above the C_{1S} edge. Meaning there is only little experimental data available in this regime and the ionization dynamics of even simple atomic systems in intense x-ray pulses is not yet completely understood. A first study performed by Young *et al.* delivered insight into the ionization of neon with intense x-ray pulses and showed that a rate equation model with a perturbative approach can describe the experimental data well [7]. To quantitatively describe the pulse length dependence of ionization with intense x-ray pulses a theoretical model was needed. For argon, however, multiple ionization via unknown intermediate excited states becomes important adding uncertainty to the simulations [93]. Specifically, the unexpected high charge states above Ar^{10+} observed in the atomic spectra (c.f. Fig. 6.3) indicate that these processes play an important role under the current experimental conditions. Therefore neon is chosen for this simulation because all relevant rates and states are known.

5.1 Rate equation model

Similar to earlier studies [7, 94] a rate equation model was set up for the x-ray ionization of neon. The ionization cross sections σ for the 64 different electronic states of neon were calculated using the Los Alamos Atomic Physics Code [59]. Auger and Fluorescence rates Γ were taken from the literature [95, 96]. The probability for a shake-off electron from the ionization of the neutral atom is also included [97]. Not included in these simulations are shake-off processes in ions and double Augers decays. The temporal x-ray pulse profile $J(t)$ was modeled as a statistical ensemble of 2 fs fwhm spikes distributed over the nominal pulse length and normalized with total pulse energy.

The ionization rate from a certain state S to an ionized state S' is $\sigma_{S\to S'}J(t)$. The population of the state that is ionized $P_S(t)$ decreases by $\sigma_{S\to S'}J(t)$ and the population of the ionized

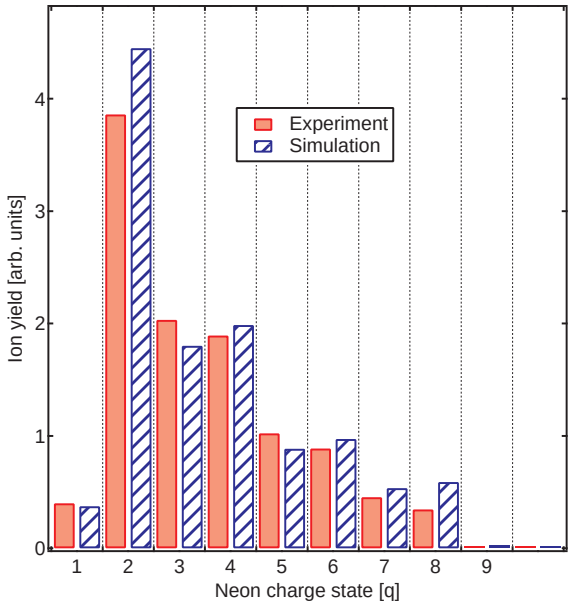

Figure 5.1: Simulated neon ion yields compared to ion yield measured in the HFP chamber at 1200 eV photon energy. The simulations agree well with the experimental data. Differences a most likely due to the fact that double Auger decays and shake-off processes are not included in the simulations and due to the temporal and special structure of the x-ray beam.

state $P'_S(t)$ increases by $\sigma_{S'\to S}J(t)$. In the same way the population of states increase or decrease through Auger decay and fluorescence decay independent of the current x-ray intensity by $\Gamma_{S\to S'}P_S(t)$ and $\Gamma_{S'\to S}P_{S'}(t)$ respectively. In more detail, $\Gamma_{S\to S'}P_S(t)$ is the probability that the state S with the population $P_S(t)$ decays to another state S' in a certain time interval. All cross sections and transition rates were included in a set of coupled rate equations where the temporal change $\frac{d}{dt}P_S(t)$ of the population of every electronic state S of neon is described by:

$$\frac{d}{dt}P_S(t) = \sum_{S'\neq S}^{all\ config} (R_{S'\to S}P_{S'}(t) - R_{S\to S'}P_S(t)) \tag{5.1}$$

with $R_{S\to S'}$ are being the combined transition rate of ionization and inner-shell vacancy decay:

$$R_{S\to S'} = \Gamma_{S\to S'} + \sigma_{S\to S'}J(t) \tag{5.2}$$

In the beginning, before the x-ray pulse starts only the neutral ground state $S = 0$ is populated:

$$P_0(t\to -\infty) = 1 \tag{5.3}$$

all other states are not populated:

$$P_{S\neq 0}(t\to -\infty) = 0 \tag{5.4}$$

The Auger decay rate for the ground state is 0:

$$\Gamma_{0\to S'} = 0 \tag{5.5}$$

And the neutral ground state cannot be produced through ionization:

$$\sigma_{S'\to 0} = 0 \tag{5.6}$$

The coupled rate equations in Eq. 5.1 are solved by numerical integration for small time steps of 1/200 fs to calculate the asymptotic neon charge state distribution. For every set of x-ray pulse parameters 10000 simulations were made and averaged to decrease statistical fluctuations that are caused by the random pulse profile.

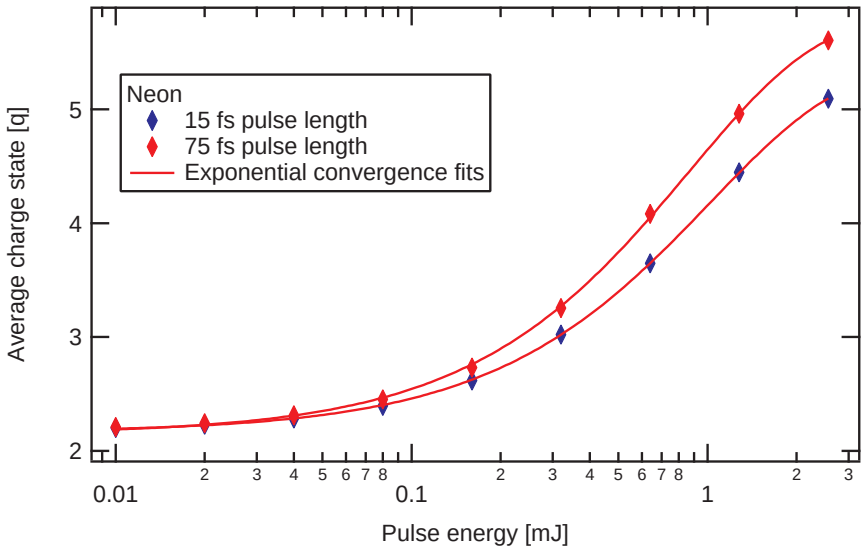

Figure 5.2: Simulated average charge state of neon atoms vs. pulse energy of the x-ray beam for a pulse length of 15 fs and 75 fs. The average charge state grows with the pulse energy until it starts to saturate. The saturation levels are different for the shorter and the longer pulse.

5.2 Simulated ion yields

To verify the validity of the rate equation model, a set of neon tof spectra was recorded with the HFP ion tof spectrometer [83] at a photon energy of 1.2 keV and a x-ray pulse length of 50 fs and compared to the results of the simulations. For the simulations a gaussian spatial x-ray focus profile with a diameter of 1.6 μm fwhm was assumed. Fig. 5.1 shows the measured and simulated charge state distribution with an average pulse energy of 0.4 mJ. There is a very good agreement between the experimental data and the theoretical distribution. The lower amount of Ne^{2+} in the experimental data compared to the simulation can be explained with double Auger

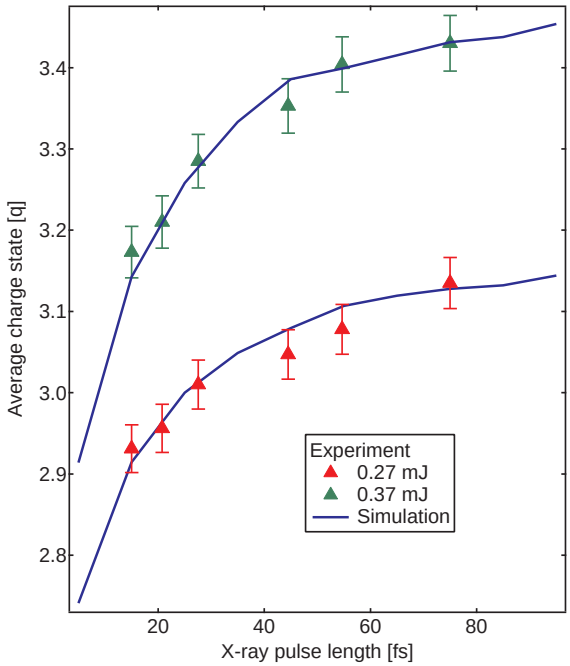

Figure 5.3: Average charge state of neon as a function of the pulse length for different pulse energies. The red and green triangles represent experimental data at different pulse energies and the blue lines represent the simulated results.

decays, one photon double ionization or shake-off/shake-up processes. These are not included in the simulations and are leading from neutral neon to Ne^{3+} and higher charge states with the absorption of only one photon.

Pulse length and pulse energy are the two important x-ray pulse parameters for the investigation presented in this work and their dependence has to be included in the simulations. Fig. 5.2 shows the pulse energy dependance of the simulated average charge states vs. pulse energy for an x-ray pulse with a pulse length of 15 fs and a 75 fs. For a constant x-ray pulse length of 15 fs the average charge state increases with the pulse energy as more and more electrons are removed from the atoms. Around 1 mJ the average charge state starts to converge to a constant value. This is because the atoms that see the highest fluence in the center of the focus are ionized to the highest charge state that can be reached via sequential photoabsorption with 1.2 keV.

If the average charge state of a short 15 fs pulse is compared to a longer 75 fs pulse differences in the pulse length dependent ionization become apparent. As mentioned in section 2.7 a longer x-ray pulse with the same number of photons can ionize more efficiently than a shorter one because the probability that inner-shell holes are refilled via Auger or fluorescence decay is higher in during longer pulse. This difference can be observed in Fig. 5.2 in terms of a higher average charge for the 75 fs pulse compared to the 15 fs pulse for the same pulse energy. For pulse energies below 0.02 mJ both pulses yield a similar average charge state as in average close

to one photon per atom is absorbed and the pulse length doesn't play a role in the absorbtion process.

Fig. 5.3 shows experimental data for neon recorded with different x-ray pulse length and pulse energies compared to the simulations. In this graph the average charge state is plotted vs. the x-ray pulse length for different pulse energies. The red and green triangles represent the experimental data for x-ray pulse length between 15 fs and 75 fs and pulse energies of $0.27\,\mu J$ and $0.37\,\mu J$ respectively. The blue lines show the simulated spectra for the same parameters. Overall, there is a good agreement between the simulated and the experimental data indication that the current rate euqation model describes the atomic ionization processes well.

5.3 Auger rates during the ionization process

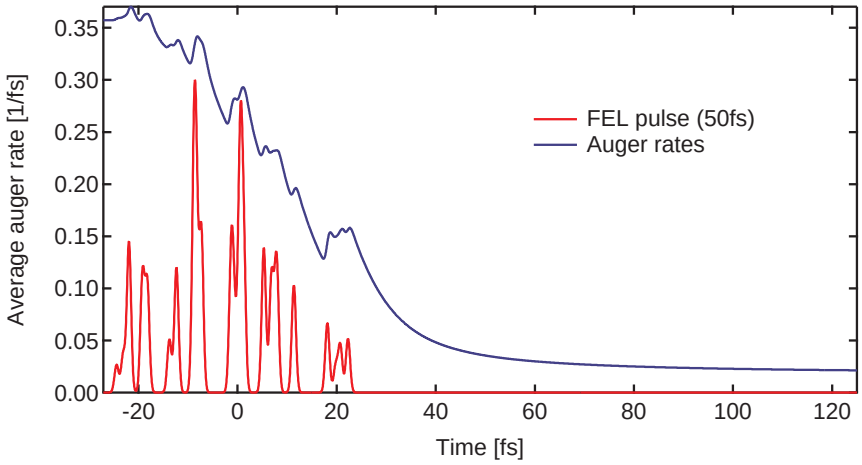

Figure 5.4: The red curve shows the temporal profile of a statistical x-ray pulse. The blue curve shows the average Auger rate of an ensemble of neon atoms in the focus of the x-ray beam. Overall the Auger rates drop over time as more and more valence electrons are ejected from the atoms. Only for a very short time after an x-ray spike when core electrons are removed there is a transient increase of the Auger rates until the holes are filled via Auger decay and the rates drop again.

The data in Fig. 5.2 and Fig. 5.3 show that there is a significant increase for the average charge state of neon from an x-ray pulse length from 15 fs to 75 fs. Young *et al.* [7] reported a change in the ion distribution of neon going from x-ray pulse length of 80 fs to 200 fs. The question may arise why the difference in pulse length affects the ionization process at all if both pulses are much longer than the Auger lifetime of a single neon 1s hole of 2.8 fs [95].

To answer this question the intermediate ionic states during the ionization process have to be considered. A single neon 1s hole is only the first step in the ionization process of neon in an intense x-ray pulse. When this hole decays and more photons are absorbed the valence shell

will be emptied resulting in longer Auger lifetimes up to many hundred femtoseconds for highly ionized ions [95]. Fig. 5.4 shows an illustration of this decrease in the Auger rates over the duration of the x-ray pulse. It shows the result of a simulation of the ionization of neon atoms in the central part of the x-ray focus where the intensity is high. A single random x-ray pulse (red line) and the ionic states of neon produced by this pulse where extracted from the simulation in 1/25 fs steps. From the state distribution the average Auger rate of all states that can possibly Auger decay weighted by their abundance was calculated for every time step (blue line). It is noted that the average Auger rate in the blue curve in Fig. 5.4 is not normalized to the ratio of states than can Auger decay to states that cannot. That is, in the beginning of the x-ray pulse and long after the x-ray pulse the average Auger rate is only represented by very few atoms of the whole ensemble.

At the start of the pulse (t=-25 fs) only few atoms are singly ionized and the average the Auger rate is 0.357/fs which corresponds to a lifetime of 2.8 fs of a single neon 1s hole. Whenever there is an intense x-ray spike more core holes and even double 1s core holes are produces and the rate transiently increases. However, over the duration of the whole x-ray pulse when the valence shell of neon becomes emptier through Auger decays, the average Auger rate strongly decreases. This results in an average Auger rate of about 0.026/fs some time after the pulse which corresponds to a lifetime of 38 fs. During the x-ray pulse the average Auger lifetime is in between 2.8 fs and 38 fs. This shows that the intermediate ionic states that are produced during the ionization process have much longer Auger lifetimes than the single core hole and they are produces in significant amounts. As a result the ionization dynamics of neon in intense x-ray pulses are sensitive to differences in pulse lengths on the order of tens of femtoseconds.

Chapter 6

Experimental results and Discussion

The goal of the present work is to investigate the time and size dependent ionization dynamics of nanometer sized samples in intense x-ray pulses. In general, there are two important experimental parameters for the study of these phenomena. First, the sample size to investigate the size dependence of the ionization. Second, the pulse length to measure the time dependence of the ionization for every sample size. As a sample system atomic clusters are ideal for the present investigation because their size can be easily tuned and they can be produced in sufficient density for measurements in the gas-phase. In gas-phase studies any influence from a surrounding medium or sample support can be excluded. Therefore, argon nanoclusters were chosen as a sample system. Argon is a monoatomic gas and argon clusters can reliably be produced. Further, argon has been also used in the model calculations by Saalmann *et al.* [7].
To study the time dependance of the ionization the pulse length of the LCLS was tuned using the slotted spoiler technique (c.f. section 2.2). The x-ray photon energy for this study was set to 480 eV, well above the binding energy of the argon L-shell. 480 eV was the lowest photon energy available at the LCLS at the time this study was performed. At this photon energy the argon L-shell exhibits the highest ionization cross section compared to the M-shell.
As preliminary steps the x-ray focus in the AMO endstation was optimized and the slit aperture to suppress atomic background (c.f. section 4.6) was aligned. Then argon ion tof spectra for atomic argon were recorded as a reference and to gain an understanding of the atomic absorption process. Afterwards, ion tof spectra for different sample sizes, i.e., cluster sizes were measured. To investigate ionization dynamics the x-ray pulse length was varied for all argon measurements. In the following chapter the results of these three experimental steps are presented, discussed and compared to simulations.

6.1 Atomic neon reference data

The ionization dynamics studied in this work are relying on highest possible x-ray intensity. This is because many photons per atom have to be absorbed in order to efficiently induce transparency in atoms and clusters. For that reason the size of the focal spot is a critical parameter for the success of the experiment. However the shape, size and position of the focus depends sensitively the bending of the KB optics and their positioning relative to the x-ray beam on a micrometer scale. Therefore, the first step in the experimental study was to optimize these parameters in order to minimize the size of the x-ray focus in the interaction region and to reach highest possible x-ray pulse intensities. From experience in earlier studies the charge state distribution of neon gas ionized at photon energy of 2000 eV gives a reliable feedback [7] on the intensity in the focus. It has also the largest set of experimental and theoretical reference data [7, 8, 18, 44, 98, 99]. For these reasons neon ionization at a photon energy of 2 keV has become the de-facto standard for the focus optimization at the LCLS AMO endstation. The optics were tuned by pitching and tilting the KB mirror set relative to the x-ray beam and bending the two mirrors. Fig. 6.1 shows the neon spectrum at 2000 eV and an average pulse energy of 2.4 mJ for the optimized focus. It compares very well to the spectrum in Fig. 2.16 [7] (blue line) at the same photon energy and pulse energy indicating a diameter of the focal spot of about 1.6 μm.

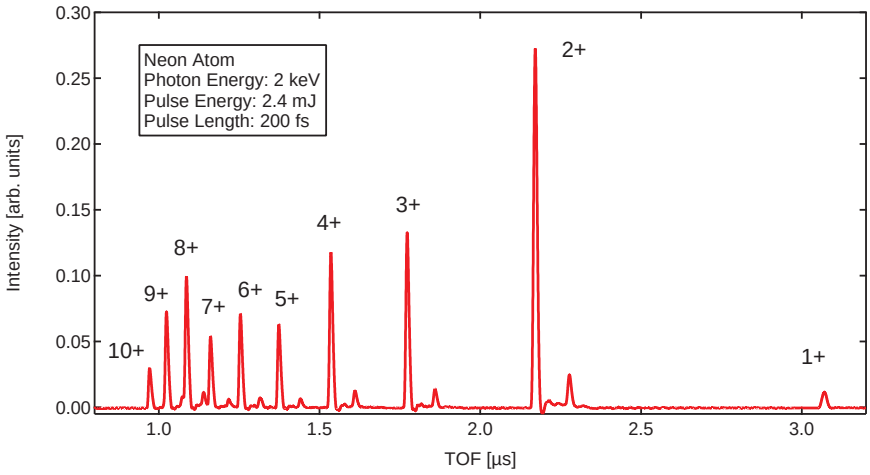

Figure 6.1: Neon ion time-of-flight spectrum after optimization at a photon energy of 2 kV and a pulse energy of 2.4 mJ. Comparison to Fig. 2.16 shows that the focal conditions where similar to the ones reported by Young *et al.* [7].

6.2 Suppression of atomic background

The second important step in the alignment of the experiment was the positioning of the slit aperture in the extractor plate of the tof spectrometer relative to the interaction region to suppress the atomic background (c.f. Fig. 4.8). As explained before, in the current setup the extractor plate with the slit is fixed to the ion spectrometer and the x-ray beam cannot be moved without sacrificing the focus. For that reason, to align the slit aperture relative to the interaction region, the whole HFP vacuum chamber was moved in direction perpendicular to the x-ray beam axis to change the relative positioning of the slit and the interaction region. The cluster jet also moves with the vacuum chamber, but the overlap between cluster jet and x-ray beam is maintained moving in this direction (c.f. Fig. 4.7). Starting from the slit centered to the x-ray beam the chamber was moved sideways until the atomic background was reduced to a tolerable level. A comparison of the ion tof spectra from atomic argon with the interaction region above the center of the slit (red line) and at the position on the edge of the slit (black line) is shown in Fig. 6.2. These spectra were recorded at a photon energy of 480 eV and a cluster size of $\langle N \rangle = 150$. Sharp peaks in the red curve stem from ions of single uncondensed atoms in the jet and from the background that do not have kinetic energy. Signal from cluster ions with kinetic energy are the broader underlying peaks. When the interaction region is positioned at the edge of the slit (black line) the atomic signal is nearly absent except for small residues and the broad cluster signal is almost unchanged. This allows for measuring cluster tof spectra of unprecedented quality that have only minimal atomic background.

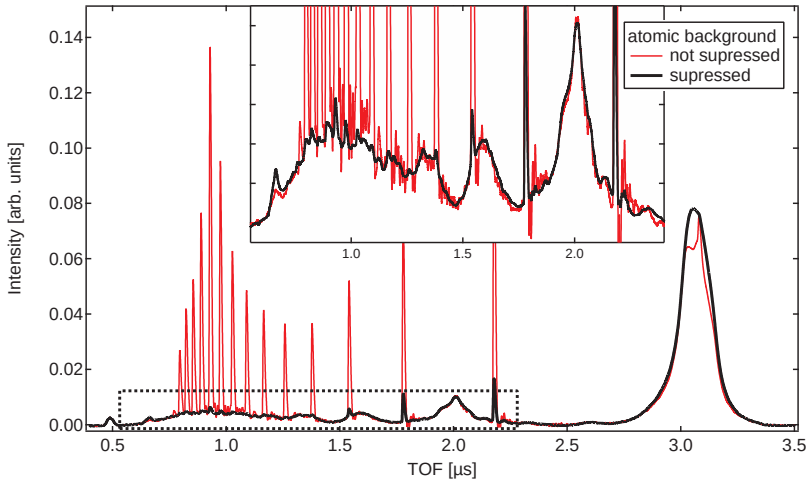

Figure 6.2: Two cluster tof spectra for the same cluster size $\langle N \rangle = 150$ and a photon energy of 480 eV. The red curve is recorded with the interaction region at the center of the tof slit aperture and the black curve at the edge of the tof slit aperture (c.f. Fig. 4.8). In the inset the area inside the dashed rectangle is magnified. In the black curve the atomic background (narrow peaks) is greatly suppressed while the cluster signal (broader peaks) is almost unchanged.

6.3 Atomic argon in intense x-ray pulses

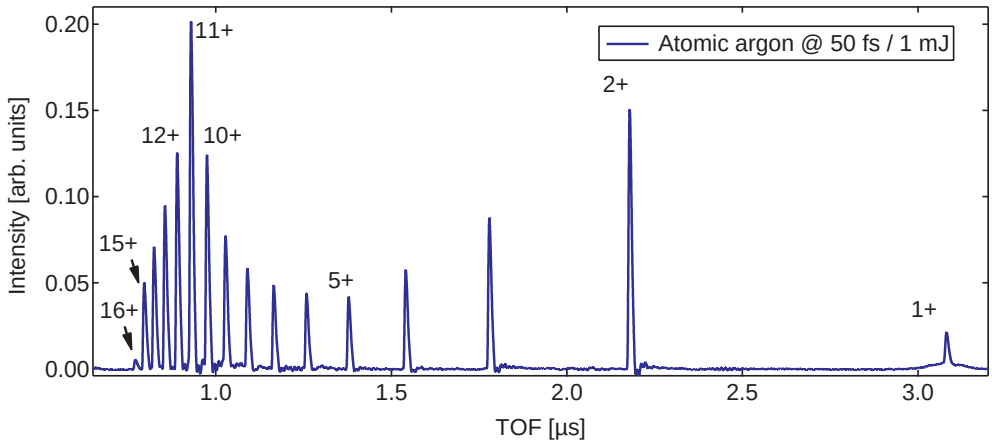

Figure 6.3: Tof spectrum of atomic argon with a pulse energy of 1 mJ and a pulse length of 50 fs. The most prominent peak is Ar^{11+}. The ionization potential of Ar^{9+} in its ground state is 479 eV while for Ar^{10+} it is already 540 eV. That is, the highest charge state that can be reached by ionization of ionic ground states with 480 eV photons is Ar^{11+}. In this spectrum a significant amount of higher charge states up to Ar^{16+} can be observed indicating that ionization via resonant excitation and intermediate excited states occurs.

Understanding the interaction between intense x-ray pulses and argon atoms is a prerequisite for the study on clusters. Currently, very few atomic and molecular systems have been investigated under the influence of intense x-ray pulses and there are no published experimental results on atomic argon or argon clusters. Therefore, as a first step, the ionization of atomic argon with intense x-ray pulses was investigated.

Fig. 2.12 in section 2.4 shows measured absorption cross sections of argon in the soft x-ray regime and Tab. 2.3 lists calculated differential absorption cross sections at 480 eV. The 2p shell exhibits with 1.05 Mbarn by far the highest absorption cross section, the cross section of the 2s shell is about a factor five lower while the 3s and 3p cross sections are about 20-40 times lower and therefore negligible for most purposes. Fig. 2.14 shows the probability of the inner-shell decays for L-shell holes in argon. When a 2p electron is removed from an argon atom the Auger decay dominates over the fluorescence decay. For a 2s hole a LLM Koster-Kronig decay is most likely with the result that a valence electron is removed and the atom remains with a 2p hole.

In the following the number of absorbed photons under the experimental conditions in this experiment is calculated in a crude estimate with the linear absorption cross section of argon (c.f. Tab. 2.3). The diameter of the x-ray focus was determined to be about 1.6 μm fwhm and the average pulse energy in the full x-ray beam at 480 eV is about 1 mJ. The transmission of the beamline between undulator and experiment is not precisely known but a value between 10 % and 50 % ist most likely according to earlier results [100, 101]. For this estimate a value of 20 % for the

beamline transmission is assumed. This results in a x-ray fluence in the focus of the experiment of about 13000 photons/Å^2. With the linear photoabsorption cross section of 1.35 Mbarn for argon at this photon energy about 175 photons/atom would be absorbed. Certainly this value is an overestimate because it assumes a linear cross section for a non-linear absorption process and on top of this argon just does not have enough electrons to absorb such a high number of x-ray photons. In reality, the absorption cross section will change with the first absorbed photon as the electronic levels shift and the number of electrons is changed. Also this calculation does not include the time dependent processes in the atom and temporal structure of the x-ray pulse which are important for the x-ray induced transparency. In addition the spatial profile of the x-ray focus is not flat so that atoms in different areas of the focus are exposed to different intensities. But nevertheless the estimated number of, in average, 175 absorbed photons per atom shows that with the current fluence and power density the absorption process is far beyond the linear regime and many photons are expected to be absorbed per atom. This argument still holds when the slotted spoiler is inserted to reduce the pulse length. Then the pulse energy is reduced by a factor 5-10.

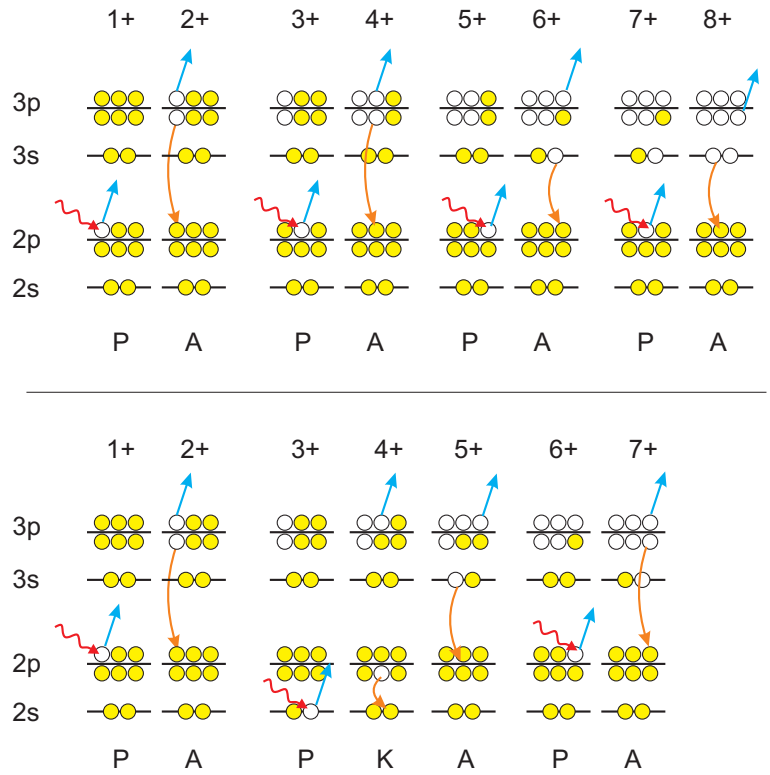

Figure 6.4: Examples of likely ionization pathways until the valence shell is empty for argon at a photon energy of 480 eV. Participating processes are Photoionization (P), Auger decay (A) and Koster-Kronig decay (K). In the upper row four 2p photoionization–Auger decay cycles lead to Ar^{8+} with an empty valence shell. In the lower row a 2s-electron is ionized. This leads to a Koster-Kronig decay followed by an Auger decay. As a result Ar^{7+} is produced with the absorption of three photons.

In Fig. 6.3 a measured tof spectrum of atomic argon at a pulse energy of 1 mJ and a photon energy of 480 eV is plotted. Charge states up to Ar^{16+} can be observed with the maximum intensity at Ar^{11+}. While Ar^{1+} is almost absent there is a local maximum at Ar^{2+} and Ar^{3+}. The 2p and 2s holes that are mostly created at this photon energy are subsequently refilled via Auger decay or Koster-Kronig decay. This results in the creation of about two or three charges per atom even for the absorption of a single photon. Ar^{1+} is only produced through valence ionization that is very unlikely at this photon energy (c.f. Tab. 2.3). Ar^{2+} and Ar^{3+} are most likely produced by absorption of a single photon in the L-shell while Ar^{4+} and Ar^{5+} are most likely produced by absorption of two photons. This indicates that the lowest observed charge states are produced in the outer parts of the x-ray focus where only one or few photons per atom are absorbed. For the production of the strongest peak Ar^{11+}, however, at least 6-8 photons have to be absorbed per atom. Fig. 6.4 shows examples of two likely ionization paths to Ar^{7+} or Ar^{8+}. In the upper row of Fig. 6.4 four 2p photoionization–Auger decay cycles lead to Ar^{8+} with an empty valence shell. In the lower row a 2s-electron is ionized and a Koster-Kronig decay followed by an Auger decay leads to the emission of two valence electrons. As a result Ar^{7+} is produced with the absorption of only three photons. This shows that after about three to four photoionization–Auger decay cycles the valence M-shell is empty. Further ionization occurs through photoionization of the L shell. In these cases seven photons would be needed to produce Ar^{11+}. If double Auger decays or shake-off processes less photons will be needed. On the other hand if valence ionization occurs even more photons are needed for Ar^{11+}. It is noted that in Fig. 6.4 the ionizations processes are shown in sequences of photoionization and Auger decays. If the x-ray intensity is high enough there could be two or more photoionizations until an Auger decay happens. This will change the order of the processes but not their number because every inner-shell hole will most likely Auger decay if valence levels are still occupied.

In the case of neon (c.f. section 2.6) the maximum observed charge state is the one with the lowest ground state ionization potential above the photon energy. This is different for the electronically more complicated systems argon. In Tab. 6.1 the ground state ionization potential of all argon charge states are listed. The spectrum in Fig. 6.3 shows that in argon charge states beyond the ground state ionization potential can be produced. Already the ground state ionization potential of Ar^{10+} with 539 eV is higher than the photon energy of 480 eV. Therefore, the high abundance of charge states above Ar^{10+} and up to Ar^{16+} is surprising. A simple explanation would be simultaneous two-photon absorption. However, this is very unlikely at the power densities currently delivered by LCLS (c.f. section 2.5) and has not been observed experimentally even at higher intensities and absorption cross sections [18]. The most likely explanation for the creation of these charge states are resonant excitation and ionization via intermediate excited states [93]. This will be discussed in more detail in the section 6.10 of this chapter. As these resonances and excited states are unknown it is impossible to model this charge state distribution with a simple rate equation model used for neon by Young et al. [7] and in chapter 5 of this work.

CS	IP [eV]	CS	IP [eV]
0+	15.8	9+	478.7
1+	27.6	10+	539.0
2+	40.7	11+	618.2
3+	59.8	12+	686.1
4+	75.0	13+	755.7
5+	91.0	14+	851.3
6+	124.3	15+	919.3
7+	143.5	16+	4121
8+	422.4	17+	4426

Table 6.1: Ground state ionization potential (IP) for the different charge states (CS) of atomic argon.

6.4 Pulse length dependent ionization of argon atoms

Prior to investigating clusters, the ionization dynamics of atomic argon has to be understood. For that purpose, atomic argon spectra are recorded as a function of the x-ray pulse length. The tof spectra of argon atoms for pulse lengths between 30 fs and 85 fs and the same pulse energy of 0.2 mJ are shown in Fig. 6.5. The x-ray pulse length was tuned with the slotted spoiler foil. Therefore, the total x-ray pulse energy is lower compared to the spectrum in Fig. 6.3 because the spoiled part of the electron beam does not emit coherent radiation anymore. As a result of the lower fluence, the relative abundance of the highest charge states is lower and the maximum observed charge state is Ar^{14+} with Ar^{11+} still being the most prominent peak amongst the higher charge states.

For better visibility the abundance of the single charge states of argon for x-ray pulse lengths of 49 fs, 67 fs and 85 fs relative to the measurement at 30 fs is displayed in Fig. 6.6. For longer pulses the high charge states above Ar^{9+} increase compared to shorter pulses, while the lower charge states are almost unchanged. This behavior is similar to the pulse length dependent ionization in neon observed by Young *et al.* [7] and as well described in section 2.7. When L-shell electrons are removed by the leading edge of the x-ray pulse the atoms are more transparent to the pulse until an Auger decay happens and the vacancies are refilled. In a longer pulse it is more likely that Auger decays happen during the pulse and the average photoabsorption cross section is higher, leading to more absorbed photons and an increased yield of high charge state. In other words, argon atoms are more transparent to shorter x-ray pulses compared to longer ones with the same number of photons. However, this effect can only be observed if a sufficient number of photons per atom are absorbed within a time on the order of the Auger lifetimes, i.e., in the central part of the focus. All charge states that are dominantly produced in outer parts of the focus where the intensity is lower do not show a pulse length dependence. For the current experimental

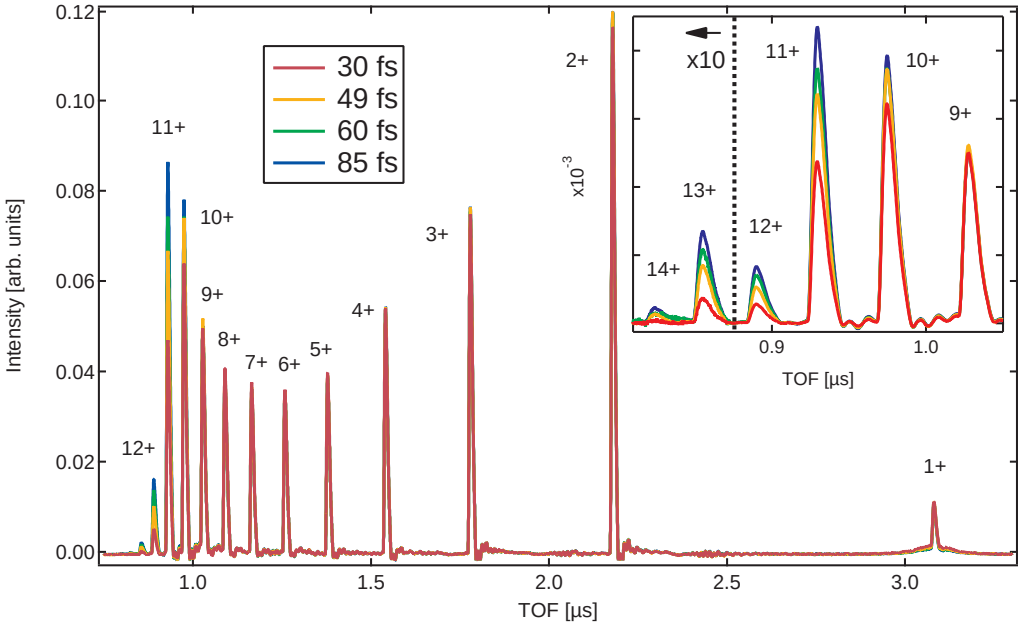

Figure 6.5: Tof spectra of atomic argon for different x-ray pulse length from 30 fs to 85 fs and the same x-ray pulse energy of 0.2 mJ. For longer pulses the higher charge states (>9+) increase. The inset shows a more detailed view of these charge states. The relatively small overall change with pulse length can be explained with the focal intensity distribution. The lower charge states stem from regions where only few photons per atom are absorbed and therefor the ionization process is not as sensitive to the pulse length.

conditions these are all charge states below Ar^{9+}. Even though about 4-5 photons are needed to produce Ar^{9+} the pulses are not short enough yet to induce significant transparency.
As a measure for the relative absorption the average charge state $\bar{q}$ of the argon atoms is calculated from the yield of the single charge state peaks I_q and their charge q as:

$$\bar{q} = \frac{\sum_{q=1}^{14} I_q \cdot q}{\sum_{q=1}^{14} I_q} \tag{6.1}$$

In Fig. 6.7 the average charge state of argon atoms as a function of the pulse energy is shown. It increases with increasing pulse length. This can be directly attributed to an increase in absorption for longer pulses. Vice versa, the transparency induced by the x-rays increases with decreasing pulse length.

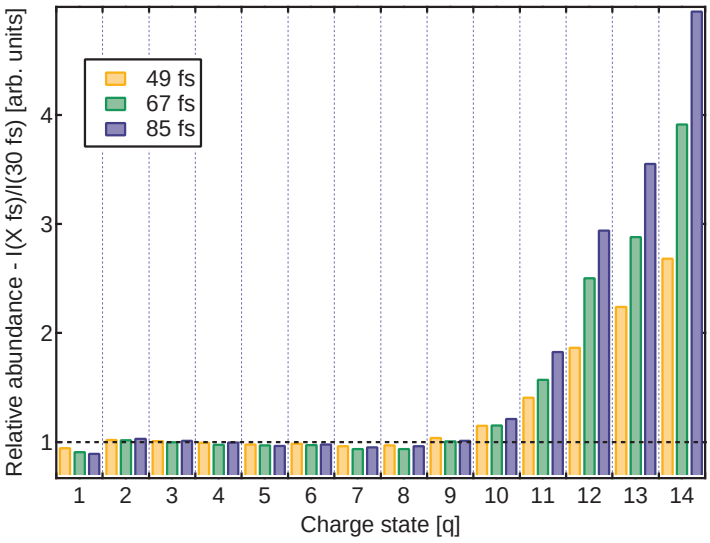

Figure 6.6: Relative abundance of argon charge states for pulse lengths of 49 fs, 67 fs and 85 fs extracted from the tof spectra shown in Fig. 6.5. The different charge states are normalized to the value for a 30 fs pulse. For charge states above 9+ there is a clear increase for longer pulses.

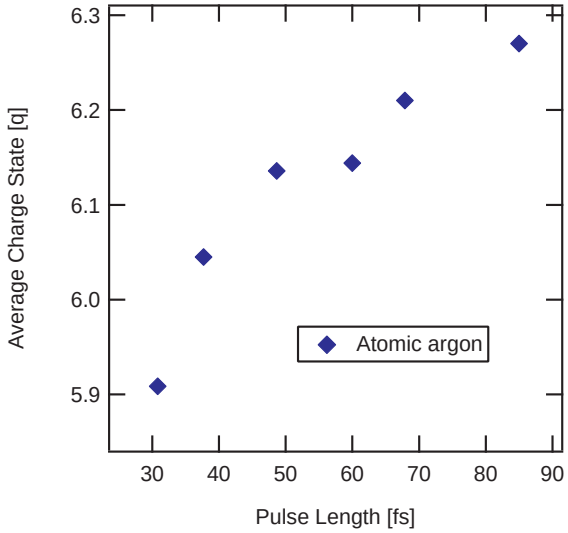

Figure 6.7: Average charge state as a function of pulse length for atomic argon at a photon energy of 480 eV and a pulse energy of 0.2 mJ. The average charge state increases for longer x-ray pulses.

6.5 Argon clusters in intense x-ray pulses

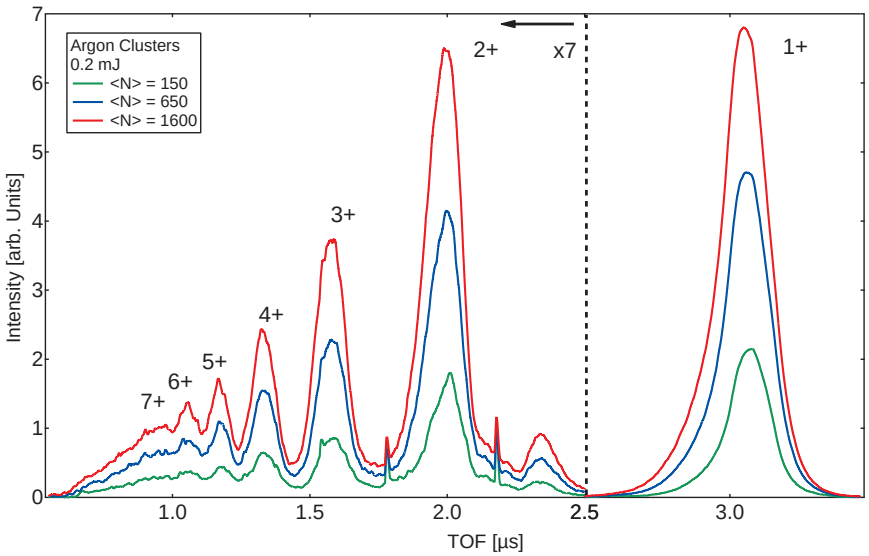

Figure 6.8: Ion tof spectra for different clusters with a size of $\langle N \rangle = 150$, $\langle N \rangle = 650$, and $\langle N \rangle = 1600$ atoms. For better visibility the part of the spectrum to the left of the dashed line is multiplied with a factor seven. The peaks of the different argon charge states are broadened and shifted compared to the atomic spectra in Fig. 6.3 due to kinetic energy of the cluster fragments. There are less high and more low charge states and a prominent Ar^{1+} peak. This is due to recombination and charge transfer processes in the cluster nanoplasma after the x-ray pulse is over.

In the following section the results of measurements of the ionization of argon clusters in intense x-ray pulses are presented. Cluster spectra for different sizes are compared and the differences to an atomic spectrum is explained. For all cluster measurements, the HFP chamber was positioned in a way that the interaction region is above the edge of the tof slit aperture (c.f. Fig. 4.8) and the atomic background is mostly suppressed.

In Fig. 6.8 tof spectra of clusters with different sizes at a photon energy of 480 eV and a pulse energy of 0.2 mJ are shown. Compared to the atomic argon spectrum in Fig. 6.3 the peaks representing the different charge states are shifted an broadened in the cluster spectra. The higher charge states are even overlapping each other. Further, the charge state distribution in the cluster spectra is different from the atomic case. The Ar^{1+} peak is highest and the intensity of the peaks decreases with increasing charge state in contrast to the atomic spectrum in Fig. 6.5 with a local maximum at Ar^{11+}. Theses differences in the cluster spectra compared to the atomic spectra are due to processes happening in the cluster after the light is absorbed (c.f. chapter 3). They are explained and assigned in the following.

In the nanoplasma that is formed during the ionization, charge can be very easily distributed even if the atoms in the cluster are initially ionized inhomogeneously. This leads to a more con-

tinuous charge state distribution compared to the atomic case. After the ionization the cluster expands and recombination in the cooling nanoplasma is possible. The recombination leads to lower observed charge states than for atoms. Another process leading to lower charge states compared to the atom, especially the large Ar^{1+} peak, is due to the focal profile of the x-rays. In atoms, two or more charges are created most of the times even if only a single photon is absorbed. For the atoms in the cluster, this is also true but the charge can be distributed to neighboring neutral atoms resulting in mainly singly charged fragments [65].
The broadening and shifting of the peaks for the charge states can be explained with kinetic energy release of the ionic cluster fragments after the expansion or explosion of the cluster. The slit aperture of the tof spectrometer limits the transmission to ions flying in a small angle compared to the spectrometer axis either towards or away from the detector and suppresses most of the atomic background (c.f. Fig. 4.8). Ions with a velocity component towards the detector will hit it earlier and ions with a velocity component away from the detector will hit it later than ions with the same charge and no kinetic energy. In general this leads to three peaks for every charge state. A small central sharp peak, that is still visible, from atoms in the residual gas without kinetic energy. A broad peak at earlier tof from ions flying towards the detector and a broad peak at later tof from ions flying away from the detector. The amount and distribution of kinetic energy of the ions determine the shape and separation of the forward and backward peaks. All three peaks can be seen for the Ar^{2+} charge state in Fig. 6.8 which also compares to the part of the tof spectrum shown in Fig. 4.8.
Because the atomic background is mostly suppressed by the slit aperture the signal from residual atomic argon is very weak. The backward peak is much weaker than the forward peak because of the smaller effective solid angle for the backwards flying ions and the spectrometer transmission. For higher charge states the backward peak starts overlapping with the forward peak of the preceding charge state. In the case of the Ar^{1+} the small kinetic energy of the fragments and a continuous kinetic energy distribution results in a complete overlap of the forward and backward peak.

6.6 Pulse length dependent ionization of argon clusters

The central results for the investigation of the ionization dynamics of clusters is the pulse length dependent data that will pe presented in the following section. By tuning the x-ray pulse length the dynamics of the ionization process in the cluster can be studied. In Fig. 6.9 two cluster spectra for a pulse length of 30 fs and 85 fs and a pulse energy of 0.15 mJ are shown. The inset in Fig. 6.9 represents a tof spectrum of atomic argon at a pulse energy of 0.15 mJ and a pulse length of 50 fs for comparison. In the cluster spectrum for the 30 fs pulse the yield of low charge states is higher and the yield of high charge states is lower compared to the 85 fs pulse. In

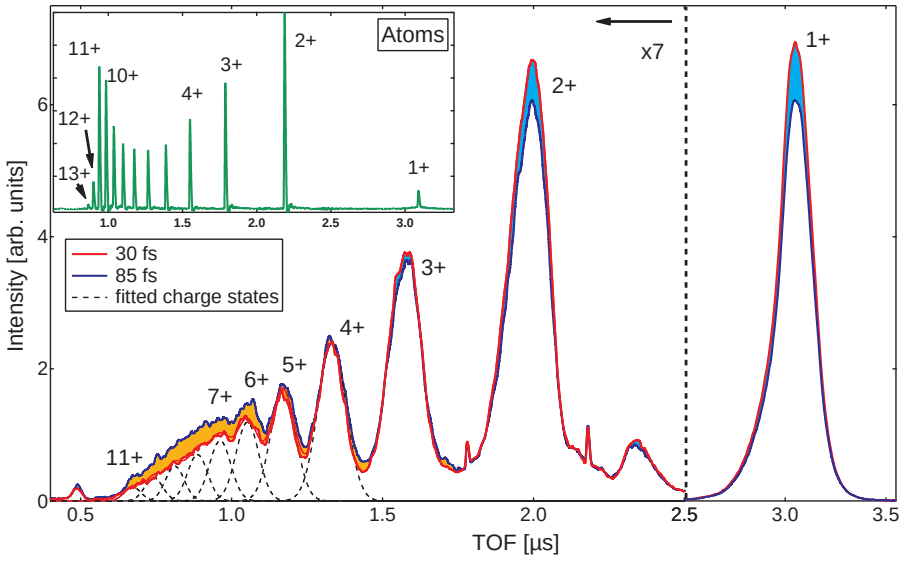

Figure 6.9: Time-of-flight spectra from argon clusters with a size of $\langle N \rangle = 1600$ atoms for 30 fs and 85 fs x-ray pulse length and 0.15 mJ pulse energy. The difference between long and short pulses is indicated in orange (higher intensity for long pulses) and blue (higher intensity for short pulses). The dashed lines indicate the fitted charge states when they are not clearly separated anymore. Inset: Atomic argon time-of-flight spectrum for the same pulse energy and 50 fs pulse length.

more detail, for the shorter pulse the Ar^{1+} and Ar^{2+} peaks are increased by the blue shaded area and the charges states of Ar^{6+} and above are decreased as indicated by the yellow shaded area. Ar^{3+} to Ar^{5+} exhibits similar intensities. Generally speaking, these differences lead to a decreased average charge state for the short pulse spectrum. Qualitatively the observed behavior is similar to the x-ray pulse length dependencies observed in atomic argon. However it is interesting to note that compared to the atomic spectra, in clusters the low charge states also exhibit a pulse length dependance. The yield of Ar^{1+} and Ar^{2+} decreases with increasing pulse length. This pulse length dependence indicates that some of these low charge states in clusters, unlike in atoms, are produced in the central part of the focus where the x-ray intensity is high. As all atoms in the cluster in this part of the focus are initially highly ionized, these Ar^{1+} and Ar^{2+} ions must be produced through electron-ion recombination processes of higher charged ions.

Discussing the absorption dynamics of clusters in intense laser pulses poses the difficulty that the spectra from different cluster sizes are not directly comparable to each other due to secondary processes affecting the tof spectra. These processes include recombination and thermally driven expansion and Coulomb explosion of the nanoplasma which are explained earlier in this section and in chapter 3. While the primary absorption process does not depend on the cluster size except for the time-dependent effects discussed in this work, these secondary processes strongly depend on the size of the cluster. When spectra for different cluster sizes and pulse length

are compared it is not clear what changes are attributed to the ionization dynamics and what changes to size-dependent secondary effects, e.g. expansion or recombination. To overcome this hurdle it was taken advantage of the fact that the secondary processes are slow compared to the femtosecond x-ray pulse [70]. Therefore the same number of absorbed photons will lead to the same final ion yield spectrum and thus, average charge state. By this means a measure for the time-dependent component of the absorption can be found for every cluster size. The first step in this method, that has to be taken before the data is analyzed in more detail, is to calculate the average charge state as a measure for the absorption. In the following section it is explained how the average charge stat is determined from the cluster tof data.

6.7 Average charge state for cluster spectra

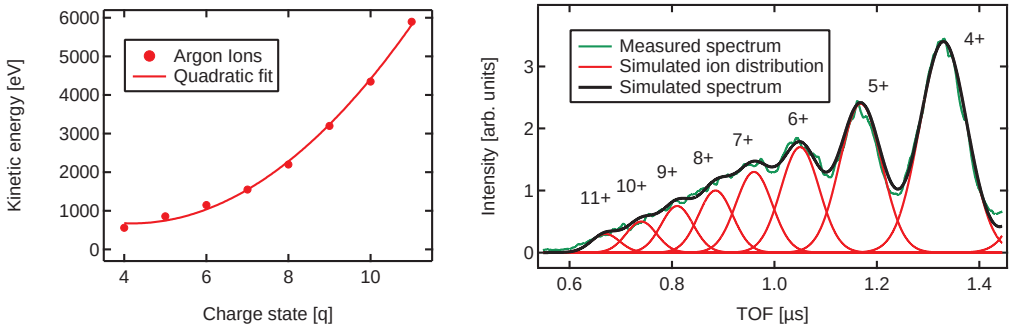

Figure 6.10: Fitting of the charge states in the argon cluster spectrum using SIMION. Left: Centroid of the kinetic energy distributions as a function of charge state. Right: Simulated ion distributions for the single charge states (red) and resulting summed spectrum (black) compared to the measured spectrum (blue).

For the analysis of the cluster absorption as function of the x-ray pulse length the average charge states of clusters are determined from the ion yield spectra displayed in Fig. 6.9. Due to their kinetic energy, the cluster fragments with charges higher than 4+ can hardly be separated. To compute the average charge state from the tof spectra the SIMION simulation shown in section 4.7 is used to fit higher charge states under the assumption of a quadratic increase in kinetic energy with ion charge state in good agreement with the data and earlier results [81]. Fig. 6.10 shows the simulated average kinetic energies of the argon ions with a charge higher than 4+. The simulated ion peaks of the charge states Ar^{4+} and above are depicted as black dashed lines in Fig. 6.9. For the calculation of the average charge state the transmission of the single charge states were normalized according to their simulated kinetic energy kinetic. It is important to note that the main purpose of this routine is to assign a charge to every part of the spectrum

and to identify spectra with similar charge state distributions for the same cluster size. Therefor possible inaccuracies in the assumptions for the charge state assignment are irrelevant as long as the same assignment is used for all spectra of the same cluster size.

6.8 X-ray induced transparency increase (XITI)

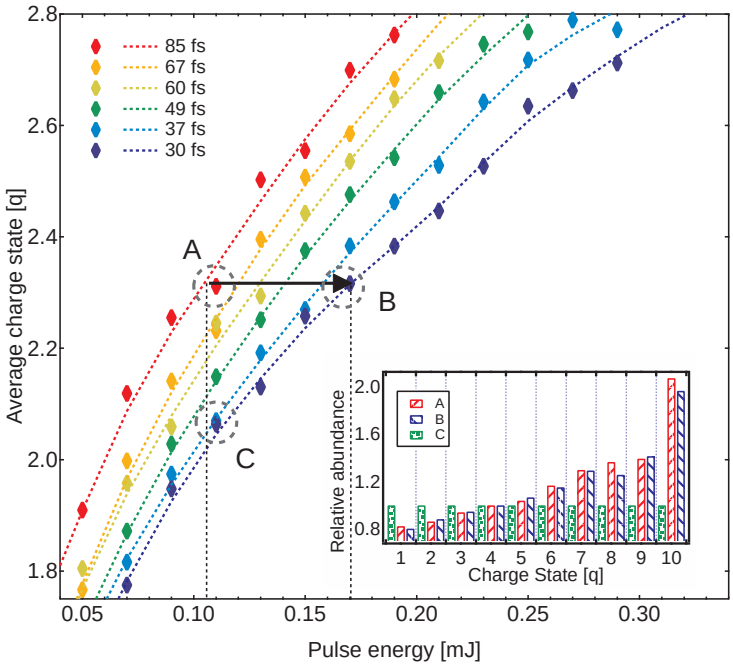

Figure 6.11: Average charge state of the detected ionic cluster fragments vs. x-ray pulse energy for clusters with an average size of $\langle N \rangle = 1600$ atoms. The different colors indicate different pulse length. The diamond shaped markers are binned data points and the dashed lines interpolated curves. The black horizontal arrow marks the XITI from a 30 fs to a 85 fs pulse. Inset: Abundances of charge states at point A, B and C. For better visibility the single charge states are normalized to the value of point C.

As explained earlier (c.f. section 6.6) tof spectra for different cluster sizes are not directly comparable. Therefore, an independent measure for the time-dependent effects in the absorption, i.e., the Auger lifetimes of the sample, for every cluster size is needed. This measure is called x-ray induced transparency increase (XITI). In the following it is shown how the XITI is extracted from the data sets for atomic argon and four argon cluster sizes and how it is related to time-dependent effect during the ionization.

In the experiment tof spectra for different pulse lengths (30 fs - 85 fs) and pulse energies were recorded for atoms and four cluster sizes. The principle of extracting the XITI from the data is explained as an example for clusters with a size of $\langle N \rangle = 1600$. In Fig. 6.11 the measured average charge state as a function of the pulse energy of a $\langle N \rangle = 1600$ cluster for six different x-ray pulse lengths is plotted. Every data point is computed from an averaged tof spectrum containing a few thousand laser shots within a pulse energy bin of $\delta E = 0.02$ mJ. The dotted lines are interpolations of the data bins. In the data two trends are apparent: First, for constant pulse length the average charge state increases with increasing pulse energies (along each curve in Fig. 6.11). Second, for constant pulse energies the average charge state increases with longer

pulses (going vertically up in the set of curves in Fig. 6.11). In the inset of Fig. 6.11 the ion yield distributions (i.e. spectra) for the three distinct points A, B, and C are compared. For better visibility the single charge states are normalized to the value of point C. It shows that fundamentally the same average charge state for the example points A and B are generated by the same charge state distribution.

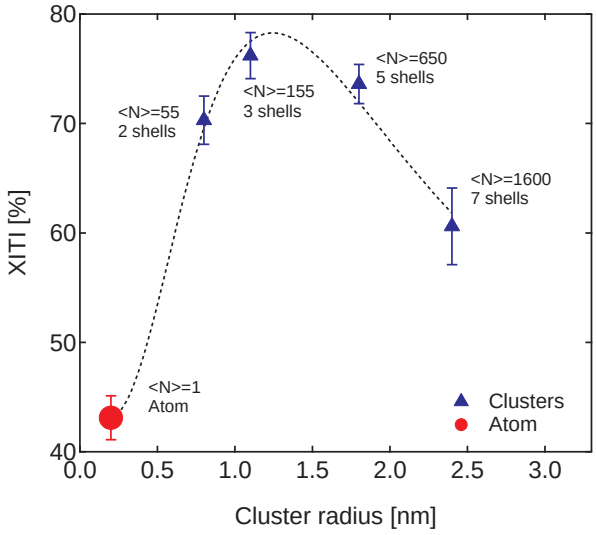

Figure 6.12: XITI from 85 fs to 30 fs x-ray pulse length for atoms and different cluster sizes ranging from $\langle N \rangle = 55$ atoms (2 geometric shells) to $\langle N \rangle = 1600$ (7 geometric shells). The dashed line is a guide to the eye.

To measure the same average charge state for a long (e.g. 85 fs, point A) and a short (e.g. 30 fs, point B) pulse, a higher pulse energy is needed for the short pulse. The horizontal arrow in Fig. 6.11 illustrates this difference in pulse energy. Specifically, for the $\langle N \rangle = 1600$ cluster in Fig. 6.11, 60% more pulse energy, i.e., photons are needed to produce the same average charge state with a 30 fs pulse compared to a 85 fs pulse. In other words, an argon cluster of $\langle N \rangle = 1600$ atoms is 60% more transparent for an intense 30 fs x-ray pulse compared to an 85 fs one. We define this as x-ray induced transparency increase (XITI) of 60% in a 30 fs pulse compared to a 85 fs pulse for a fixed initial pulse energy. It is pointed out that XITI is purely a measure for the time-dependent components in the absorption, i.e., the lifetime of the inner-shell vacancies. All processes that influence the absorption and that are not time-dependent do not have an impact on the XITI. This is because for both point A and B in Fig. 6.11 the same number of photons are absorbed by the sample. For a better understanding one could imagine a situation where purely valence ionization occurs and no time-dependent effects such as inner-shell vacancy decays can possibly happen. In this case a pulse with the same number of photons would always lead to the same number of absorbed photons regardless of the pulse length, given non-sequential multi-photon absorption does not occur. For argon excited with intense 480 eV x-ray pulses the

inner-shell vacancy lifetime and thus the XITI, is dominantly determined by the Auger rates as fluorescence decay does not play a role for the XITI of argon at 480 eV (c.f. section 2.4).
The next step is to investigate the size-dependence of the ultrafast x-ray absorption. Therefore similar data sets to the one exemplified in Fig. 6.11 have been acquired for an atomic target and four cluster sizes ranging from $\langle N \rangle = 55$ to $\langle N \rangle = 1600$. The XITI for the atom as well as for the clusters for the same pulse length combination of 85 fs and 30 fs has been determined as explained above. The result is summarized in Fig. 6.12. First and foremost, the XITI in Fig. 6.12 is much higher for all cluster sizes compared to the atom reference which can be directly attributed to changing Auger lifetimes in the clusters. Further, the XITI varies systematically within the different samples indicating a dependence of the Auger rates on the cluster size. It increases from atoms to small clusters and decreases for larger clusters again. The relative change of the Auger lifetime with the cluster sizes is encoded in the shape of the curve in Fig. 6.12 which can be explained as follows.
Fig. 6.13 shows an illustration of the general dependance of the XITI on the Auger lifetime in an atomic system for ionization with x-ray pulses of two fixed length. For simplicity an atom with only one inner-shell electron and eight valence electrons is assumed as shown in the upper left in Fig. 6.13. When the inner-shell electron is removed this system is quasi transparent until the hole is refilled via Auger decay. This atomic system is ionized by x-ray pulses with a rectangular temporal profile of two different length and the same number of photons, that are represented by green lines. The long pulse has the length τ_1 and a short pulse the length τ_2. X-ray pulse energy, i.e. number of photons, is chosen such that, assuming the inner shell was immediately refilled after ionization, four photons would be absorbed in both cases. Accordingly, the potential ionization events, i.e. the ionization rate, are indicated with vertical orange dotted lines. Below the x-ray pulses an inner-shell photoionization is marked as a light blue arrow and the Auger decay as red arrow. The horizontal extension of the red arrow represents the Auger lifetime. In Fig. 6.13 three distinct possibilities for the Auger lifetime of this system are shown. In case (a) the Auger lifetime T is much shorter than the two pulse length τ_1 and τ_2, in case (b) T is on the order of τ_1 and τ_2, and in case (c) T is much longer than τ_1 and τ_2. The number of absorbed photons for every case is indicated inside the blue circles.
For a very short Auger lifetime T in case (a) the inner-shell hole is always refilled between two possible ionization events (orange dotted lines). Therefore, the number of absorbed photons for both pulse lengths is similar (four) and eight electrons are removed from the atom in total. That is, the sample exhibits the same absorption for both pulse length which results in a XITI of 0. If the Auger lifetimes are such that they are close to the used pulse lengths, they play a role in the sequential absorption processes. This is shown in case (b). In the long pulse the potential ionization events are still spread enough in time to allow for an Auger decay resulting in four absorbed photons. For the short pulse, however, the potential ionization events are temporally closer resulting in only two absorbed photons resulting in a XITI from the long to the short pulse that is greater than 0. In other words, a shorter pulse will see a more transparent sample

because on average the probability that the vacancies are filled is lower compared to a longer pulse. Therefore, the XITI will be greater than 0 and it will depend sensitively on the Auger lifetimes. For a very long Auger lifetime in case (c) the absorption for both pulses is similar again. The Auger decay does not happen between two potential ionization events and for both pulse lengths only one photon is absorbed. Thus, the XITI is 0.
The general behavior of the XITI as a function of the Auger lifetime is summarized in the upper right of Fig. 6.13. For Auger lifetimes much shorter (a) and much longer (b) than the x-ray pulse length the XITI is close to 0. In between, for Auger lifetimes close to the x-ray pulse length, there is a maximum where the XITI is greater than 0. This maximum compares to the maximum of the measured XITI for argon clusters in Fig. 6.12 indicating an increase of the Auger lifetime from argon atoms to clusters and with the cluster size. To support this arguments and to further investigate the impact on Auger lifetimes on the curve shape, the XITI of a simplified and well understood system as a function of inner-vacancy lifetimes is simulated with a rate equation model. The result of the simulations is presented in the following section.

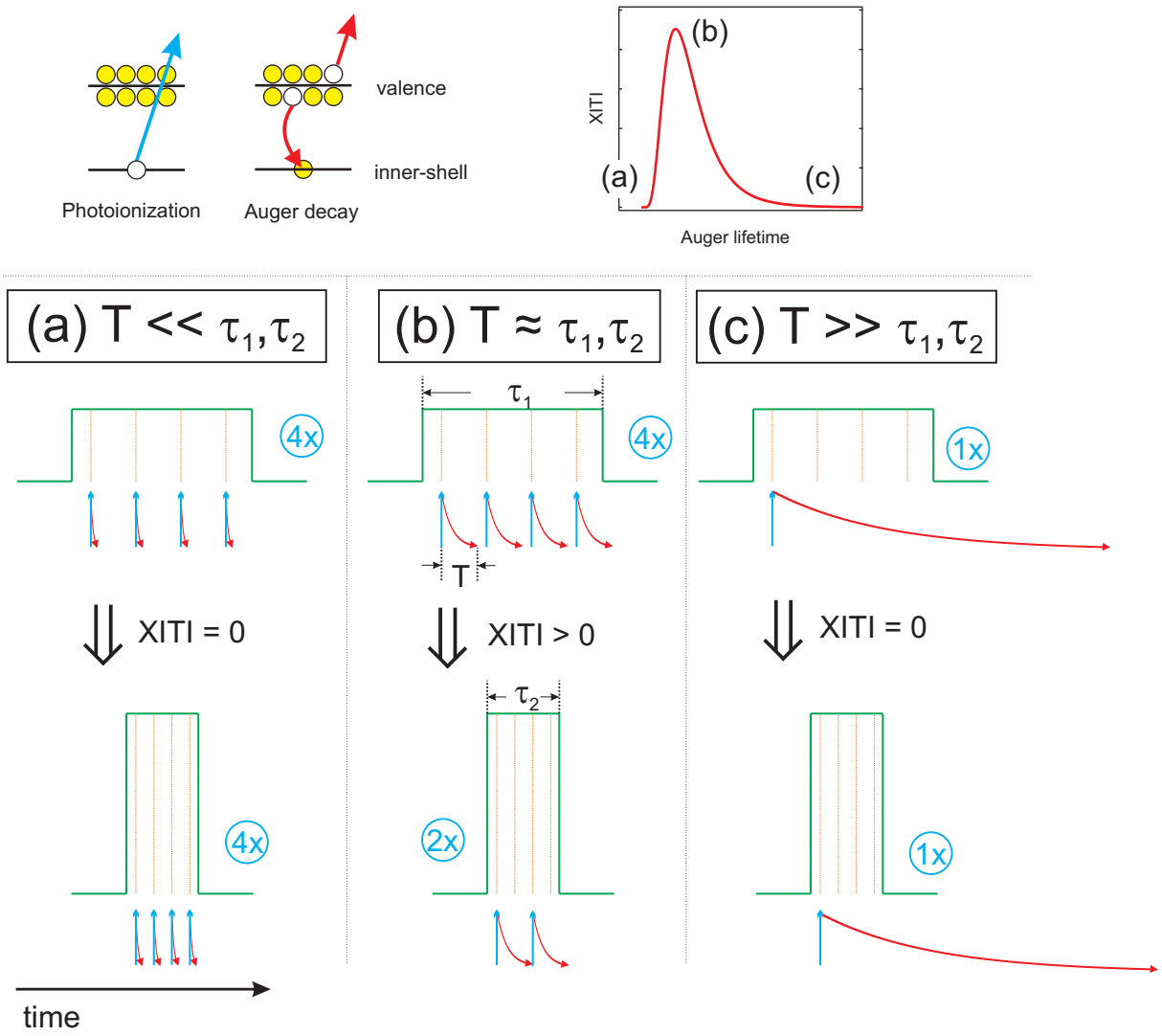

Figure 6.13: Illustration of the dependance of the XITI on the Auger lifetime for two fixed x-ray pulse length (for more detailed explanation see text). A simplified atomic system with one inner shell electron and eight valence electrons is assumed (c.f. upper left). It is transparent after a photoionization event (blue arrow) until the Auger decay happens (red arrow). In the lower part the three distinct cases for the Auger lifetime are explained. X-ray pulse profiles are indicated with green lines and the ionization rate is marked as orange dotted lines. The number of absorbed photons for every combination of pulse length and Auger lifetime is written in a blue circle.
(a) The Auger lifetime T is much shorter than the pulse lengths τ_1,τ_2. For both pulses the Auger decay happens on a time scale shorter than the temporal spacing between two potential ionization events, leading to similar absorption of four photons (XITI=0).
(b) The Auger lifetime is on the order of the pulse lengths. For the shorter pulse less photons get absorbed because the Auger happens on a longer time scale compared to the temporal spacing between two ionization events (XITI $>$ 0).
(c) The Auger lifetime is much longer than the pulse lengths. The absorption is similar for both pulse lengths because the Auger lifetime is much longer than the temporal spacing between two potential ionization events.

6.9 Simulation of the XITI

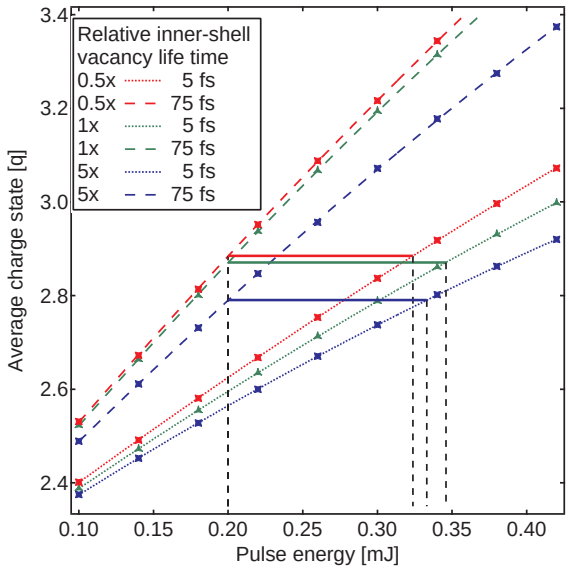

Figure 6.14: Simulated average charge states for neon atoms in a 5 fs and 75 fs. The inner-shell vacancy lifetime has been artificially modified as indicated in the graph. These curves are used to determine the XITI in the same way as in Fig. 6.11 for the argon clusters.

Rate equation models similar to the one described in chapter 5 have been used to describe the absorption of neon atoms in intense x-ray pulses [7]. For argon, however, multiple ionization via unknown intermediate excited states becomes important as explained in section 6.3. These unknown processes add uncertainty to the simulations. Specifically, the unexpected high charge states above Ar^{10+} observed in the atomic spectra shown in Fig. 6.9 indicate that these processes play an important role under the current experimental conditions. Therefore neon is chosen for this proof-of-principle simulation because all relevant rates and states are known. Details about the rate equation model that was developed for this work are explained in chapter 5. The results of the simulations agree well with experimental neon ion spectra at different pulse lengths. Also earlier work performed by Young *et al.* found good agreement between an ionization rate equation model for neon and experimental data [7]. To simulate the XITI the average charge states from ion yields for different pulse lengths and pulse energies were calculated. To investigate the impact of the inner-shell vacancy lifetimes they are artificially varied in the calculations. The resulting average charge states as a function of pulse energy is plotted for pulse lengths of 5 fs (dotted lines) and 75 fs (dashed lines) in Fig. 6.14. The green lines show the neon-like system with the natural lifetimes, for the blue line all lifetimes have been multiplied by 5 and for the red line all lifetimes have been multiplied by 0.5. From the results the XITI is determined as described above for the experimental data (c.f. Fig 6.11). It is also noted that the pulse length are chosen to be slightly shorter than in the experiment to make up for the shorter lifetimes in

the modeled neon-like system compared to argon. The horizontal lines in Fig. 6.14 indicate two points with the same average charge state. Their length shows the XITI for the respective set of lifetimes with respect to a 5 fs and 75 fs x-ray pulse. It can be seen that the XITI is lowest if the inner-shell vacancy lifetimes are multiplied with a factor 0.5, it increases when multiplying the lifetimes with a factor 1 and decreases again when multiplying the lifetimes with a factor 5. In Fig. 6.15 the simulated XITI is plotted as a function of different multipliers of the lifetimes. The three cases shown in Fig. 6.14 are indicated with colored arrows. Overall, the shape of the simulated curve is very similar to the one deduced from the experimental data displayed in Fig. 6.12. The XITI goes through a maximum for intermediate lifetimes and decreases for shorter as well as for longer lifetimes.

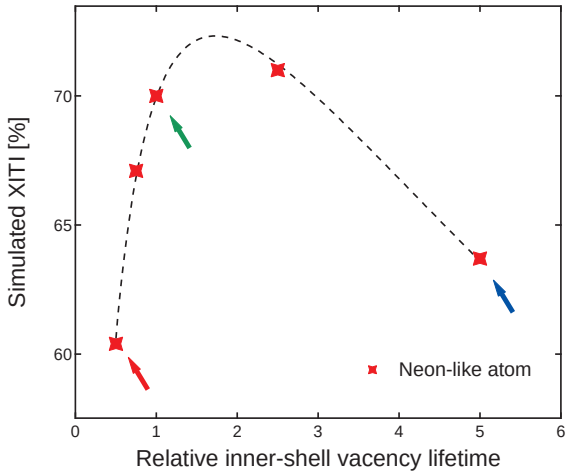

Figure 6.15: Simulated XITI of an atomic Ne-like system extracted from the data shown in Fig. 6.14. The colored arrows refer to the respective plots in Fig. 6.14. All lifetimes of the inner-shell vacancies are artificially multiplied by the linear factors shown on the x-axis. The dashed line is a guide to the eye. The simulated XITI exhibits qualitatively the same shape as the cluster-size dependent XITI (c.f. Fig. 6.12) and goes through a maximum for intermediate lifetimes, indicating that different cluster sizes result in different inner vacancy lifetimes.

6.10 Discussion

The measured XITI for argon clusters shown in Fig. 6.12 shows an increase of the XITI for argon atoms to argon clusters. Further, the XITI goes through a maximum for small clusters and decreases for larger clusters. The variation in the XITI can clearly be associated to a change in Auger lifetimes as the Auger decay is the only significant time-dependent process that influences the absorption of the argon L-shell. The simple model discussed in Fig. 6.13 indicates that the maximum of the XITI can be associated to an increase in Auger lifetime for increasing cluster size. Concurrent with this model, simulations using a rate equation model of a neon-like atomic system show a similar behavior of the XITI for increasing inner-shell vacancy lifetime. The experimental data in combination with the simulation show that in intense x-ray laser pulses the Auger lifetimes of nanoscale samples increase with size.

The Auger lifetimes have been theoretically predicted by Saalmann *et al.* to change for clusters in intense x-ray pulses compared to atomic samples [19]. Fig. 6.16 gives an illustration of the processes in the cluster ionization leading to reduced Auger lifetimes in the nanoplasma. As explained in chapter 3 the atoms in a cluster are ionized by the x-ray pulse through inner-shell photoionization and Auger decay (a). With every ionization event the positive cluster Coulomb potential increases (b). At some point the photo- and Auger electrons cannot leave the cluster any more (c). This massive creation of charges leads to suppression of the Coulomb barrier between the atoms in the cluster [78]. At least the high laying valence electrons are then turned into quasi-free electrons and they are effectively delocalized (d). Consequently, the overlap between these electrons and the localized inner-shell vacancies decreases and therefore the Auger rates are reduced [19]. As outlined in section 2.7, longer Auger lifetimes result in a decreased absorption. This is because inner-shell holes are refilled slower and the sample remains with a transiently increased transparency for a longer time. Therefore, the increase in Auger lifetime for argon clusters results in decreased absorption with increasing cluster size.

Fig. 6.17 shows a calculation of the absorbed energy per atom for atomic argon and different argon cluster sizes as a function of the field strength, i.e, intensity of the x-ray pulse [19]. The data has been calculated for a photon energy of 350 eV. For low intensities the absorbed energy is similar for atoms and both cluster sizes. This compares to a region of the x-ray focus where the intensity is low and the induced transparency effects are minor. For higher intensities the absorption is different for and atoms and clusters. The clusters absorb fewer photons than the atom and the larger cluster absorbs less than the smaller cluster. It is noted that in these calculations two effects account for the reduced absorption of clusters. First, the decrease in Auger lifetime, that is subject of the present study. Second, a shift in the binding energy of the valence electrons compared to a cluster without interionic barrier suppression. As the second effect is not time-dependent it is not observed in the present study.

While a quantitative statement about the increase of Auger lifetimes in the Ar clusters is difficult without detailed calculations, a crude estimate can be given. If the XITI is assumed to be linear

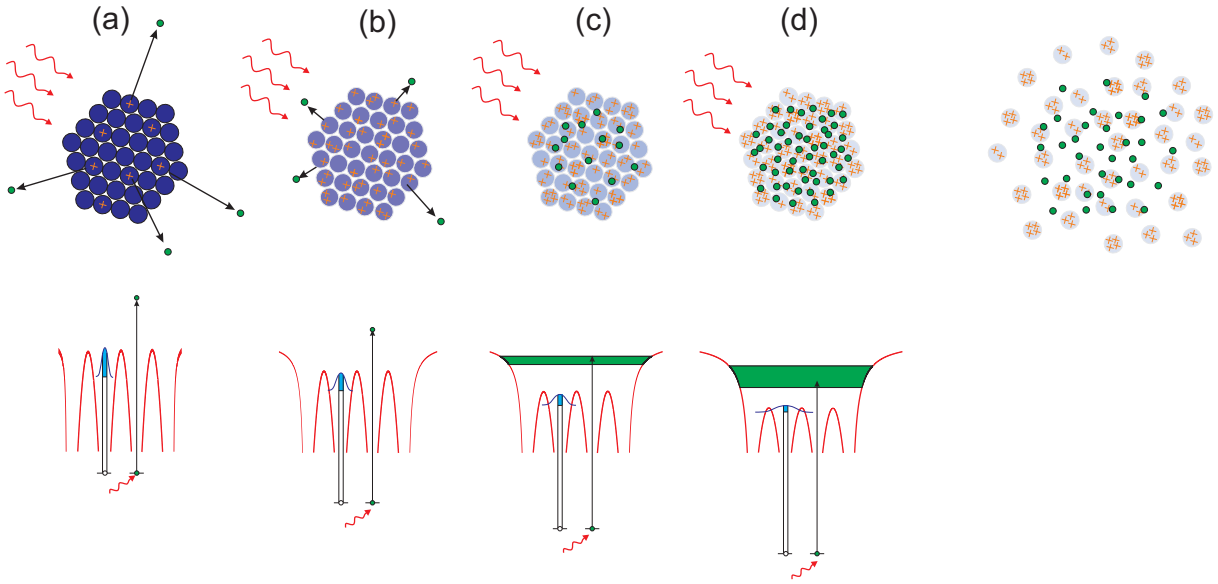

Figure 6.16: Scheme of the potential barriers in a highly excited cluster in an intense x-ray pulse for different times during the pulse. In the beginning of the pulse (a) photoelectrons and Auger electrons can still escape the cluster. When the cluster charge increases (b) the electrons cannot leave the cluster anymore (c). Due to the charges of the trapped electrons the barriers between the single atoms are lowered. This leads to delocalization of the valence electrons an subsequently smaller overlap between inner-shell holes and the valence electrons (d).

between a lifetime of zero and the maximum, the measured increase by a factor two from the atom to $\langle N \rangle = 155$ in Fig. 6.12 can be translated to a factor two increase in average lifetimes as a lower limit. This is in good agreement with the factor five predicted by the calculations of Saalmann *et al.* for slightly different pulse conditions [19].

Another outcome of this study contributes to the ongoing discussion whether electron-ion recombination occurs in expanding hot nanoplasmas produced by the intense x-ray pulses. For large xenon clusters it has been shown that in the most intense part of the focus the electron temperature is high enough so that electron-ion recombination is nearly impossible resulting in exclusively highly charged fragments detected from a single cluster [10]. According to these results lower charge states are purely a result of clusters that are illuminated in the much less intense part of the focus. In a different publication lower charge states and the kinetic energy distribution of the fragments are explained with electron-ion recombination in the expanding hot nanoplasma [44]. In the present study indications for recombination in the intense part of the focus were observed. The difference in the ion tof spectra of atoms and clusters for different pulse lengths can clearly be assigned to the most intense part of the focus (c.f. section 2.7). For atoms and molecules the result is an increase of high charge states that are produced in this part of the focus for longer pulses (c.f. Fig. 2.18, Fig. 5.3, Fig. 6.5, and Ref. [7, 8]). In the cluster spectra in Fig. 6.9 however, in addition to an increase of high charge states for longer pulses a decrease

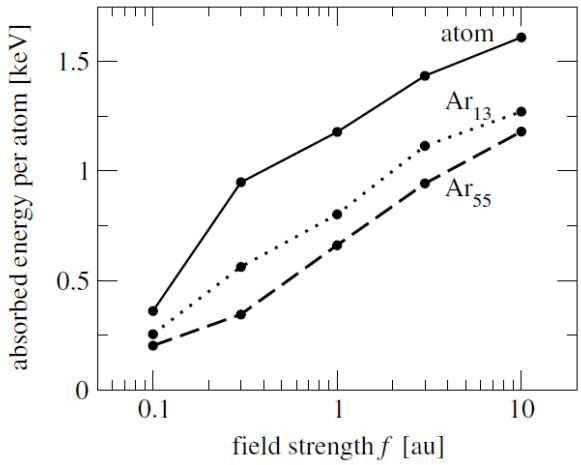

Figure 6.17: Simulation of the absorbed energy per atom for an atom and clusters of different sizes in intense x-ray pulses by Saalmann *et al.* [19]. Due to the reduced Auger rates and the lowered binding energy of the valence electrons clusters absorb less energy than atoms and larger cluster less than smaller clusters.

of low charge states (Ar^{1+} and Ar^{2+}) is observed. This indicates that these charge states are produced through electron-ion recombination in the most intense part of the focus where initially all atoms are highly ionized. It should be noted that the studies mentioned above [10, 44] where performed at a photon energy of 800 eV and 850 eV while the current study was performed at a photon energy of 480 eV. The photon energy is an important parameter because the probability for electron-ion recombination in a plasma is proportional to $1/T^4$ with T being the temperature of the plasma.

In addition to the results in free clusters, this study also yields insight into a hitherto uninvestigated regime of the ionization of argon atoms. At the highest x-ray intensities argon ions with a charge of up to Ar^{16+} with a maximum intensity at Ar^{11+} were observed at a photon energy

Charge state	2s	2p	3s	3p	IP(2s)	IP(2p)	IP(3s)	IP(3p)
4+	0	4	2	6	-	428	114	92
5+	0	3	2	6	-	485	139	117
6+	0	2	2	6	-	553	165	144
4+	2	2	2	6	493	445	115	93
5+	2	1	2	6	540	503	141	117
6+	1	1	2	6	595	554	166	144
7+	0	1	2	6	-	607	194	173

Table 6.2: Differential ionization potentials of selected hollow states of argon Los Alamos Atomic Physics Code [59].

of 480 eV (c.f. Fig. 6.3). In other words all electrons except for the 1s core electrons could be removed from the argon. This is surprising because the ground state ionization potential (IP) of Ar^{10+} is with 539 eV already higher than the photon energy and the IP of Ar^{15+} is 918 eV. The most likely pathway to these high charge states is ionization via intermediate states that can be resonantly exited. These can either be empty valence states or Rydberg states that shift down in energy an get within reach from the inner-shell levels. Other pathways that lead to such high charge states can be excluded. Simultaneous multi-photon absorption is very unlikely (c.f. section 2.5) and has not been observed at the LCLS even in more favorable conditions [18]. In principle also the production of extreme hollow atoms that are subsequently valence ionized or Auger decay could explain these high charge states. Tab. 6.2 shows differential IPs for a selection of extreme hollow atoms of different charge states. Already the IPs of the 2p shell in hollow Ar^{5+} are slightly above the photon energy of 480 eV and in Ar^{6+} they are clearly above. Even if all eight valence electrons of Ar^{6+} would be removed via direct ionization only Ar^{14+} could be reached. However, the Auger lifetimes in such extreme hollow atoms are very short because of the strong population inversion. Therefore, it is unlikely that these hollow ions are even produced through removal of five or six L-shell electrons are before a single Auger decay happens. In addition to that, even if such hollow atoms were produced, the valence ionization rate in these ions would be much lower than the Auger rates. This means inner-shell holes would be refilled via Auger decay before many valence electrons are removed. In other words, extreme hollow ions would relax to a ground-state-like configuration very quickly before enough electrons from the valence shell could be removed to produce charge states on the order of Ar^{12+} to Ar^{14+}.
Therefore the ionization via intermediate excited sates is the most likely explanation for the production of higher charge states. While in lighter atoms this effect clearly do not play a major role [7], indications for similar effects have been observed in much heavier atoms [93]. There, the ionization via resonant excitation has been identified as a likely ionization pathway in electronically complicated systems. However, all results so far achieved are of qualitative character. The detailed electronic structure of these highly excited atoms and the dynamics of the ionization process has not yet been understood. Argon plays a key role in the investigation of ionization via intermediate resonant states because it is one of the lightest, i.e., simplest systems where it has been demonstrated so far.

Chapter 7

Summary and Outlook

7.1 Summary

In the present work the ultrafast ionization dynamics of nanoscale systems in intense x-ray pulses was investigated. The experiments were conducted in the high-field physics (HFP) system at the endstation for atomic, molecular and optical (AMO) sciences of the linac coherent light source (LCLS) free-electron laser in Stanford. As a sample system argon atoms and clusters with sizes between $\langle \mathrm{N} \rangle = 55$ and $\langle \mathrm{N} \rangle = 1600$ were studied. The clusters were irradiated with intense 480 eV x-ray pulses with power densities of a few $10^{17}\, W/cm^2$. Ionic fragments of the atoms and clusters were recorded with an ion time-of-flight spectrometer. To investigate time-dependent effects, the x-ray pulse length was tuned between 30 fs and 85 fs using the novel LCLS slotted spoiler technique.

Argon atoms and clusters show a clear pulse length dependence in the ionization. Longer x-ray pulses are absorbed more efficiently than shorter x-ray pulses with the same number of photons. Because of secondary processes in the cluster nanoplasma, including recombination and explosion, it is virtually impossible to directly compare spectra from different sizes. To overcome this limitation from previous experiments, a novel analysis approach is introduced, taking advantage of the fact that the same number of absorbed photons leads to the same ion spectrum for every cluster size. The x-ray induced transparency increase (XITI) describes the difference in x-ray pulse energy, i.e., number of photons, to induce the same absorption in a sample with a long and compared to a short pulse. In a short pulse more photons are needed to achieve a fundamentally similar cluster ionization compared to a long pulse. As a result, the XITI is a measure for the time-dependent effects in the absorption process. It was determined for every cluster size from the acquired data set including measurements for different pulse lengths and pulse energies. The XITI shows a clear size dependance, it increases from atoms to small clusters and decreases for larger clusters again. With a simple model this can be interpreted as an increase of the Auger

lifetime with size of the highly ionized clusters. To support the interpretation of the experimental data, a rate equation model for the pulse length dependent ionization was developed. The experimental data together with the simulations show that the Auger lifetime increases from an atom to a cluster and with increasing cluster size. This increase in Auger lifetime can be explained with delocalization of the valence electrons in the massively ionized cluster that has been theoretically predicted [19]. When the valence electrons are delocalized they have a lower overlap with inner-shell holes which results in decreased Auger lifetimes. Due to core-level bleaching, the increase in Auger lifetime leads to a lower absorption of intense x-ray pulses for larger cluster compared to smaller ones.
The size-dependence of the Auger rates is of importance for a wide range of experiments at free-electron laser sources making use of the high power densities. These range from single-shot imaging, where advanced damage models could be developed to the investigation of hot dense plasmas.

7.2 Outlook

In the following section the impact of the present results for ultrafast x-ray science is explained in more detail and an outlook on future experiments investigating the ionization dynamics in intense x-ray pulses is given.
Single-shot imaging of nanometer sized non-periodic objects and nanocrystals is one the most important applications for intense x-ray pulses. In those imaging techniques the photo absorption damage limits the usable photon fluence. Very high fluences can still be used to record meaningful scattering images, if the pulse length is short compared to the Auger lifetimes of the sample [16]. Through the increased Auger lifetimes in nanometer-sized samples the radiation damage may be lower than predicted by current damage models.
Double core-hole spectroscopy has been proposed to greatly increase the sensitivity in chemical analysis [102, 103]. The lifetimes of the inner-shell holes are the decisive parameters for these investigations as they determine the core hole abundance for a certain pulse intensity. For larger systems the influence of the environment and the additional changes in the valence electrons through ionization will have to be taken into account.
In dense x-ray excited plasmas inner-shell ionization and subsequent Auger decays play an important role [11, 104]. The Auger rates of the sample system are an important part of theoretical models that are used to simulate an interpret experimental data. Understanding the environmental influence on the ionization dynamics, i.e., Auger rates, could help to develop more sophisticated models for such matter in extreme conditions.
In a further step, the method of measuring the x-ray induced transparency increase (XITI) can be extended to more complicated systems such as heterogenous clusters or large molecules. It

will yield information about the ionization dynamics in different sample systems. Once a larger set of experimental data for the ionization with intense x-ray pulses becomes available, more sophisticated theoretical models for the ionization dynamics could be developed. Together with those models the XITI can give a precise quantitative feedback on the time-dependent effects in the samples.

To improve the time resolution of the measurements and extract a direct gauge for time-dependent effects in the ionization, x-ray pump – x-ray probe experiments could be performed. With the first pulse, a certain ionization state of the sample could be prepared and its development over time could be probed with a second x-ray pulse. Populations and binding energies of electronic states in the nanoplasma could be measured as a function of time and give insight on inner-shell vacancy lifetimes. Through ion spectroscopy the total absorption and the fragments of the exploding nanoplasma can be measured. Photoelectron and Auger-electron spectroscopy, as well as scattered photons and fluorescence photons can give a snapshot of electronic states in the nanoplasma during the ionization process. All these experimental techniques are available and have been used in experiments at x-ray free-electron lasers. Also, double x-ray pulses with a femtosecond delay have recently become available at the LCLS. Both pulses are produced with the same electron bunch, of which two slices are cut out using a spoiler foil with a double slot (c.f. Fig. 2.9). As both pulses come out of the undulator they are automatically spatially overlapped in the focus. However, the pulse length of both pulses is fixed and the range of delays is limited by the electron bunch length. Another way to produce two temporally separated x-ray pulses is split and delay unit using mirrors, as it has been implemented at the FLASH FEL for the XUV wavelength regime [105]. At the LCLS a simpler approach with two mirrors is under development [106] and a eight mirror system is in planning for future beamlines. A coincident measurement of ions, electrons and photons in an x-ray pump – x-ray probe experiment can give a complete picture of the ionization dynamics of nanometer sized samples.

While the ionization dynamics of intense x-ray pulses in samples is of interest for a large community performing experiments with x-ray lasers, there is also a fundamental interest in the properties and dynamics of a hot dense plasmas itself. Matter with a high density and a high temperature is prevalent in stars and the cores of giant planets. It is also relevant for inertial confinement fusion. Free nanoclusters are ideal model systems to prepare and probe such plasmas as they initially have solid density and no energy dissipation to surrounding media occurs. If the nanoplasma is prepared using an optical laser, ultrashort x-ray pulses can be used to probe the time-dependent properties similar to the study in the present work. When the clusters are excited with an intense but long optical laser pulse the properties of induced plasma undergoes changes over the length of the pulse. A certain combination of density, temperature and charge density of the nanoplasma can be probed by adjusting the delay between the optical pump pulse and one or two x-ray probe pulses. X-ray induced dynamics in the nanoplasma produced with an optical pulse could be traced. Therefore, the plasma is produced with the optical pulse. After a certain time, a first x-ray pulses ionizes inner-shell electrons and the population of these states

can be probed with a second x-ray pulse. State-of-the art optical laser systems are available at most FEL sources. The time resolution between optical and x-ray pulses is limited by an inherent jitter between the accelerator based FEL and the optical laser. A way to reduce this jitter is to measure the delay between x-ray and optical pulse for every shot. At the LCLS AMO endstation such an x-ray–optical cross-correlator system has been developed improving the time resolution to currently below 50 fs fwhm and potentially below 10 fs with shorter x-ray pulses [107].

Appendix

List of Figures

List of Tables

Bibliography

[1] P. Emma, R. Akre, J. Arthur, R. Bionta, C. Bostedt, J. Bozek, A. Brachmann, P. Bucksbaum, R. Coffee, F. J. Decker, Y. Ding, D. Dowell, et al., Nat. Photonics **4**, 641 (2010).

[2] V. Petrovic, M. Siano, J. White, N. Berrah, C. Bostedt, J. Bozek, D. Broege, M. Chalfin, R. Coffee, J. Cryan, and L. Fang, Phys. Rev. Lett. **108**, 253006 (2012).

[3] M. Guehr et al., in preparation .

[4] M. M. Seibert, T. Ekeberg, F. R. N. C. Maia, M. Svenda, J. Andreasson, O. Joensson, D. Odic, B. Iwan, A. Rocker, D. Westphal, M. Hantke, D. P. DePonte, et al., Nature **470**, 78 (2011).

[5] H. N. Chapman, P. Fromme, A. Barty, T. A. White, R. A. Kirian, A. Aquila, M. S. Hunter, J. Schulz, D. P. DePonte, U. Weierstall, R. B. Doak, F. R. N. C. Maia, et al., Nature **470**, 73 (2011).

[6] S. Boutet, L. Lomb, G. J. Williams, T. R. M. Barends, A. Aquila, R. B. Doak, U. Weierstall, D. P. DePonte, J. Steinbrener, R. L. Shoeman, M. Messerschmidt, A. Barty, et al., Science **337**, 362 (2012).

[7] L. Young, E. P. Kanter, B. Krässig, Y. Li, A. M. March, S. T. Pratt, R. Santra, S. H. Southworth, N. Rohringer, L. F. Dimauro, G. Doumy, C. A. Roedig, et al., Nature **466**, 56 (2010).

[8] M. Hoener, L. Fang, O. Kornilov, O. Gessner, S. T. Pratt, M. Guehr, E. P. Kanter, C. Blaga, C. Bostedt, J. D. Bozek, P. H. Bucksbaum, C. Buth, et al., Phys. Rev. Lett. **104**, 253002 (2010).

[9] J. P. Cryan, J. M. Glownia, J. Andreasson, A. Belkacem, N. Berrah, C. I. Blaga, C. Bostedt, J. Bozek, C. Buth, L. F. DiMauro, L. Fang, O. Gessner, et al., Phys. Rev. Lett. **105**, 083004 (2010).

[10] T. Gorkhover, M. Adolph, D. Rupp, S. Schorb, S. W. Epp, B. Erk, L. Foucar, R. Hartmann, N. Kimmel, K.-U. Kühnel, D. Rolles, B. Rudek, et al., Phys. Rev. Lett. **108**, 245005 (2012).

[11] S. M. Vinko, O. Ciricosta, B. I. Cho, K. Engelhorn, H.-K. Chung, C. R. D. Brown, T. Burian, J. Chalupsky, R. W. Falcone, C. Graves, V. Hajkova, A. Higginbotham, et al., Nature **482**, 49 (2012).

[12] LCLS brochure on the LCLS website: http://lcls.slac.stanford.edu.

[13] L. Lomb, T. R. M. Barends, S. Kassemeyer, A. Aquila, S. W. Epp, B. Erk, L. Foucar, R. Hartmann, B. Rudek, D. Rolles, A. Rudenko, R. L. Shoeman, et al., Phys. Rev. B **84**, 214111 (2011).

[14] A. Barty, C. Caleman, A. Aquila, N. Timneanu, L. Lomb, T. A. White, J. Andreasson, D. Arnlund, S. Bajt, T. R. M. Barends, M. Barthelmess, M. J. Bogan, et al., Nat. Photonics **6**, 35 (2012).

[15] R. Neutze, R. Wouts, D. van der Spoel, E. Weckert, and J. Hajdu, Nature **406**, 752 (2000).

[16] S.-K. Son, L. Young, and R. Santra, Phys. Rev. A **83**, 033402 (2011).

[17] E. P. Kanter, B. Kraessig, Y. Li, A. M. March, P. Ho, N. Rohringer, R. Santra, S. H. Southworth, L. F. DiMauro, G. Doumy, C. A. Roedig, N. Berrah, et al., Phys. Rev. Lett. **107**, 233001 (2011).

[18] G. Doumy, C. Roedig, S. Son, C. I. Blaga, A. D. DiChiara, R. Santra, N. Berrah, C. Bostedt, J. D. Bozek, P. H. Bucksbaum, J. P. Cryan, L. Fang, et al., Phys. Rev. Lett. **106**, 083002 (2011).

[19] U. Saalmann, and J. M. Rost, Phys. Rev. Lett. **89**, 143401 (2002).

[20] P. Emma, K. Bane, M. Cornacchia, Z. Huang, H. Schlarb, G. Stupakov, and D. Walz, Phys. Rev. Lett. **92**, 074801 (2004).

[21] C. Bostedt, H. N. Chapman, J. T. Costello, J. R. C. Lopez-Urrutia, S. Duesterer, S. W. Epp, J. Feldhaus, A. Foehlisch, M. Meyer, T. Moeller, R. Moshammer, M. Richter, et al., Nucl. Instr. Meth. **601**, 108 (2009).

[22] H. Motz, J. Appl. Phys. **22**, 527 (1951).

[23] Z. Huang, and K.-J. Kim, Phys. Rev. Spec. Top. - Acc. Beams **10**, 034801 (2007).

[24] E. Saldin, E. Schneidmiller, and M. Yurkov, *The physics of free-electron lasers*, Springer-Verlag, Berlin Heidelberg New York, 2000.

[25] http://hasylab.desy.de/facilities/flash/machine/how_it_works/high_gain_fel/index_eng.html.

[26] L. Yu, L. DiMauro, A. Doyuran, W. Graves, E. Johnson, R. Heese, S. Krinsky, H. Loos, J. Murphy, G. Rakowsky, J. Rose, T. Shaftan, et al., Phys. Rev. Lett. **91**, 074801 (2003).

[27] W. Ackermann, G. Asova, V. Ayvazyan, A. Azima, N. Baboi, J. Baehr, V. Balandin, B. Beutner, A. Brandt, A. Bolzmann, R. Brinkmann, O. I. Brovko, et al., Nat. Photonics **1**, 336 (2007).

[28] T. Shintake, H. Tanaka, T. Hara, T. Tanaka, K. Togawa, M. Yabashi, Y. Otake, Y. Asano, T. Bizen, T. Fukui, S. Goto, A. Higashiya, et al., Nat. Photonics **2**, 555 (2008).

[29] D. Zhu, M. Cammarata, J. Feldkamp, D. Fritz, J. Hastings, S. Lee, H. Lemke, A. Robert, J. Turner, and Y. Feng, Appl. Phys. Lett. **101**, 034103 (2012).

[30] E. Allaria, C. Callegari, D. Cocco, W. M. Fawley, M. Kiskinova, C. Masciovecchio, and F. Parmigiani, N. J. Phys. **12**, 075002 (2010).

[31] D. Pile, Nat. Photonics **5**, 456 (2011).

[32] W. Helml, A. Maier, W. Schweinberger, I. Grugras, P. Radcliffe, G. Doumy, C. Roedig, J. Gagnon, M. Messerschmidt, S. Schorb, G. F., and L. DiMauro, submitted to Nat. Photonics (2012).

[33] A. Cavalieri et al., in preparation (2012).

[34] I. Yamada, J. Matsuo, N. Toyoda, and A. Kirkpatrick, Mat. Sci. Eng. R **34**, 231 (2001).

[35] H. Haberland, *Chapter "Cluster" in [108]*, Walter de Gruyter & Co., 1992.

[36] J. Jortner, Z. Phys. D **24**, 247 (1992).

[37] T. Ditmire, T. Donnelly, A. Rubenchik, R. Falcone, and M. Perry, Phys. Rev. A **53**, 3379 (1996).

[38] T. Ditmire, J. Zweiback, V. Yanovsky, T. Cowan, G. Hays, and K. Wharton, Nature **398**, 489 (1999).

[39] H. Wabnitz, L. Bittner, A. de Castro, R. Dohrmann, P. Gurtler, T. Laarmann, W. Laasch, J. Schulz, A. Swiderski, K. von Haeften, T. Moller, B. Faatz, et al., Nature **420**, 482 (2002).

[40] U. Saalmann, J. Mod. Optic. **53**, 173 (2006).

[41] T. Fennel, K.-H. Meiwes-Broer, J. Tiggesbaeumker, P.-G. Reinhard, P. M. Dinh, and E. Suraud, Rev. Mod. Phys. **82**, 1793 (2010).

[42] T. Doppner, T. Fennel, T. Diederich, J. Tiggesbaumker, and K. Meiwes-Broer, Phys. Rev. Lett. **94**, 013401 (2005).

[43] C. Bostedt, H. Thomas, M. Hoener, E. Eremina, T. Fennel, K.-H. Meiwes-Broer, H. Wabnitz, M. Kuhlmann, E. Plönjes, K. Tiedtke, R. Treusch, J. Feldhaus, et al., Phys. Rev. Lett. **100**, 133401 (2008).

[44] H. Thomas, A. Helal, K. Hoffmann, N. Kandadai, J. Keto, J. Andreasson, B. Iwan, M. Seibert, N. Timneanu, J. Hajdu, M. Adolph, T. Gorkhover, et al., Phys. Rev. Lett. **108**, 133401 (2012).

[45] B. Van de Waal, J. Chem. Phys. **98**, 4909 (1993).

[46] J. Farges, M. Feraudy, B. Raoult, and G. Torchet, Surf. Sci. **106**, 95 (1981).

[47] E. Becker, K. Bier, and W. Henkes, Z. Phys. A **146**, 333 (1956).

[48] O. F. Hagena, and W. Obert, J. Chem. Phys. **56**, 1793 (1972).

[49] H. Haberland, U. Buck, and M. Tolle, Rev. Sci. Instr. **56**, 1712 (1985).

[50] U. Buck, and R. Krohne, J. Chem. Phys. **105**, 5408 (1996).

[51] U. Buck, U, and H. Meyer, Phys. Rev. Lett. **52**, 109 (1984).

[52] D. R. Miller, *Free je expansion*, in [109], p. 14, 1988.

[53] D. Rupp, M. Adolph, T. Gorkhover, S. Schorb, D. Wolter, R. Hartmann, N. Kimmel, C. Reich, T. Feigl, A. R. B. de Castro, R. Treusch, L. Strueder, et al., N. J. Phys. **14**, 055016 (2012).

[54] O. F. Hagena, Surf. Sci. **106**, 101 (1981).

[55] J. Stapelfeldt, *CLULU: Ein neues Experiment für Fluorescenceuntersuchungen an Edelgas-Clustern vom Dimer bis zum Mikrokristall*, PhD thesis, Universität Hamburg, 1989.

[56] V. Senz, T. Fischer, P. Oelssner, J. Tiggesbaeumker, J. Stanzel, C. Bostedt, H. Thomas, M. Schoeffler, L. Foucar, M. Martins, J. Neville, M. Neeb, et al., Phys. Rev. Lett. **102**, 138303 (2009).

[57] S. Schorb et al., in preparation (2012).

[58] U. Becker, and D. Shirley, editors, *VUV and Soft X-Ray Photoionization*, Plenum, 1996.

[59] Los Alamos National Laboratory Atomic Physics Codes, http:// aphysics2.lanl.gov/cgi-bin/ion/runlanl08a.pl.

[60] L. Meitner, Zeit. f. Phys. **9**, 131 (1922).

[61] P. Auger, C.R.A.S. **177**, 169 (1923).

[62] M. O. Krause, J. Phys. Chem. Ref. Data **8** (1979).

[63] L. Keldysh, Sov. Phys. JETP **20**, 1307 (1965).

[64] C. Bostedt, H. Thomas, M. Hoener, T. Möller, U. Saalmann, I. Georgescu, C. Gnodtke, and J.-M. Rost, New J. Phys. **12**, 083004 (2010).

[65] M. Hoener, C. Bostedt, S. Schorb, H. Thomas, L. Foucar, O. Jagutzki, H. Schmidt-Boeking, R. Doerner, and T. Moeller, Phys. Rev. A **78**, 021201 (2008).

[66] H. Iwayama, K. Nagaya, M. Yao, H. Fukuzawa, X.-J. Liu, G. Pruemper, M. Okunishi, K. Shimada, K. Ueda, T. Harada, M. Toyoda, M. Yanagihara, et al., J. Phys. B **42**, 134019 (2009).

[67] T. Laarmann, M. Rusek, H. Wabnitz, J. Schulz, A. de Castro, P. Gurtler, W. Laasch, and T. Moller, Phys. Rev. Lett. **95**, 063402 (2005).

[68] T. Laarmann et al., in preparation (2012).

[69] C. Bostedt, M. Adolph, E. Eremina, M. Hoener, D. Rupp, S. Schorb, H. Thomas, A. R. B. de Castro, and T. Moeller, J. Phys. B **43**, 194011 (2010).

[70] C. Bostedt, E. Eremina, D. Rupp, M. Adolph, H. Thomas, M. Hoener, A. R. B. De Castro, J. Tiggesbäumker, K.-H. Meiwes-Broer, T. Laarmann, H. Wabnitz, E. Plönjes, et al., Phys. Rev. Lett. **108**, 093401 (2012).

[71] M. Islam, U. Saalmann, and J. Rost, Phys. Rev. A **73**, 041201 (2006).

[72] T. Fennel, T. Doppner, J. Passig, C. Schaal, J. Tiggesbaumer, and K. H. Meiwes-Broer, Phys. Rev. Lett. **98**, 143401 (2007).

[73] C. Gnodtke, U. Saalmann, and J.-M. Rost, Phys. Rev. Lett. **108**, 175003 (2012).

[74] I. Georgescu, U. Saalmann, and J. M. Rost, Phys. Rev. Lett. **99**, 183002 (2007).

[75] S. Zamith, T. Martchenko, Y. Ni, S. Aseyev, H. Muller, and M. Vrakking, Phys. Rev. A **70** (2004).

[76] L. Koller, M. Schumacher, J. Kohn, S. Teuber, J. Tiggesbaumker, and K. Meiwes-Broer, Phys. Rev. Lett. **82**, 3783 (1999).

[77] M. Arbeiter, and T. Fennel, Phys **82**, 013201 (2010).

[78] C. Siedschlag, and J. Rost, Phys. Rev. Lett. **93**, 043402 (2004).

[79] M. Hoener, C. Bostedt, H. Thomas, L. Landt, E. Eremina, H. Wabnitz, T. Laarmann, R. Treusch, A. de Castro, and T. Möller, J. Phys. B **41**, 181001 (2008).

[80] M. Arbeiter, and T. Fennel, New J. Phys. **13**, 053022 (2011).

[81] H. Thomas, C. Bostedt, M. Hoener, E. Eremina, H. Wabnitz, T. Laarmann, E. Plönjes, R. Treusch, A. R. B. De Castro, and T. Möller, J. Phys. B **42**, 134018 (2009).

[82] B. Ziaja, H. N. Chapman, R. Santra, T. Laarmann, E. Weckert, C. Bostedt, and T. Möller, Phys. Rev. A **84**, 033201 (2011).

[83] J. D. Bozek, Eur. Phys. J. **169**, 129 (2009).

[84] S. Moeller, J. Arthur, A. Brachmann, R. Coffee, F. J. Decker, Y. Ding, D. Dowell, S. Edstrom, P. Emma, Y. Feng, A. Fisher, J. Frisch, et al., Nucl. Instr. Meth. **635**, S6 (2011).

[85] S. P. Hau-Riege, R. M. Bionta, D. D. Ryutov, R. A. London, E. Ables, K. I. Kishiyama, S. Shen, M. A. McKernan, D. H. McMahon, M. Messerschmidt, J. Krzywinski, P. Stefan, et al., Phys. Rev. Lett. **105**, 043003 (2010).

[86] L. Strüder, S. Epp, D. Rolles, R. Hartmann, P. Holl, G. Lutz, H. Soltau, R. Eckart, C. Reich, K. Heinzinger, C. Thamm, A. Rudenko, et al., Nucl. Instr. Meth. **614**, 483 (2010).

[87] P. Kirkpatrick, and A. Baetz, J. Opt. Soc. Am. **38**, 766 (1948).

[88] J. Krzywinski, personal communication.

[89] O. Hemmers, S. Whitfield, P. Glans, H. Wang, D. Lindle, R. Wehlitz, and I. Sellin, Rev. Sci. Instr. **69**, 3809 (1998).

[90] W. Wiley, and I. McLaren, Rev. Sci. Instr. **26**, 1150 (1955).

[91] D. A. Dahl, Int. J. Mass Spec. **200**, 3 (2000).

[92] H. Thomas, *Wechselwirkung von Edelgas-Clustern mit intensiven Pulsen weicher Röntgenstrahlung vom Freie-Elektronen-Laser FLASH*, PhD thesis, Technische Universität Berlin, 2010.

[93] B. Rudek, S.-K. Son, L. Foucar, S. Epp, B. Erk, M. Hartmann, M. Adolph, R. Andritschke, A. Aquila, N. Berrah, C. Bostedt, J. Bozek, et al., accepted at Nat. Photonics (2012).

[94] N. Rohringer, and R. Santra, Phys. Rev. A **76**, 033416 (2007).

[95] C. P. Bhalla, N. O. Folland, and M. A. Hein, Phys. Rev. A **8**, 649 (1973).

[96] L. Natarajan, Phys. Scr. **75**, 47 (2007).

[97] M. Y. Amusa, I. S. Lee, and V. A. Kilin, Phys. Rev. A **45**, 4576 (1992).

[98] L. Fang, M. Hoener, O. Gessner, F. Tarantelli, S. T. Pratt, O. Kornilov, C. Buth, M. Guehr, E. P. Kanter, C. Bostedt, J. D. Bozek, P. H. Bucksbaum, et al., Phys. Rev. Lett. **105**, 083005 (2010).

[99] C. Buth, J.-C. Liu, M. H. Chen, J. P. Cryan, L. Fang, J. M. Glownia, M. Hoener, R. N. Coffee, and N. Berrah, J. Chem. Phys. **136**, 214310 (2012).

[100] A. A. Sorokin, P. Juranic, J. U., K. Tiedtke, M. Richter, M. Yabashi, M. Nagasono, S. Moeller, J. Krzywinski, and S. Hau-Riege, Report on pulse energy monitoring of x-ray FEL beam by gas-monitor detector, 2010.

[101] W. F. Schlotter, J. J. Turner, M. Rowen, P. Heimann, M. Holmes, O. Krupin, M. Messerschmidt, S. Moeller, J. Krzywinski, R. Soufli, M. Fernandez-Perea, N. Kelez, et al., Rev. Sci. Instr. **83**, 043107 (2012).

[102] L. Cederbaum, F. Tarantelli, A. Sgamellotti, and J. Schirmer, J. Chem. Phys. **85**, 6513 (1986).

[103] N. Berrah, L. Fang, B. Murphy, T. Osipov, K. Ueda, E. Kukk, R. Feifel, P. van der Meulen, P. Salen, H. T. Schmidt, R. D. Thomas, M. Larsson, et al., P. Natl. Acad. Sci. USA **108**, 16912 (2011).

[104] B. Nagler, U. Zastrau, R. R. Faeustlin, S. M. Vinko, T. Whitcher, A. J. Nelson, R. Sobierajski, J. Krzywinski, J. Chalupsky, E. Abreu, S. Bajt, T. Bornath, et al., Nat. Physics **5**, 693 (2009).

[105] R. Mitzner, A. A. Sorokin, B. Siemer, S. Roling, M. Rutkowski, H. Zacharias, M. Neeb, T. Noll, F. Siewert, W. Eberhardt, M. Richter, P. Juranic, et al., Phys. Rev. A **80**, 025402 (2009).

[106] J. Castagna et al., in preparation (2012).

[107] S. Schorb, T. Gorkhover, J. P. Cryan, J. M. Glownia, M. R. Bionta, R. N. Coffee, B. Erk, R. Boll, C. Schmidt, D. Rolles, A. Rudenko, A. Rouzee, et al., Appl. Phys. Lett. **100**, 121107 (2012).

[108] W. Raith, editor, *Lehrbuch der Experimentalphysik, Band V: Struktur der Materie*, Walter de Gruyter & Co., 1992.

[109] G. Scoles, editor, *Atomic and Molecular Beam Methods*, Oxford University Press, 1988.

Appendix A

Publications of the Author

Size-dependent ultrafast ionization dynamics of nanoscale samples in intense femtosecond x-ray free-electron laser pulses
S. Schorb, D. Rupp, M. L. Swiggers, R, N. Coffee, M. Messerschmidt, G. Williams, J. D. Bozek, S.-I. Wada, O. Kornilov, T. Möller, and C. Bostedt
Physical Review Letters **108**, 233401 (2012)

X-ray-optical cross-correlator for gas-phase experiments at the Linac Coherent Light Source free-electron laser
S. Schorb, T. Gorkhover, J. P. Cryan, J. M. Glownia, M. R. Bionta, R. N. Coffee, B. Erk, R. Boll, C. Schmidt, D. Rolles, A. Rudenko, A. Rouzee, M. Swiggers, S. Carron, J. C. Castagna, J. D. Bozek, M. Messerschmidt, W. F. Schlotter, and C. Bostedt
Applied Physics Letters **100**, 121107 (2012)

Identification of twinned gas phase clusters by single shot scattering with soft X-ray FEL pulses
D. Rupp, M. Adolph, T. Gorkhover, **S. Schorb**, D. Wolter, R. Hartmann, N. Kimmel, C. Reich, T. Feigl, A. R. B. de Castro, R. Treusch, L. Strüder, T. Möller and C. Bostedt
New Journal of Physics **14**, 055016 (2012)

Explosions of xenon Clusters in Ultraintense Femtosecond X-Ray Pulses from the LCLS Free Electron Laser
H. Thomas, A. Helal, K. Hoffmann, N. Kandadai, J. Keto, J. Andreasson, B. Iwan, M. Seibert, N. Timneanu, J. Hajdu, M. Adolph, T. Gorkhover, D. Rupp, **S. Schorb**, T. Möller, G. Doumy, L. F. DiMauro, M. Hoener, B. Murphy, N. Berrah, M. Messerschmidt, J. Bozek, C. Bostedt, and T. Ditmire
Physical Review Letters **108**, 133401 (2012)

Nanoplasma dynamics of single large xenon clusters irradiated with super intense x-ray pulses from the Linac Coherent Light Source free-electron laser
T. Gorkhover, M. Adolph, D. Rupp, **S. Schorb**, S.W. Epp, B. Erk, L. Foucar, R. Hartmann, N. Kimmel, K.-U. Kühnel, D. Rolles, B. Rudek, A. Rudenko, R. Andritschke, A. Aquila, J.D. Bozek, N. Coppola, T. Erke, F. Filsinger, H. Gorke, H. Graafsma, L. Gumprecht, G. Hauser, S. Herrmann, H. Hirsemann, A. Hömke, P. Holl, C. Kaiser, F. Krasniqi, J.-H. Meyer, M. Matysek, M. Messerschmidt, D. Miessner, B. Nilsson, D. Pietschner, G. Potdevin, C. Reich, G. Schaller, C. Schmidt, F. Schopper, C.D. Schröter, J. Schulz, H. Soltau, G. Weidenspointner, I. Schlichting, L. Strüder, J. Ullrich, T. Möller, and C. Bostedt
Physical Review Letters **108**, 245005 (2012)

Ionization dynamics in expanding clusters studied by XUV pump-probe spectroscopy
M. Krikunova, M. Adolph, T. Gorkhover, D. Rupp, **S. Schorb**, C. Bostedt, S. Roling, B. Siemer, R. Mitzner, H. Zacharias and .T Möller
Journal of Physics B: Atomic Molecular and Optical Physics **45**, 105101 (2012).

Explosion, ion acceleration and molecular fragmentation of methane clusters in the pulsed beam of a free-electron laser
B. Iwan, J. Andreasson, M. Bergh, **S. Schorb**, H. Thomas, D. Rupp, T. Gorkhover, M. Adolph, T. Möller, C. Bostedt, J. Hajdu, and N. Timneanu
Physical Review A **86**, 033201 (2012)

Ultra-Efficient Ionization of Heavy Atoms by Intense X-Ray Free-Electron Laser Pulses
B. Rudek, S.-K. Son, L. Foucar, S.W. Epp, B. Erk, R. Hartmann, M. Adolph, R. Andritschke, A. Aquila, N. Berrah, C. Bostedt, J. Bozek, N. Coppola, F. Filsinger, H. Gorke, T. Gorkhover, H. Graafsma, L. Gumprecht, A. Hartmann, G. Hauser, S. Herrmann, H. Hirsemann, P. Holl, A. Hömke, L. Journel, C. Kaiser, N. Kimmel, F. Krasniqi, K.-U. Kühnel, M. Matysek, M. Messerschmidt, D. Miesner, T. Möller, R. Moshammer, K. Nagaya, B. Nilsson, G. Potdevin, D. Pietschner, C. Reich, D. Rupp, G. Schaller, I. Schlichting, C. Schmidt, F. Schopper, **S. Schorb**, C.-D. Schröter, J. Schulz, M. Simon, H. Soltau, L. Strüder, K. Ueda, G. Weidenspointner, R. Santra, J. Ullrich, A. Rudenko, and D. Rolles
Accepted at Nature Photonics (2012)

Amorphous to crystalline phase transition in carbon induced by intense femtosecond x-ray free-electron laser pulses
J. Gaudin, O. Peyrusse, J. Chalupsky, M. Toufarov, L. Vysin, V. Hajkova, R. Sobierajski, T. Burian, Sh. Dastjani-Farahani, A. Graf, M. Amati, L. Gregoratti, S. P. Hau-Riege, G. Hoffmann, L. Juha, J. Krzywinski, R. A. London, S. Moeller, H. Sinn, **S. Schorb**, M. Störmer, Th. Tschentscher, V. Vorlicek, H. Vu, J. Bozek, and C. Bostedt
Physical Review B **86** 024103 (2012)

Ultrafast transitions from solid to liquid and plasma states of graphite induced by x-ray free-electron laser pulses
S.P. Hau-Riege, A. Graf, T. Döppner, R. A. London, J. Krzywinski, C. Fortmann, S. H. Glenzer, M. Frank, K. Sokolowski-Tinten, M. Messerschmidt, C. Bostedt, **S. Schorb**, J. A. Bradley, A. Lutman, D. Rolles, A. Rudenko, B. Rudek
Physical Review Letters **108**, 217401 (2012)

Transient x-ray fragmentation: Probing a prototypical photoinduced ring opening
V. S. Petrovic, M.S., James L. White, N. Berrah, C. Bostedt, J.D. Bozek, D. Broege, M. Chalfin, R.N. Coffee, J.P. Cryan, L. Fang, J.P. Farrell, L.J. Frasinski, J.M. Glownia, M. Gühr, M. Hoener, D.M.P. Holland, J. Kim, J.P. Marangos, T. Martinez, B.K. McFarland, R.S. Minns, S. Miyabe, **S. Schorb**, R.J. Sension, L.S. Spector, R. Squibb, H. Tao, J.G. Underwood, and Philip H. Bucksbaum
Physical Review Letters **108**, 253006 (2012)

Angle-Resolved Electron Spectroscopy of Laser-Assisted Auger Decay Induced by a Few-Femtosecond X-Ray Pulse
M. Meyer, P. Radcliffe, T. Tschentscher, J. T. Costello, A. L. Cavalieri, I. Grguras, A. R. Maier, R. Kienberger, J. Bozek, C. Bostedt, **S. Schorb**, R. Coffee, M. Messerschmidt, C. Roedig, E. Sistrunk, L. F. Di Mauro, G. Doumy, K. Ueda, S. Wada, S. Duesterer, A. K. Kazansky, and N. M. Kabachnik
Physical Review Letters **108**, 063007 (2012)

Spectral encoding of x-ray/optical relative delay
M. R. Bionta, H. T. Lemke, J. P. Cryan, J. M. Glownia, C. Bostedt, M. Cammarata, J.-C. Castagna, Y. Ding, D. M. Fritz, A. R. Fry, J. Krzywinski, M. Messerschmidt, **S. Schorb**, M. L. Swiggers, and R. N. Coffee
Optics Express **19**, 21855 (2011)

Femtosecond X-ray protein nanocrystallography
H. N. Chapman, P. Fromme, A. Barty, T. A. White, R. A. Kirian, A. Aquila, M. S. Hunter, J. Schulz, D. P. De-Ponte, U. Weierstall, R. B. Doak, F. R. N. C. Maia, A. V. Martin, I. Schlichting, L. Lomb, N. Coppola, R. L. Shoeman, S. W. Epp, R. Hartmann, D. Rolles, A. Rudenko, L. Foucar, N. Kimmel, G. Weidenspointner, P. Holl, M. Liang, M. Barthelmess, C. Caleman, S. Boutet, M. J. Bogan, J. Krzywinski, C. Bostedt, S. Bajt, L. Gumprecht, B. Rudek, B. Erk, C. Schmidt, A. Hoemke, C. Reich, D. Pietschner, L. Strueder, G. Hauser, H. Gorke, J. Ullrich, S. Herrmann, G. Schaller, F. Schopper, H. Soltau, K.-U. Kuehnel, M. Messerschmidt, J. D. Bozek, S. P. Hau-Riege, M. Frank, C. Y. Hampton, R. G. Sierra, D. Starodub, G. J. Williams, J. Hajdu, N. Timneanu, M. M. Seibert, J. Andreasson, A. Rocker, O. Joensson, M. Svenda, S. Stern, K. Nass, R. Andritschke, C.-D. Schröter, F. Krasniqi, M. Bott, K. E. Schmidt, X. Wang, I. Grotjohann, J. M. Holton, T. R. M. Barends, R. Neutze, S. Marchesini, R. Fromme, **S. Schorb**, D. Rupp, M. Adolph, T. Gorkhover, I. Andersson, H. Hirsemann, G. Potdevin, H. Graafsma, B. Nilsson, and J. C. H. Spence
Nature **470**, 73 (2011)

Single mimivirus particles intercepted and imaged with an X-ray laser
M. M. Seibert, T. Ekeberg, F. R. N. C. Maia, M. Svenda, J. Andreasson, O. Joensson, D. Odic, B. Iwan, A. Rocker, D. Westphal, M. Hantke, D. P. DePonte, A. Barty, J. Schulz, L. Gumprecht, N. Coppola, A. Aquila, M. Liang, T. A. White, A. Martin, C. Caleman, S. Stern, C. Abergel, V. Seltzer, J.-M. Claverie, C. Bostedt, J. D. Bozek, S. Boutet, A. A. Miahnahri, M. Messerschmidt, J. Krzywinski, G. Williams, K. O. Hodgson, M. J. Bogan, C. Y. Hampton, R. G. Sierra, D. Starodub, I. Andersson, S. Bajt, M. Barthelmess, J. C. H. Spence, P. Fromme, U.Weierstall, R. Kirian, M. Hunter, R. B. Doak, S. Marchesini, S. P. Hau-Riege, M. Frank, R. L. Shoeman, L. Lomb, S. W. Epp, R. Hartmann, D. Rolles, A. Rudenko, C. Schmidt, L. Foucar, N. Kimmel, P. Holl, B. Rudek, B. Erk, A. Hoemke, C. Reich, D. Pietschner, G. Weidenspointner, L. Strüder, G. Hauser, H. Gorke, J. Ullrich, I. Schlichting, S. Herrmann, G. Schaller, F. Schopper, H. Soltau, K.-U. Kuehnel, R. Andritschke, C.-D. Schröter, F. Krasniqi, M. Bott, **S. Schorb**, D. Rupp, M. Adolph, T. Gorkhover, H. Hirsemann, G. Potdevin, H. Graafsma, B. Nilsson, H. N. Chapman, and J. Hajdu
Nature **470**, 78 (2011)

Clusters in intense FLASH pulses: ultrafast ionization dynamics and electron emission studied with spectroscopic and scattering techniques
C. Bostedt, M. Adolph, E. Eremina, M. Hoener, D. Rupp, **S. Schorb**, H. Thomas, A. R. B. de Castro, and T. Möller
Journal of Physics B - Atomic Molecular and Optical Physics **43**, 194011 (2010)

From fission to explosion: Momentum-resolved survey over the Rayleigh instability barrier M. Hoener, C. Bostedt, **S. Schorb**, H. Thomas, L. Foucar, O. Jagutzki, H. Schmidt-Boeking, R. Doerner, and T. Möller
Physical Review A **78**, 021201 (2008)

Acknowledgements

The work that resulted in this thesis was prepared and performed at the Technische Universität Berlin and the SLAC National Accelerator Laboratory. It would not have been possible without the support of many people whom I would like to thank.

First and foremost I would like to thank Christoph Bostedt and Thomas Möller. Thomas gave me the opportunity to join his group and I would like to thank him for his continuous support and advise as well as for the freedom to follow my own plans and ideas. I am deeply grateful to Christoph for his scientific guidance, his promotion and his support in all possible issues over the course of the last years. Thanks to him I got the unique opportunity to come to SLAC and participate in many fascinating experiments at LCLS from the beginning on.
I had a great time at the TU Berlin, in the office and the lab and also in many weeks of beamtimes at the FLASH free-electron laser in Hamburg. For these exciting years I want to thank Marcus Adolph, Tais Gorkhover, Lasse Landt, Benjamin Röben, Daniela Rupp, Matthias Staiger, Heiko Thomas, Rainer Unterumsberger, David Wolter, and Tobias Zimmermann. Especially Lasse was always a great friend and colleague. And beyond that a consistent and tough training partner. Early morning runs in the Berlin snow mud, cans of tuna for breakfast and near-death experiences in the pool of the olympic stadium are only a few of the highlights. The preparation for the triathlons in Hamburg and Monterey resulted in the balance that was necessary for long beamtimes and to concentrate on the office work.
I joined SLAC and LCLS in April 2010 and thanks to the LCLS team and particularly the AMO team I had a very exciting and joyful time. Experiments at the LCLS are always collaborative efforts and I would like to thank all LCLS staff for running this incredible machine and for the their great support. Specifically I am indebted to Michelle Swiggers and Jean-Charles Castagna for their support in designing, setting up and preparing the experiments. John Bozek, Ryan Coffee, Marc Messerschmidt, Daniela Rupp, Shin-Ichi Wada, and Garth Williams helped controlling the experiment during long night shifts in the AMO control room. In particular Daniela kept the necessary overview in the early morning hours. The simulations shown in this work benefitted a lot from advise and discussions with Oleg Kornilov. For the support with the data acquisition system I would like to thank Marc Messerschmidt and Matthew Weaver. Furthermore, many thanks go to Ulf Saalmann for the time an effort of reviewing this thesis. Finally I would like to thank Ken Ferguson and Sebastian Carron for proof-reading the thesis.